SCUOLA DI DOTTORATO
UNIVERSITÀ DEGLI STUDI DI MILANO-BICOCCA

Department of
Materials Science

PhD course in Materials Science and Nanotechnology
Cycle XXXII

DYNAMICS IN POROUS MATERIALS

Negroni Mattia
RN 745759

Tutor: Prof A. Comotti

ACADEMIC YEAR 2018-2019

A process cannot be understood by stopping it.
Understanding must move with the flow of the process,
must join it and flow with it.

-The First Law of Mentat, Dune

Abstract

Porous materials offer a unique environment in the solid state, with systems consisting of a substantial amount of empty space. This can be used in many different ways, particularly with regard to gases. A gas in a porous material sees a drastic and selective change in its degrees of freedom, with a severity that depends on the intrinsic characteristics of the gas and the pores. The main interaction is usually the adhesion of the gas on the pore walls, a phenomenon called adsorption. An adsorbed gas behaves like a liquid but the pressure is much lower than the vapour pressure. For this reason, many porous materials are studied for gas transport, with the possibility of storing it in a high density liquid-like phase without the high pressure normally required.

However, gas is not the only dynamic part in such systems. Usually solid matter is consider static because the close-packed structure does not allow for many movement. In a porous material, the void space can be used by some part of the structure to move. This opens up new possibilities for functional materials able of interacting in more complex ways with gases. Molecular motion is of great interest and there are several research groups interested in this emerging field.

Despite the significant number of publications about adsorption and molecular rotors, few of them address the issue of the interaction between these two dynamics systems. I think that this topic may be of great interest for the practical applications of more advance porous materials. Molecular rotors should, in theory, alter the adsorption process generating more complex adsorption profiles. This differentiation can bring to materials with a more favourable behaviour for application in gas storage and separation. For this reasons I decided to focus my research project in this field by joining the Sozzani's Research Group.

Here I came into contact with a considerable knowledge and expertise on adsorption and molecular rotors, but I was also able to study new interesting materials. The complexity of this project will be clear during the reading of this thesis. The first five chapters are dedicated to the introduction of the theories and techniques used during my PhD. I had to study both of these worlds and a good parts of what I had learned is in these paragraphs.

The first step of my work was to understand the interaction between gas and rotors and how this affects rotation. There were already some publications about rotor dynamic reduction after adsorption with variable results depending on the adsorbed substance. The only common result was the reversibility of the process. Notably, I_2 has the greatest stopping power especially for *p*-phenyl rotors. I performed several NMR measurements on materials with different CO_2 pressures to analyse the evolution of the spectra. The choice was due to the good adsorption capacity of the samples for this gas. I discovered that the interaction tend to increase the activation energy for the rotation without altering the type of motion or the frequency at infinite temperature. I also noticed that the variation in energy is a function of the loading.

A significant problem with these results was the loading itself. In simple and uniform systems adsorption is simple but it increases in complexity if the porous network becomes more intricate. The assumption of liquid-like behaviour is applicable with small adjustments to meso- and macroporous materials, but the gases inside micropores begin to act differently. A special case is the single file diffusion in ultramicropores, a typical condition in many materials.

I decided to face this problem and tried to understand the dynamics of gas in tight pores. Using NMR, I was able to study the

diffusion mechanism of xenon and CO_2 inside porous materials. The results show the jump mechanism between adsorption sites and from the spectra acquired at variable temperature it was possible to calculate the activation energy of the jumps. Although these empirical results contain a considerable amount of information, they are not sufficient to completely map the diffusion because NMR analyses an average interaction. Molecular dynamics play a fundamental role in helping to understand the behaviour of a single molecule inside a narrow channel. These reveal a peculiar dynamic and how shape and charge distribution within the channel are imprinted in the gas motion.

Another important problem with ultramicroporosity is the pore size distribution. Standard adsorption analysis using non-local DFT struggles to accurately map small pores, especially if the pore system is complex. I restored our hyperpolarized xenon apparatus to perform more detailed pore size studies. Despite the technique is very powerful and is able to provide some unique information, it is not widely used. Literature about hyperpolarized xenon in novel porous materials like PAFs and MOFs is scarce if not inexistent. I began to probe the applicability of this technique to such materials and the results are very good, opening the possibility to more advance studies.

Following the idea of more advance NMR measurements for the characterization of porous materials, I spent six month at the EPFL in Lausanne in Prof. Emsley laboratories. There I studied the dynamic nuclear polarization which is another hyperpolarization technique based on radicals polarization transfer. The application is usually related to mesoporous materials that can be used as scaffolding for the radicals or studying the diffusion of polarization.

This thesis is a selection of the main works of my three years experience, during which I had to expand my knowledge in many different directions just to start to understand these complex systems.The combination of adsorptions, x-rays, NMR and *ab initio* calculations is fundamental to outline a clear picture of interactions between gases and molecular rotors. The correct interpretation of this considerable amount of data can lead to a good understanding of porous structures and to the design of functional materials. Professor Kitagawa said that, while the depletion of petroleum is a critical concern, "the age of gas is dawning". So I expect a growing interest for a better control of gases and porous material will play a key role in the near future. What I try in the past years was to unveil some hidden mechanism and I have to say, I am quite satisfied with the results.

But I clearly see even more interesting projects just ahead.

RIASSUNTO

I materiali porosi offrono un contesto unico allo stato solido, questi sistemi hanno una notevole quantità di spazio vuoto. Questo può essere utilizzato in molti modi diversi, in particolare per quanto riguarda i gas. Un gas in un materiale poroso vede un drastico e selettivocambiamento dei suoi gradi di libertà, con una magnitudine che dipende dalle caratteristiche intrinseche del gas e dei pori. L'interazione principale è solitamente l'adesione del gas sulle pareti dei pori, fenomeno chiamato adsorbimento. Un gas adsorbito si comporta come un liquido ma ciò avviene ad una pressione molto più bassa della pressione del vapore. Per questo motivo, molti materiali porosi sono studiati per il trasporto di gas, con la possibilità di conservarlo in una fase liquida ad alta densità senza l'alta pressione normalmente richiesta.

Tuttavia, il gas non è l'unica parte dinamica in tali sistemi. Di solito la materia allo stato solido è considerata statica perché la struttura compatta non consente molti movimenti. In un materiale poroso, lo spazio vuoto può essere utilizzato da alcune parti della struttura per muoversi. Ciò apre nuove possibilità per materiali funzionali in grado di interagire in modo più complesso con i gas. Il movimento molecolare è di grande interesse e vi sono diversi gruppi di ricerca interessati a questo ambito.

Nonostante il numero significativo di pubblicazioni sull'adsorbimento e sui rotori molecolari, poche affrontano la questione dell'interazione tra queste due dinamiche. Penso che tale argomento possa essere di grande interesse per le applicazioni pratiche di materiali porosi più avanzati. I rotori molecolari dovrebbero, in teoria, alterare il processo di adsorbimento generando profili di adsorbimento più complessi. Questa differenziazione può portare a materiali con un comportamento più favorevole per l'applicazione nello stoccaggio e nella separazione del gas. Per questo motivo ho deciso di concentrare il mio progetto di ricerca in questo campo unendomi al gruppo di ricerca del Prof. Sozzani.

Qui sono entrato in contatto con una notevole conoscenza ed esperienza sull'adsorbimento e sui rotori molecolari, ma sono stato anche in grado di studiare nuovi ed interessanti materiali. La complessità del progetto sarà chiara durante la lettura di questa tesi. I primi cinque capitoli sono dedicati all'introduzione delle teorie e delle tecniche utilizzate durante il mio dottorato. Ho dovuto studiare entrambi questi mondi e una buona parte di ciò che ho imparato è in questi paragrafi.

Il primo passo del mio lavoro è stato quello di comprendere l'interazione tra gas e rotori e come ciò influisce sulla rotazione. Vi erano già alcune pubblicazioni sulla riduzione della dinamica del rotore dopo l'adsorbimento con risultati variabili a seconda della sostanza adsorbita. L'unico risultato comune è stata la reversibilità del processo. In particolare, I_2 ha il più grande potere di arresto specialmente per i rotori *p*-fenilenici. Ho eseguito diverse misurazioni NMR su materiali con diverse pressioni di CO_2 per analizzare l'evoluzione degli spettri. La scelta è dovuta alla buona capacità di adsorbimento dei campioni per questo gas. Ho scoperto che l'interazione tende ad aumentare l'energia di attivazione per la rotazione senza alterare il tipo di movimento o la frequenza a temperatura infinita. Notai anche che la variazione di energia è una funzione della quantità adsorbita.

Un importante problema di questi risultati è il caricamento stesso. In sistemi semplici e uniformi l'adsorbimento è semplice ma aumenta in complessità se il sistema poroso diventa più complesso. L'assunzione di un comportamento simile al liquido è applicabile, con piccoli aggiustamenti ,ai materiali meso- e macroporosi, ma i gas all'interno dei micropori iniziano a comportarsi diversamente. Un caso

speciale è la diffusione in file all'interno di ultramicropori, una condizione tipica in molti materiali.

Decisi di affrontare questo problema e cercai di comprendere la dinamica del gas in pori stretti. Usando l'NMR, sono stato in grado di studiare il meccanismo di diffusione di xeno e CO_2 all'interno di materiali porosi. I risultati rivelano il meccanismo di salto tra i siti di adsorbimento e dagli spettri acquisiti a temperatura variabile è stato possibile calcolare l'energia di attivazione dei salti. Sebbene questi risultati empirici contengano una considerevole quantità di informazioni, non sono sufficienti per mappare completamente la diffusione perché l'NMR analizza un'interazione media. Simulazioni di dinamica molecolare svolgono un ruolo fondamentale per comprendere il comportamento di una singola molecola all'interno di un canale. Queste rivelano una dinamica peculiare e come la forma e la distribuzione delle cariche all'interno del canale sono impresse nel moto del gas.

Un altro problema con l'ultramicroporosità è la distribuzione delle dimensioni dei pori. L'analisi standard dell'adsorbimento che utilizza la DFT fatica a mappare accuratamente piccoli pori, specialmente se il sistema è complesso. Ripristinai il nostro apparato dello xeno iperpolarizzato per eseguire studi più dettagliati sulle dimensioni dei pori. Nonostante la tecnica sia molto potente ed è in grado di fornire alcune informazioni uniche, non è ampiamente utilizzata. La letteratura sullo xeno iperpolarizzato in materiali porosi di recente scoperta come PAF e MOF è scarsa se non inesistente. Cominciai a sondare l'applicabilità di questa tecnica a tali materiali e i risultati sono molto buoni, aprendo la strada a studi più avanzati.

Seguendo l'idea di misure NMR più avanzate per la caratterizzazione di materiali porosi, ho trascorso sei mesi all'EPFL di Losanna nei laboratori del Prof. Emsley. Lì ho studiato la DNP che è un'altra tecnica di iperpolarizzazione basata sul trasferimento di polarizzazione dei radicali. L'applicazione è solitamente correlata a materiali mesoporosi che possono essere utilizzati come impalcatura per i radicali o studiando la diffusione di polarizzazione nei pori.

Questa tesi è una selezione dei principali lavori della mia esperienza di tre anni, durante i quali ho dovuto espandere la mia conoscenza in molte direzioni diverse solo per iniziare a comprendere questi sistemi complessi. La combinazione di adsorbimento, raggi X, NMR e calcoli *ab initio* è fondamentale per delineare un quadro chiaro delle interazioni tra gas e rotori molecolari. La corretta interpretazione di questa considerevole quantità di dati può portare a una buona comprensione della struttura porosa e alla progettazione di materiali funzionali. Il professor Kitagawa ha affermato che, mentre l'esaurimento del petrolio è una preoccupazione crescente, "l'età del gas sta sorgendo". Quindi mi aspetto un interesse crescente verso un migliore controllo di gas e i materiali poroso avranno un ruolo chiave nel prossimo futuro. Quello che ho provato negli anni passati è stato svelare alcuni meccanismi nascosti e devo dire che sono piuttosto soddisfatto dei risultati.

Ma vedo chiaramente progetti ancora più interessati giusto dietro l'angolo.

Contents

1 Porous Materials 1
- 1.1 Pores 1
  - Connection 1
  - Shape 1
  - Size 2
  - Distribution 2
  - Origin 2
- 1.2 Density 2
  - Bulk 2
  - Apparent 2
  - True 2
- 1.3 Materials 3
  - Zeolites 3
  - Metal-Organic Frameworks 4
  - Organic Frameworks 5
  - Molecular Crystals 5

2 Ideal Adsorption 11
- 2.1 The Basic Theory 11
  - Langmuir Isotherm 11
  - Low Adsorption 12
  - Multiple Adsorption Sites 13
  - Multiple Adsorption Layers 14
  - Sigmoidal Isotherm 14
- 2.2 Surface Area 16
  - Langmuir Surface 16
  - BET Surface 17
- 2.3 Heat 17
  - Van't Hoff 17
- 2.4 Selectivity 18
  - Henry's Law 18
  - IAST 18
- 2.5 Adsorption Simulations 20
  - Grand Canonical Monte Carlo Simulation 21

3 Molecular Rotors 25
- 3.1 Rotor Structure 25
- 3.2 Biological Rotors 25
- 3.3 Synthetic Rotors 25
  - Surface 25
  - Porous Systems 26
- 3.4 Applications 27
  - Compasses 27
  - Adsorption 27

4 Tachometry 33
- 4.1 Anysotropy Study 33
  - Tensors Conventions 33
  - Motion Averaging 35
  - Experiment 36
  - Pros and Cons 37
- 4.2 Second Moment 38
  - Measure 38
  - Calculation 38
  - Pros and Cons 39
- 4.3 Relaxation Times 39
  - Measure 40
  - Energy Calculation 43
  - Theoretical Values 45
  - Spin-Spin Relaxation 47
  - Quadrupolar Nuclei 47
  - Pros and Cons 48

5 Hyperpolarization 53
- 5.1 Strategies 53
- 5.2 Dynamic Nuclear Polarization (DNP) 53
  - Mechanisms 53
  - Polarizing Agents 55
  - Microwave Sources 56
  - Dissolution DNP 57
  - Developments 57
- 5.3 Spin-Exchange Optical Pumping (SEOP) 58
  - Mechanism 58
  - Applications 59

6 Rotor-Gas Interaction 67
- 6.1 Molecular Rotors in a Porous Organic Framework 67
  - Crystal Structure 67
  - Gas Adsorption 68
  - MAS NMR Spectroscopy 68
- 6.2 Ultrafast Molecular Rotors in a Metal Organic Framework 72
  - Crystal Structure 72
  - Adsorption 73
  - NMR Spectroscopy 75

7 Gas Dynamic in the Solid State by NMR 81
7.1 Xe Diffusion 81
Crystal Structure 81
Gas Adsorption 82
NMR Spectroscopy 83
Simulations 84
7.2 CO_2 Diffusion 86
Crystal Structure 86
Gas Adsorption 87
CO_2 Study 88

8 Fluorinated Porous Aromatic Frameworks 95
8.1 Functionalization of PAFs 95
Synthesis 95
^{13}C MAS NMR 96
Porosity Evaluation 97
Gas Adsorption and Selectivity 98

9 Porous Dipeptides as Volatile Drug Vessels 103
9.1 Porous Dipeptides 103
Anesthetics 103
Crystal Structures 103
Adsorption 105
^{1}H fast-MAS NRM 105
Adsorbate Conformation 107

10 Conclusions 111
10.1 Interaction 111
10.2 Gas Dynamics 111
10.3 Drug Vessels 111
10.4 Fluorine PAFs 111
10.5 Future 111
10.6 Scientific Impact of Mattia Negroni 112
Articles 112
Conferences 112

A Materials Details A1
BSPEB and *n*-benzylamine A1
Zn-BPEB A1
TCF-1 A2
CPOS-5 A2
L-valyl-L-alanine A3
L-alanyl-L-isoleucine A3
L-valyl-L-valine A3
L-isoleucyl-L-alanine A3
L-isoleucyl-L-valine A4

1. Porous Materials

Porous materials have been extensively studied over the part years due to their application in adsorption, catalysis, ion exchange, nanotechnology, etc.[1] The definition of "porous" is quite broad and involves any material that, at the atomic level, is not densely stacked but form voids. This classification does not take into account the pore size, pore distribution or the chemistry of the material.[2]

Whit such a generic definition, the enormous amount of research and applications is not a surprise. There are many sub-categories for these materials and their knowledge is essential for orienting in this world.

1.1 Pores

The pore is the main point of interest in a porous material. This empty space is related to all the main proprieties of the material and can be classified according to different aspects.

Connection

Not all pores are accessible to an external fluid in the same way, the figure 1.1 will help with the following definitions. First of all there are the closed pores (a), which are inaccessible. These affect macroscopic proprieties but are not useful for surface-related interactions such as gas adsorption or ion exchange. All other pores are defined as open pores, but there are other details to consider. The pores with only one open end are called blind pores (b,f) while the through pores are open from both ends (e). It is also important not to confuse porosity with roughness, even if they are similar. A rough material becomes porous if the irregularities are deeper than they are wide.[3]

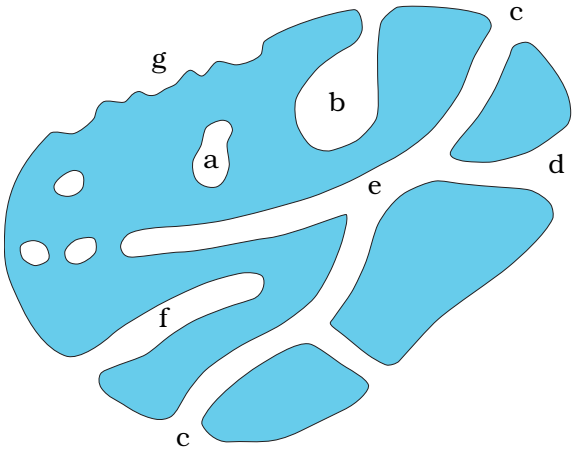

Figure 1.1: Schematic cross-section of a porous solid.[3]

Shape

The shape of the pores can also be important for their properties. The principal shapes are shown in figure 1.2. In literature it is also possible to find rhomboid, elliptical and square shapes. This simplistic description is useful for modelling the material and often the pore system is described as a combination of geometric shapes (cylinders, prisms, cavities, slits and spheres). Sometimes the network is so complex that the material is described by its geometric shapes and the pore are just the voids.[4]

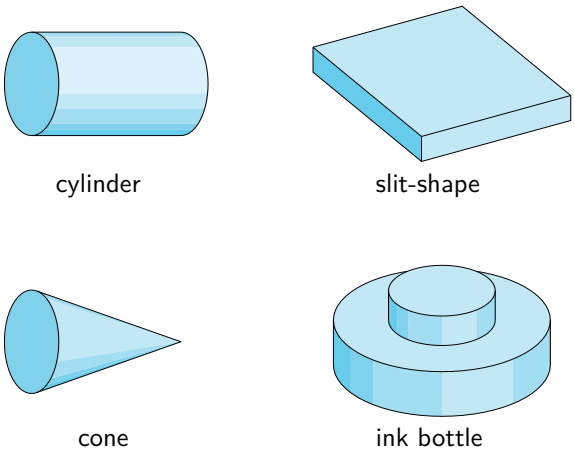

Figure 1.2: Pore shapes.[5]

Size

The most common and most important pore subdivision is based on the diameter (or pore width). Obviously this parameter can be applied exactly in the case of pores with a defined geometry. In case of irregular porous systems, the term refers to the smaller dimension.[3] Pore width is a fundamental parameter because it determines the guest that can diffuse inside the material. Size is also important for the phenomena that occur inside the material; a large pore can accommodate larger molecules but the surface is relatively low and *vice versa*.

IUPAC classifies the pore in three categories:[3]

- *Macropores* Width larger than 50 nm.
- *Mesopores* Width between 2 and 50 nm.
- *Micropores* Width smaller than 2 nm.

Distribution

As already mentioned, the pore size is not always constant. For this reason it is also important to determine the pore size distribution. This parameter is fundamental for determining the final properties of the system. Crystalline materials tend to have a very narrow distribution but amorphous compounds usually present an uneven pore width.

Origin

It is also important to distinguish the origin of porous materials. One possibility is that the pores are part of a crystal structure and for this reason they form a regular network with narrow size distribution. A second category consists of particles with loose (aggregates) or consolidated (agglomerates) packing. A porous material can also be formed by subtraction, removing some parts of the original system to generate pores.[3]

1.2 Density

A delicate issue with porous materials is density. The main problem is the volume to be considered in the formula because the pores are technically part of the material itself. This generates three possible density definitions:[3]

Bulk

The bulk density considers the total volume of the material including all the pores, therefore it is the smallest density. In the case of aggregate powders (such as soils) the bulk density is not constant because it strongly depends on the packing.[6]

Similar to bulk is the crystallographic density which takes into account the entire volume of the crystal cell. In this case the value is constant.

Apparent

In apparent density, the volume considered excludes the open pores, it however keeps the close pores. It is called "apparent" because is the one measured by fluid displacement (picnometry) and therefore the close pores are impossible to reach by the sample fluid. These measures always assume a negligible adsorption effect that would change the fluid density.[3]

This is usually the reported density, along with the liquid used and its temperature.[7]

True

This density takes into account only the volume occupied by the material, excluding any kind of pore. In the absence of close pores, it is equal to the apparent density. In the presence of close pores it is extremely difficult to measure and could be only estimated. In the case of crystal structures, it is often calculated from the unit cell analysis.

1.3 MATERIALS

Porous materials are often divided into precise categories based on the elements of the structure and the way in which they are connected. Of the enormous amount of materials, only some of them are presented in the following chapters. The main objective is gas adsorption, a surface phenomenon, so they are prevalently microporous systems.

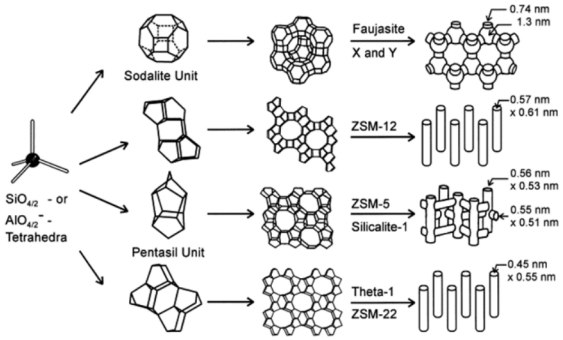

Figure 1.3: Structures of four selected zeolites and their micropore systems and dimensions. [10]

ZEOLITES

A zeolite (Fig. 1.3) is a crystalline aluminosilicate with a three-dimensional structure that forms uniformly sized pores of molecular dimensions. These inorganic structures have been known since 1756 but only in the 1980s, with synthetic zeolites (Barrier, 1948), they became of great interest. The microporosity combined with the crystal form allowed their use as molecular sieves.

The main components of the zeolites are silicon (Si^{4+}) and aluminium (Al^{3+}) cations surrounded by oxygen ions (O^{2-}). Silicon is always the main cation but sometimes is replaced by aluminium (with a minimum Si/Al ratio of 1). The substitution does not change the structure of the zeolite but generates a net negative charge in the framework. To compensate, the material has some cations inside the pores. These ions are free to move in the pores and tend to have a very high mobility. For this reason, zeolites are widely use as ion exchangers. [8]

Currently there are only 245 known zeolite structures, both natural (around 40) and synthetic. This number is incredibly small considering over 40 years of intense research and the number of new structures in recent years is very small. [9]

Synthesis

Zeolites are synthesized through hydrothermal crystallization of an aluminosilicate gel or solution. The process must be performed in a basic environment (pH > 10) and usually takes several days or weeks.

The mechanism of zeolite formation is not completely understood. Experiments show the formation of an initial amorphous gel with a structure very similar to the final crystal. A subsequent rearrangement of the aluminosilicate framework creates the zeolite. This is very different from the more classical crystallization based on nucleation and growth. [11]

Most of synthetic methods requires organic compounds as structure-directing agents that remain in the final compound and are removed by calcination at high temperature. Unfortunately these are often expensive, corrosive and toxic and are converted into harmful gases during the removal process. Another problem is the possibility of crystal deformation due to the high temperature. For all these reasons, some template-free synthesis have been studied. [12]

Applications

The first and most important application of zeolites is in the petroleum and chemical industry due to their catalytic properties in a considerable number of hydrocarbon reactions like cracking, isomerization and alkylation. [13] Zeolites are excellent catalytic materials because it is possible to perform shape-selective conversions with the right choice of pore size and cationic content in the framework. For this reason they are

also used in fine chemistry (for drugs or perfumes).[14]

Ion exchange is another very important application. Zeolites are commonly used in detergents to soften the water as an alternative to sodium tripolyphospate whose enviromental impact problem arose about half a century ago. It is also possible to use this propriety in the treatment of wastewater to remove harmful substances and even some radio-nuclei in radioactive waste. They can also be used as a supplement in animal food.[8]

The incredible regularity of small pores make zeolites good materials for gas adsorption and very efficient dessicants. However their use is mainly focused on gas separation and enrichment using the technique of pressure swing adsorption.

Zeolites can also form membranes used for dehydration of organic solvents, catalysis or for gas separation.[14,15]

Metal-Organic Frameworks

These systems are coordination networks with organic ligands containing potential voids (Fig. 1.4).[16] A large amount of Metal-Organic Frameworks (MOFs) are crystalline.

Interest in MOFs began in the 1990s and is still a field of great interest. Compared to zeolites, these materials can be created in milder conditions (below 300° C) and there are several synthetic routes. These are fundamental because not only change the macroscopic result of the synthesis, but can create different MOFs.[17,18]

The pore size in these materials range from microporosity to macroporosity,[19] this is due mainly to the organic part. The dimensions of the linker are related to the final pore size of the structure. It is often possible to tune the porosity: increasing length of the linker without changing its geometry generates a wider pore but with the same shape.[20]

Also the inorganic node has a great importance in determining the final structure. These are metal ions or clusters and are often referred to as secondary

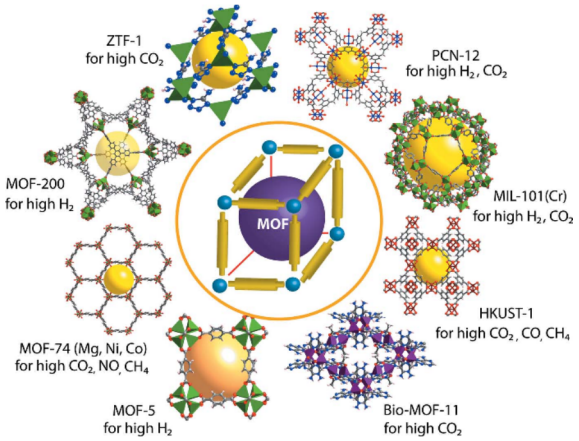

Figure 1.4: Schematic representation of important reported MOFs which are known for high gas storage properties.[23]

building units (SBUs). They are represented in simple geometric shapes.[21] Changing the node can drastically modify the MOF structure. This can be an advantage if, after the creation of a functional linkers, there is a need to find an appropriate framework.[22]

Synthesis

There are different ways to form the crystal structure of MOFs and the synthetic choice is not determined only by the nature of linkers and metal nodes. Different techniques can lead to different structures. Nevertheless, other parameters such as temperature, time, pressure, pH and solvent must be considered as well.

The standard method of diffusion is the simplest technique for the synthesis of MOFs. It can be performed in several ways but it is usually particularly slow, with weeks of reaction time. This is the best method for creating large single crystals.

As for zeolites, it is also possible to perform self-assembly using solvothermal methods. These are faster than the diffusion approach but the reaction time is in the order of days.

Microwave-assisted synthesis is another possible method. Microwaves affect metal particles and generate a uniform seeding condition but do not create a crystal. Crystallization occurs during the cooling of

the solution or during solvent evaporation. This technique can greatly accelerate the synthesis and control particles shape and size. However, it is not used so regularly.

There are also other possible synthetic ways for the creation of MOFs. The electrochemical method is the most used for industrial production and allows a fine tune with the regulation of the voltage or the use of particular signals. Sonochemistry is also very interesting because it promises a quick and easy synthetic method at ambient temperature.[24]

Applications

The possibility to create functional linkers is perhaps the reason for the great success of MOFs. The thermal stability is good (from 250° to 500° C) but the chemical stability is not always optimal particularly in presence of moisture or extreme pH (metal-ligand bonds are susceptible to hydrolysis).[25]

MOFs are very promising materials for gas adsorption and storage, especially for hydrogen; this effect is mostly due to the presence of small pores because this gas has a very low interaction with the organic linkers. Also the adsorption of methane is particularly high.[26] Some MOFs exhibit interesting proprieties for the direct air capture of CO_2.[27]

Their proton-conduction properties make these porous material interesting as electrolyte in fuel cells; replacing the more delicate perfluorosulfonic acid polymers.[28,29]

Industrial use is still limited, but some groups begin to focus on shaping for commercial purposes.[30]

Organic Frameworks

Porous Organic Frameworks (POFs) include more specific subclasses such as Covalent Organic Frameworks (COFs), Covalent Triazine Frameworks (CTFs), Porous Aromatic Frameworks (PAFs) and many others (Fig. 1.5). The common ground is that all are made by organic monomers connected through strong covalent

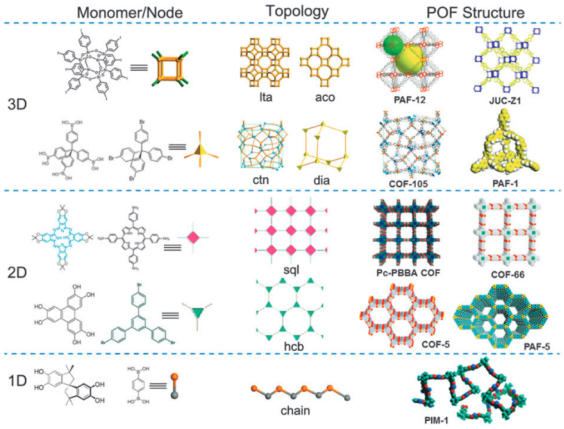

Figure 1.5: Schematic illustration of building blocks, underlying topologies, and final structures of POF materials..[31]

bonds.[31]

POFs have an extremely high surface area and a high porosity that give them an enormous adsorption capacity. Combining this characteristic with the flexibility of organic synthesis, it allows the creation of very specific functional materials. Fields of application include adsorption, separation, catalysis, sensor, magnetism and even bio-related.[32]

Due to the general definition of POFs, it is difficult to find common features within this category. The materials can be crystalline or amorphous, but they are able to maintain permanent porosity. They are usually microporous and with excellent thermal stability due to their covalent nature.[33]

Molecular Crystals

Molecular crystals are composed of discrete molecules without any strong covalent bond among them. The final structures are usually held together by weak interactions and can be easily dissolved in the appropriate solvent. The porosity is usually revealed by the removal of the solvent after the synthesis but, the lack of a covalent framework, implies that most molecular crystals cannot maintain the porosity after the thermal treatment and their structure collapses.[34] For this reason, porous molecular crystals are rare

compared to porous network materials.[35]

Nevertheless, over the years some very stable porous systems have been discovered, reaching also exceptional levels of porosity (4000 m^2/g).[36,37]

Synthesis

The synthesis is quite straight forward and any standard crystal growth technique is applicable, according to the proprieties and stability of the molecule. An important factor is purity because the incorporation of any impurities can have a considerable effect on the physical proprieties of the crystal.[38]

Applications

The main application of molecular crystals is in electronics as semiconductor. Compared to their inorganic counterparts, they present very interesting proprieties such as higher purity and order. These can also be modified by manipulating the crystal structure.[39,40]

Pharmaceutical applications are also studied. Many drugs are delivered as salts but this is not applicable to all molecules. The possibility of forming a cocrystal composed of the active molecule and another harmless compound is very interesting because it has less limitation respect to the salt formation.[41–43]

Bibliography

[1] Xu, R.; Pang, W.; Yu, J.; Huo, Q.; Chen, J. *Chemistry of Zeolites and Related Porous Materials*; John Wiley & Sons, Ltd, 2007.

[2] Zhu, G.; Ren, H. *Porous Organic Frameworks: Design, Synthesis and Their Advanced Applications*; SpringerBriefs in Molecular Science; Springer Berlin Heidelberg, 2014.

[3] Rouquerol, J.; Avnir, D.; Fairbridge, C. W.; Everett, D. H.; Haynes, J. M.; Pernicone, N.; Ramsay, J. D. F.; Sing, K. S. W.; Unger, K. K. Recommendations for the characterization of porous solids (Technical Report). *Pure and Applied Chemistry* **1994**, *66*, 1739–1758.

[4] Zdravkov, B.; Čermák, J.; Šefara, M.; Janků, J. Pore classification in the characterization of porous materials: a perspective. *Open Chemistry* **2007**, *5*.

[5] Kaneko, K. Determination of pore size and pore size distribution. *Journal of Membrane Science* **1994**, *96*, 59–89.

[6] Lal, R. *Encyclopedia of Soil Science*; Encyclopedia of Soil Science v. 1; Taylor & Francis, 2006.

[7] Lowell, S.; Shields, J.; Thomas, M.; Thommes, M. *Characterization of Porous Solids and Powders: Surface Area, Pore Size and Density*; Particle Technology Series; Springer Netherlands, 2006.

[8] Jacobs, P.; Flanigen, E.; Jansen, J.; van Bekkum, H. *Introduction to Zeolite Science and Practice*; Studies in Surface Science and Catalysis; Elsevier Science, 2001.

[9] Baerlocher, C.; McCusker, L. Database of Zeolites Structures.

[10] Weitkamp, J. Zeolites and catalysis. *Solid State Ionics* **2000**, *131*, 175–188.

[11] Xu, J.; Wang, Q.; Li, S.; Deng, F. *Solid-State NMR in Zeolite Catalysis*; Lecture Notes in Chemistry; Springer Singapore, 2019.

[12] Ng, E.; Zou, X.; Mintova, S. *New and Future Developments in Catalysis: Chapter 12. Environmental Synthesis Concerns of Zeolites*; Elsevier Science, 2013.

[13] Bhatia, S. *Zeolite Catalysts: Principles and Applications*; Taylor & Francis, 1989.

[14] Rouquerol, J.; Rouquerol, F.; Llewellyn, P.; Maurin, G.; Sing, K. *Adsorption by Powders and Porous Solids: Principles, Methodology and Applications*; Elsevier Science, 2013.

[15] Cejka, J.; Corma, A.; Zones, S. *Zeolites and Catalysis: Synthesis, Reactions and Applications*; Wiley, 2010.

[16] Batten, S. R.; Champness, N. R.; Chen, X.-M.; Garcia-Martinez, J.; Kitagawa, S.; Öhrström, L.; O'Keeffe, M.; Suh, M. P.; Reedijk, J. Terminology of metal–organic frameworks and coordination polymers (IUPAC Recommendations 2013). *Pure and Applied Chemistry* **2013**, *85*, 1715–1724.

[17] Stock, N.; Biswas, S. Synthesis of metal-organic frameworks (MOFs): routes to various MOF topologies, morphologies and composites. *Chemical Reviews* **2011**, *112*, 933–969.

[18] Kuppler, R. J.; Timmons, D. J.; Fang, Q.-R.; Li, J.-R.; Makal, T. A.; Young, M. D.; Yuan, D.; Zhao, D.; Zhuang, W.; Zhou, H.-C. Potential applications of metal-organic frameworks. *Coordination Chemistry Reviews* **2009**, *253*, 3042–3066.

[19] Ahmed, A.; Hodgson, N.; Barrow, M.; Clowes, R.; Robertson, C. M.; Steiner, A.; McKeown, P.; Bradshaw, D.; Myers, P.; Zhang, H. Macroporous metal–organic framework microparticles with improved liquid phase separation. *J. Mater. Chem. A* **2014**, *2*, 9085–9090.

[20] Lu, W.; Wei, Z.; Gu, Z.-Y.; Liu, T.-F.; Park, J.; Park, J.; Tian, J.; Zhang, M.; Zhang, Q.; III, T. G.; Bosch, M.; Zhou, H.-C. Tuning the structure and function of metal–organic frameworks via linker design. *Chem. Soc. Rev.* **2014**, *43*, 5561–5593.

[21] Klabunde, K.; Richards, R. *Nanoscale Materials in Chemistry*; Wiley, 2009.

[22] Galli, S.; Maspero, A.; Giacobbe, C.; Palmisano, G.; Nardo, L.; Comotti, A.; Bassanetti, I.; Sozzani, P.; Masciocchi, N. When long bis(pyrazolates) meet late transition metals: structure, stability and adsorption of metal–organic frameworks featuring large parallel channels. *Journal of Materials Chemistry A* **2014**, *2*, 12208.

[23] Dey, C.; Kundu, T.; Biswal, B. P.; Mallick, A.; Banerjee, R. Crystalline metal-organic frameworks (MOFs): synthesis, structure and function. *Acta Crystallographica Section B Structural Science, Crystal Engineering and Materials* **2013**, *70*, 3–10.

[24] Safaei, M.; Foroughi, M. M.; Ebrahimpoor, N.; Jahani, S.; Omidi, A.; Khatami, M. A review on metal-organic frameworks: synthesis and applications. *TrAC Trends in Analytical Chemistry* **2019**, *118*, 401–425.

[25] Shengqian, M.; A, P. *Elaboration and Applications of Metal-Organic Frameworks*; Series On Chemistry, Energy And The Environment; World Scientific Publishing Company, 2018.

[26] Zhou, W.; Wu, H.; Hartman, M. R.; Yildirim, T. Hydrogen and methane adsorption in metal-organic frameworks: a high-pressure volumetric study. *The Journal of Physical Chemistry C* **2007**, *111*, 16131–16137.

[27] Kumar, A.; Madden, D. G.; Lusi, M.; Chen, K.-J.; Daniels, E. A.; Curtin, T.; Perry, J. J.; Zaworotko, M. J. Direct air capture of CO_2 by physisorbent materials. *Angewandte Chemie International Edition* **2015**, *54*, 14372–14377.

[28] Furukawa, H.; Cordova, K. E.; O'Keeffe, M.; Yaghi, O. M. The chemistry and applications of metal-organic frameworks. *Science* **2013**, *341*, 1230444–1230444.

[29] Chen, B.; Qian, G. *Metal-Organic Frameworks for Photonics Applications*; Structure and Bonding; Springer Berlin Heidelberg, 2014.

[30] Bazer-Bachi, D.; Assié, L.; Lecocq, V.; Harbuzaru, B.; Falk, V. Towards industrial use of metal-organic framework: impact of shaping on the MOF properties. *Powder Technology* **2014**, *255*, 52–59.

[31] Zhang, S.; Yang, Q.; Wang, C.; Luo, X.; Kim, J.; Wang, Z.; Yamauchi, Y. Porous organic frameworks: advanced materials in analytical chemistry. *Advanced Science* **2018**, *5*, 1801116.

[32] Zhang, H.; Li, G.; Liao, C.; Cai, Y.; Jiang, G. Bio-related applications of porous organic frameworks (POFs). *Journal of Materials Chemistry B* **2019**, *7*, 2398–2420.

[33] Zou, X.; Ren, H.; Zhu, G. Topology-directed design of porous organic frameworks and their advanced applications. *Chemical Communications* **2013**, *49*, 3925.

[34] McKeown, N. B. Nanoporous molecular crystals. *Journal of Materials Chemistry* **2010**, *20*, 10588.

[35] Tian, J.; Thallapally, P. K.; McGrail, B. P. Porous organic molecular materials. *CrystEngComm* **2012**, *14*, 1909.

[36] Mastalerz, M.; Oppel, I. M. Rational construction of an extrinsic porous molecular crystal with an extraordinary high specific surface area. *Angewandte Chemie International Edition* **2012**, *51*, 5252–5255.

[37] Zhang, G.; Presly, O.; White, F.; Oppel, I. M.; Mastalerz, M. A permanent mesoporous organic cage with an exceptionally high surface area. *Angewandte Chemie International Edition* **2014**, *53*, 1516–1520.

[38] Wright, J. *Molecular Crystals*; Molecular Crystals; Cambridge University Press, 1995.

[39] Pinotti, E.; Sassella, A.; Borghesi, A.; Tubino, R. Electrical characterization of organic semiconductors by transient current methods. *Synthetic Metals* **2001**, *122*, 169–171.

[40] Li, R.; Hu, W.; Liu, Y.; Zhu, D. Micro- and Nanocrystals of Organic Semiconductors. *Accounts of Chemical Research* **2010**, *43*, 529–540.

[41] Remenar, J. F.; Morissette, S. L.; Peterson, M. L.; Moulton, B.; MacPhee, J. M.; Guzmán, H. R.; Örn Almarsson, Crystal engineering of novel cocrystals of a triazole drug with 1,4-dicarboxylic acids. *Journal of the American Chemical Society* **2003**, *125*, 8456–8457.

[42] Velaga, S. P.; Basavoju, S.; Boström, D. Norfloxacin saccharinate-saccharin dihydrate cocrystal - a new pharmaceutical cocrystal with an organic counter ion. *Journal of Molecular Structure* **2008**, *889*, 150–153.

[43] Schultheiss, N.; Newman, A. Pharmaceutical cocrystals and their physicochemical properties. *Crystal Growth & Design* **2009**, *9*, 2950–2967.

2. Ideal Adsorption

The main propriety of a porous material is its ability to adsorbe gases on its internal surface. The main method to measure this capacity, is the analysis of adsorption isotherms. There are different interaction mechanisms between gases and surface and each one generates a precise curve.[1]

2.1 The Basic Theory

Adsorption is the adhesion of atoms, molecules or ions (called adsorbate) on a surface (adsorbent); the word was coined in 1881 by German physicist Heinrich Kayser.[2] It should not be confused with absorption, the process in which the fluid permeates a solid. Adsorption is a pure surface phenomenon and is classified in chemisorption (characterized by the formation of a chemical bond) and in physisorption (weak interaction).[3] The opposite effect is called desorption.

The unit of measurement of adsorption is not universal; the most common is cm^3/g and defines the cm^3 of adsorbate per gram of adsorbent. An alternative is the unit $mmol/g$ to highlight the number of molecules per gram and in the case of crystal structure there are also the variants mol/mol and $molecules/cell$. A more useful measure is $cm^3(STP)/cm^3$ which allows to immediately know the volume of gas trapped inside the material.

Langmuir Isotherm

The most common type of adsorption follows the Langmuir isotherm. This theory, developed by the Nobel Prize Irving Langmuir in 1918, is based on the premise that an adsorbate behaves like an ideal gas under isothermal condition. It also assumes:[4]

- The surface is flat.
- The adsorbed gas is in an immobile state.
- All adsorption sites are equivalent and can host only one molecule.
- There are no interactions between molecules of gas in adjacent sites.

All this can be translated in the following formula

Langmuir isotherm formula

$$Ads(P) = Ads_M \frac{K_L P}{1 + K_L P} \tag{2.1}$$

Ads_M is the maximum adsorbed quantity and is an useful data for calculation of the void occupancy;

K_L is the Langmuir constant and describe the adsorption/desorption equilibrium;

P is the pressure.

As shown in figure 2.1 the isotherm begins with a linear plot and then start to curve as it approaches its horizontal asymptote at $Ads = Ads_M$ (saturation). This tendency is justified by the limits:

$$\lim_{P \to 0} Ads(P) = Ads_M K_L P \tag{2.2}$$

$$\lim_{P \to \infty} Ads(P) = Ads_M \tag{2.3}$$

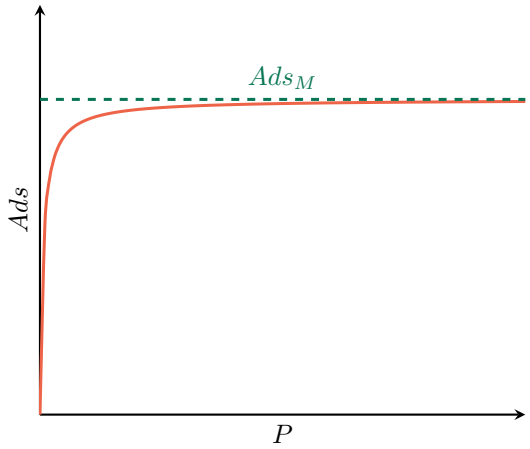

Figure 2.1: Langmuir isotherm plot.

The Langmuir model is a powerful theory but the assumptions are very strict and far from reality. Over the years new and more complex theories have tried to explain the adsorption of gases.

Low Adsorption

Langmuir was not the first scientist who studied gas properties, at his time all the major gas laws have more than a century. Despite this, adsorption was not well described and studied more thoroughly. Since the nineteenth century we have had the simplest and most basic isotherm of all.

Henry Isotherm

This isotherm (Fig. 2.2) is directly connected with Henry's law and it assumes:[4]

- The ideal behaviour of the gas.
- Uniform surface.
- There are no interactions between molecules of gas in adjacent sites.

Henry isotherm formula

$$Ads(P) = K_H P \tag{2.4}$$

K_H is the Henry constant.

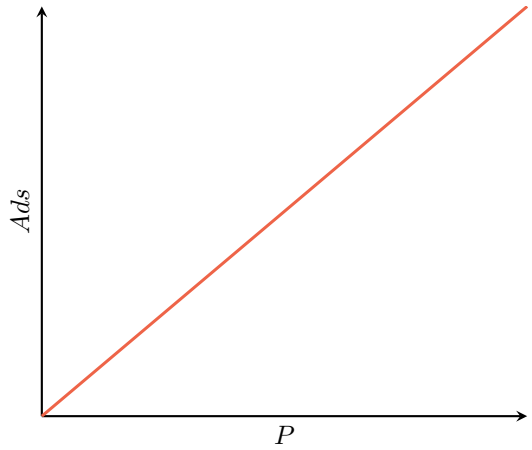

Figure 2.2: Henry isotherm plot.

It is easy to notice a similarity with the equation 2.2. In fact, this formula well describes the first part of all the main adsorption isotherms. Despite its limitations, it is often used to easily describe low pressure surface interaction or in the case of very low adsorption (due to a small interaction between surface and gas). Particular attention is needed when using this isotherm formula because it is a divergent equation:

$$\lim_{P\to\infty} Ads(P) = \infty \tag{2.5}$$

At some point the pressure becomes so high that the gas condenses or the material starts to saturate and the curve becomes a Langmuir.

Freundlich Isotherm

The theory behind Henry isotherm cannot be easily applied to real gases and real surfaces. In 1909, Herbert Freundlich, proposed a new isotherm (Fig. 2.3) that take into account of the possible interactions between adsorption sites on an heterogeneous surface.[5]

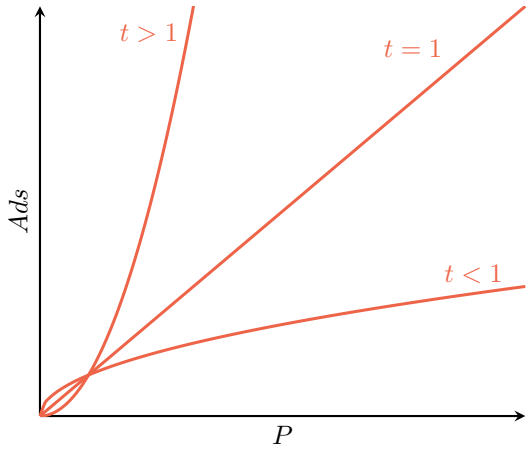

Figure 2.3: Freundlich isotherm plot.

Freundlich isotherm formula

$$Ads(P) = K_F P^t \tag{2.6}$$

K_F is the Freundlich constant;
t is function of the adsorption strength.
The t parameter is an indicator of the interaction between adsorbed molecules. We can have three possible situations:

$t = 1$: in this situation the adsorbed molecules do not interact and the adsorption follows the Henry isotherm described in the precedent chapter.

$t < 1$: in this situation there is a competitive adsorption between sites.

$t > 1$: is a rare situation of cooperative adsorption.[6]

Multiple Adsorption Sites

The main problem with Langmuir isotherm is the requirement of uniform surface. It is difficult to have such an ideal adsorption site, especially in porous materials. Usually the pores have an uneven electron density and sometimes these systems are created with a dedicated adsorption site for a specific gas.

Dual-site Langmuir Isotherm

Suppose two independent sites within the material and their individual behaviour can be described as a Langmuir (Fig. 2.4). This system can be descried with the sum of two Langmuir equation (2.1) with different parameters.

Dual-site Langmuir isotherm formula

$$Ads(P) = \frac{Ads_{M1} K_{L1} P}{1 + K_{L1} P} + \frac{Ads_{M2} K_{L2} P}{1 + K_{L2} P} \tag{2.7}$$

Ads_{M1} is the maximum adsorbed quantity of site 1;

K_{L1} is the Langmuir constant of site 1;

Ads_{M2} is the maximum adsorbed quantity of site 2;

K_{L2} is the Langmuir constant of site 2.

This equation is an implementation of the Langmuir theory and for this reason it has the same assumptions but it also supposes two independent adsorption sites. Also the limits are very similar:

$$\lim_{P \to 0} Ads(P) = (Ads_{M1} K_{L1} + Ads_{M2} K_{L2}) P \tag{2.8}$$

$$\lim_{P \to \infty} Ads(P) = Ads_{M1} + Ads_{M2} \tag{2.9}$$

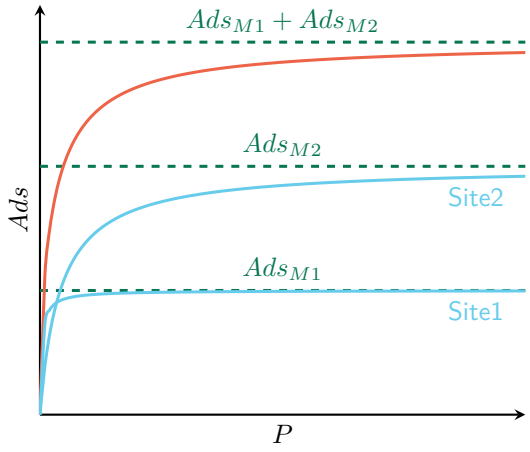

Figure 2.4: Dual-site Langmuir isotherm plot (orange) and the two individual Langmuir (light blue).

The curve has a linear low pressure pattern and reaches a high pressure plateau.

Langmuir-Freundlich Isotherm

In 1948, Robert Sips, proposed a new isotherm (Fig. 2.5). The initial idea was to create a versatile formula that would combine both Langmuir and Freundlich equations.[7]

Langmuir-Freundlich isotherm formula

$$Ads(P) = Ads_M \frac{(K_{LF} P)^t}{1 + (K_{LF} P)^t} \tag{2.10}$$

Ads_M is the maximum adsorbed quantity;

K_{LF} is the Langmuir-Freundlich constant;

t is function of the adsorption strength.

This new formula (also know as Sips isotherm) is a small correction of the Langmuir isotherm and modifies the shape of the curve at low pressure. The meaning of t is the same of the Freundlich isotherm and in the case of $t = 1$ equation 2.10 became equal to equation 2.1.

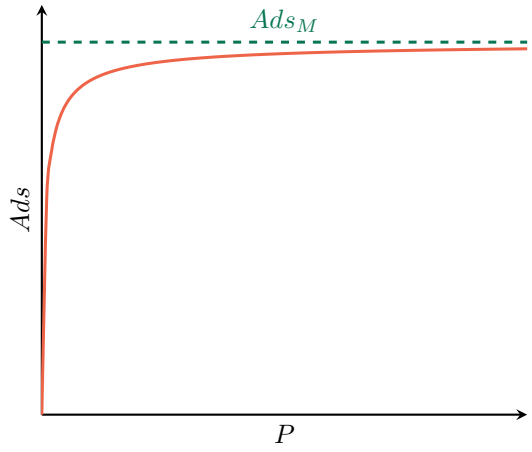

Figure 2.5: Langmuir-Freundlich isotherm plot.

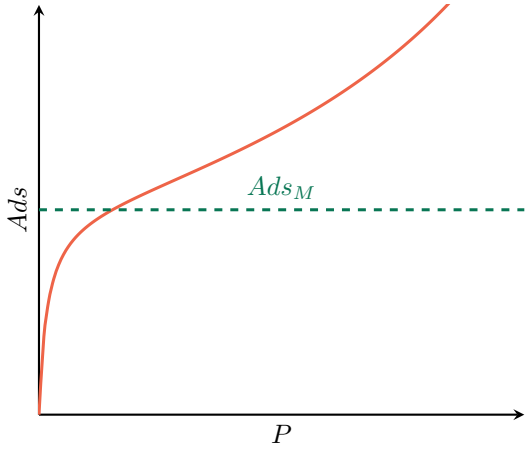

Figure 2.6: BET isotherm plot.

Multiple Adsorption Layers

The single-layer approximation in Langmuir's theory became a major source of error in the case of large pores. The adsorbed layer can interact strongly with gas causing new molecules to be adsorbed on it. In this case the Langmuir equation does not adapt to the experimental isotherm; for these situations there is another widely used adsorption theory.

BET Isotherm

The Brunauer-Emmett-Teller theory (Fig. 2.6) was proposed by the three scientist in 1938 to better describe multi-layer adsorption. It is a direct evolution of Langmuir's theory and has the same assumptions plus:

- A layer interact only with the adjacent ones.
- The second, third and higher layers have an heath of adsorption equal to the heath of fusion.
- Langmuir theory can be applied to each layer.

BET isotherm formula

$$Ads(P) = Ads_M \frac{(K_A P)}{(1 - K_B P)(1 - K_B P + K_A P)} \tag{2.11}$$

Ads_M is the maximum adsorbed quantity of a single layer;
K_A is the equilibrium constant of adsorption for first layer;
K_B is the equilibrium constant of adsorption for upper layers.[8]

This isotherm is commonly used to calculate the surface area of the sample,[4] but it is important to avoid any kind of extrapolation. We have to notice that:

$$\lim_{P \to \infty} Ads(P) = 0 \tag{2.12}$$

In the real case, this result is impossible, so the adsorbed values are not valid outside the experimental range.

Sigmoidal Isotherm

There is a rare isotherm, typical of few materials and also very useful for some applications. Its shape is very different from the other curves and implies a peculiar adsorption mechanism.

Sigmoidal isotherm formula

$$Ads(P) = Ads_M \frac{(KP)}{1 + KP + \frac{S}{P}} \tag{2.13}$$

Ads_M is the maximum adsorbed quantity;
K is the equilibrium constant of adsorption for first layer;
S is the sigmoidal factor.[9]

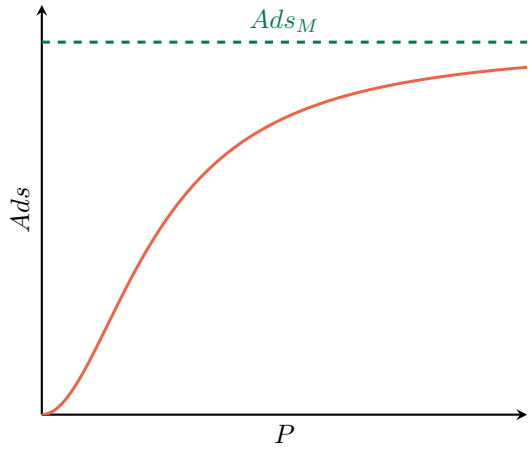

Figure 2.7: Sigmoidal isotherm plot.

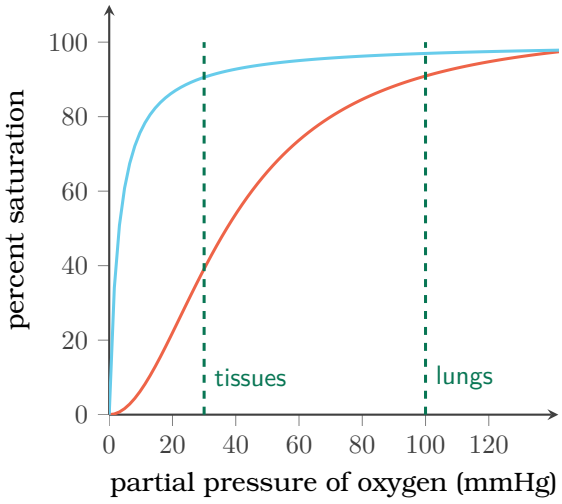

Figure 2.8: Binding isotherms for myoglobin (light blue) and hemoglobin (orange).

In figure 2.7, it is possible to see that at low pressure the behaviour is very similar to a Freundlich isotherm with $t > 1$ as shown in figure 2.3. The reason is that both isotherms try to simulate a cooperative adsorption, where the adsorbed molecules increase the surface affinity for the gas.[10]

Myoglobin vs Hemoglobin

This is a famous biological example that explain why sigmoidal adsorption behaviour is very important. In our body there are two protein designed to bind oxygen:myoglobin and hemoglobin. The main difference between them is that the former is composed of a single peptide chain while the hemoglobin is tetrameric; this difference plays a crucial role in their interaction with oxygen.

As shown in figure 2.8, myoglobin has a Langmuir adsorption and hemoglobin has a sigmoid one. If we observe the saturation at 100 mmHg of oxygen partial pressure (typical value within the lungs), myoglobin is completely saturated and hemoglobin is only at 90%. This is a demonstration that myoglobin is a better adsorbent for O_2 and is good for storage, but not for transport.

Efficient adsorption materials for the transport of gas need a big difference in adsorption between the two working pressures instead of a large absolute adsorption. Looking at figure 2.8, hemoglobin has lost 50% of saturation when it passes from lungs to tissues (oxygen partial pressure of 30 mmHg) but myoglobin has lost less than 10%. This makes hemoglobin an excellent oxygen carrier and this is its work inside human body. Myoglobin is used in muscles as an "emergency reservoir" in the case of intensive activity that causes a decrease in oxygen pressure within the tissues.

The sigmoidal shape is due, as already mentioned, to a cooperative adsorption. Hemoglobin has four oxygen adsorption sites and all have a low affinity for gas. When two sites are occupied, the whole protein changes its structure and this increases the affinity of the remaining adsorption sites. The entire process is reversible.[11]

It is not easy to generate such dynamic structures in the solid state: materials with low energy interaction (they must be in the same order as the heat of adsorption) but stable. So far, examples of those materials are rare and usually their discovery is based on serendipity. There are also other ways to obtain them, such as the controlled reversible collapse[12] or the introduction of dynamic elements such as molecular rotors.[13]

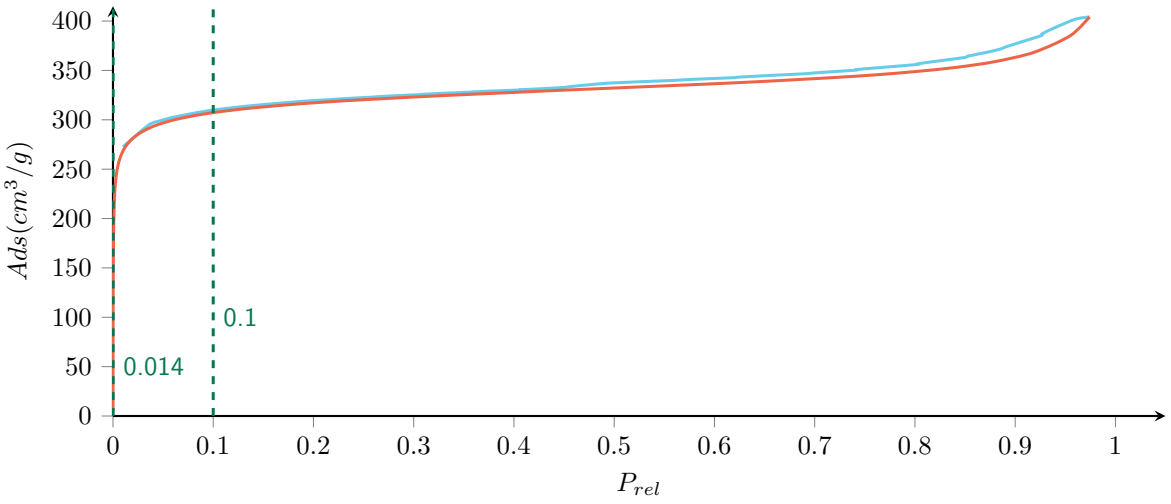

Figure 2.9: Isotherm for adsorption (orange) and desorption (light blue) of N_2 at 77 K.

2.2 Surface Area

One of the most important parameters of porous materials is the surface area. This is a good indicator of the area available for the gas adsorption. It is not an absolute indicator of how good the material is, we have already seen that the adsorption process involves many adsorbent/adsorbate interactions and layering, but indicates the potentiality of a structure surface area.

The measurement of this parameter is not trivial; the first and most important thing to choose is the probe gas. This must be small enough to enter each pore but not so small as to be absorbed, moreover it must be inert to the surface (no chemisorption). The choices are nitrogen and the noble gases. N_2 vapour at the liquid nitrogen boiling point of 77 K is the most frequently used adsorbate.[14]

Surface area is an intrinsic propriety so it should be independent of the choice of the adsorbate. In some cases even nitrogen is too large to be an appropriate probe, we are talking about ultramicroporosity (pore width < 0.7 nm). In these cases, good results are obtain with Argon at 87 K but below 0.4 nm also this gas fails to obtain a good surface area. The most suitable probe for ultramicroporosity is Helium at 4.2 K.[15]

We have two possible theories to analyse the experimental results and extrapolate the surface area. All the following formulas come directly from the dynamic theory behind the adsorption isotherms[16]

Langmuir Surface

From an experimental adsorption of N_2 at 77 K (Fig. 2.9) only some of the points are needed; in particular the relative pressure interval (P_{rel}) between 0.015 and 0.1 (in literature usually is between 0.05 and 0.35 but is not ideal for microporous materials).[16] The first thing to do is to convert the y-axis with the formula:

$$L = \frac{P_{rel}}{Ads[cm^3/g]} \tag{2.14}$$

The result must be something similar to figure 2.10. The plot is linear and is possible to define a slope (S) and an intercept (Y). In the case of some deviations we have to consider removing some points.

The final surface formula is:

Langmuir surface formula

$$Surface[m^2/g] = \frac{\sigma * 6.023 * 10^{23}}{22414 * 10^{18} * S} \tag{2.15}$$

Where σ is the analysis gas molecular cross-sectional area (for nitrogen is equal to 0.162 nm^2).

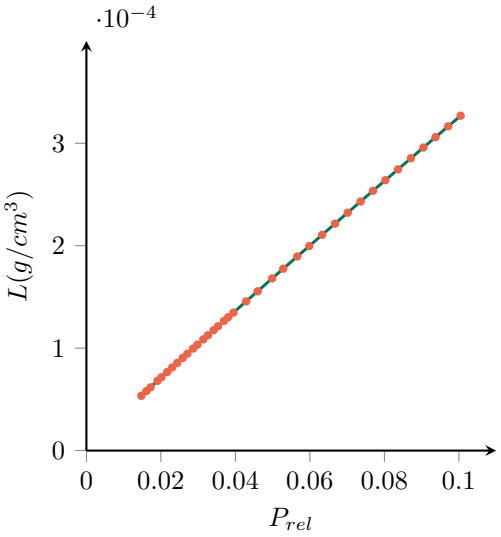

Figure 2.10: Isotherm for adsorptionn of N_2 at 77 K reduced and modified for Langmuir surface calculation.

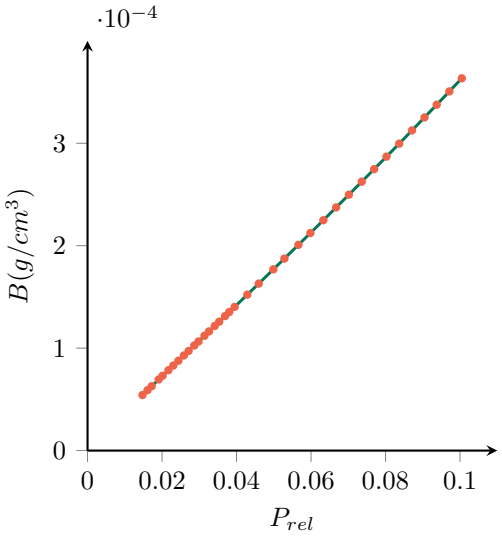

Figure 2.11: Isotherm for adsorption of N_2 at 77 K reduced and modified for BET surface calculation.

BET Surface

A large limitation of Langmuir's theory is the approximation of single layer adsorption, but often the pores are large enough to allow multilayer adsorption. In this case it is better to use the BET theory.

The procedure is similar to the previous calculation and also the pressure range, but instead of equation 2.14 we have to use:

$$B = \frac{P_{rel}}{Ads[cm^3/g](1 - P_{rel})} \tag{2.16}$$

Also in this case the plot is linear (Fig. 2.11). With these data is possible to calculate the BET surface with the formula:

BET surface formula

$$Surface[m^2/g] = \frac{\sigma * 6.023 * 10^{23}}{22414 * 10^{18} * (S + Y)} \tag{2.17}$$

Due to the fact that BET theory takes into account the multilayer adsorption, the surface calculated by this method is strictly less than the Langmuir surface.

2.3 Heat

The surface area is not sufficient to define a good material for adsorption, also the adsorbent/adsorbate interaction must be taken into account. Adsorption is an exothermic process and it releases energy. This parameter is known as isosteric heat of adsorption and is a direct indicator of the interaction between gas and surface. The greater is the energy, the stronger the interaction.[17]

Directly measuring the heat of adsorption is a bit complicated. Calorimetric measurement requires appropriate instrumentation and presents some accuracy and reproducibility issues. For these reasons often the data are extrapolated from the adsorption isotherms using appropriate calculations. In some cases (eg partial chemisorption) the direct measure remains the only way.[18]

Van't Hoff

Van't Hoff equation is a standard formula for the calculation of enthalpy (ΔH) studying the variation of equilibrium constant (k) with temperature:

$$\frac{d\ln(k)}{d(1/T)} = -\frac{\Delta H}{R} \tag{2.18}$$

Where R is the ideal gas constant.[19]

From Langmuir theory, we can define the adsorption-desorption equilibrium constant as:

$$k_{ads} = \frac{1}{K_L} = \frac{P(Ads_M - Ads)}{Ads} \tag{2.19}$$

The substitution of the previous formula in the van't Hoff equation is used to describe the equilibrium between adsorption and desorption. Such general equation yields three special cases: when the temperature is constant (isothermal), when the pressure is constant (isobaric), and a third case where the fraction of the surface covered is constant (isosteric). This last is the most used version and has the form of the Clausius-Clapeyron equation (using the vapour pressure to obtain the heat of vaporization).[20,21]

Its application is based on the creation of a curve improperly called Van't Hoff isochore from various experimental isotherms. By choosing a fixed value for the quantity adsorbed, it is necessary to plot natural log of the pressure against $1/T$. The resulting linear graph (Fig. 2.12) will follow the equation:

Van't Hoff isochore

$$\ln(P) = -\frac{\Delta H}{RT} + \frac{\Delta S}{R} \tag{2.20}$$

2.4 Selectivity

Selectivity is the ability of a material to adsorb one component preferably to one other when it is exposed to a mixture of gases. This propriety plays a key role in obtaining high purity gases. Nowadays the most used separation technique is cryogenic distillation, but is energy intensive. The possible alternatives (PSA, TSA, ...) are based on porous materials.[23]

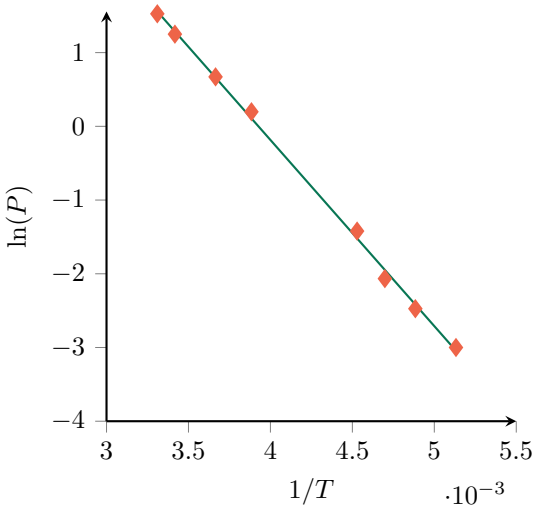

Figure 2.12: Example of Van't Hoff isochore.[22]

The selectivity is always considered between two gases at a specific total adsorption, temperature and mixture. If the value is greater than 1 the first gas is preferentially adsorbed, if it is below 1 the second gas is preferentially adsorbed. The thermodynamic selectivity decreases with the temperature for any adsorption values. At constant T, the selectivity changes with adsorption value in different ways depending on the size difference between adsorbates. For an heterogeneous adsorbent, selectivity decreases with loading.[24]

Henry's Law

The easiest way to measure selectivity between A and B is based on the Henry's gas law. For small amounts of adsorbed material the selectivity corresponds to the ratio of Henry's constants:

Henry Selectivity

$$S_{AB} = \frac{K_{HA}}{K_{HB}} \tag{2.21}$$

IAST

The ability to retain gases is considered of large interest for storage[25–28] and

purification[29,30]. In both cases the material must adsorb a gas mixture but the interactions are not the same for different molecules. Even in the case of storage of pure gases, the contribution of impurities is not always negligible .[31,32]

The measure of single-component adsorption isotherm is a simple automated task performed by specific instruments. The same is not always possible for mix adsorption isotherm[33] and it involves a large investment of time for results not so accurate as the pure gas isotherm .[31] For a complete characterization the isotherms must be acquired with different gases composition.

To overcome this problem, Myers and Prausnitz[34] developed the Ideal Adsorption Solution Theory (IAST). This thermodynamic theory predicts the adsorption isotherm of a mixture of gases starting from the single-component adsorption isotherms. IAST is widely used due to its success in predicting multicomponent adsorption in a wide variety of systems. A limitation of this theory is the approximation of ideal mixture. Other models try to overcame this limitation as the Predictive Real Adsorption Solution Theory (PRAST)[35] which introduces the activity coefficients to evaluate the interaction between gases. Another IAST limit is the need to use data outside the measured pressure range and this can cause some extrapolation error. To avoid this, some groups propose the simulation of adsorption isotherm via Transition Matrix Monte Carlo (TMMC) simulation.[36] Both these methods are based on IAST but greatly increase the complexity of the calculations; for this reason the ideal adsorption solution theory is widely used, despite its limitation.

IAST calculation

The IAST model is a powerful tool for predicting gas mixture adsorption starting from the experimental single gas adsorption isotherm.[34] The ideal assumption implies that the mixture of m gases is in equilibrium with the liquid phase. To achieve this, the spreading pressure (π_i) of each solute must be equal. Taking a function ($n_i^0(p_i)$) that describes how the material adsorbs the gas as a function of the gas pressure (p_i). This could be achieved fitting the experimental data with an ideal isotherm. Spreading pressure is defined as:

$$\pi_i(p_i^0) = \frac{RT}{A}\int_0^{p_i^0} n_i^0(p_i)\, d\ln p_i \tag{2.22}$$

R is the gas constant;
T is the absolute temperature;
A is the area occupied by the adsorbed phase.

The spreading pressure can be expressed as a reduced spreading pressure (π_i^*) in the case of a constant temperature and a constant specific surface:

Reduced Spreading Pressure

$$\pi_i^*(p_i^0) = \frac{A\pi_i(p_i^0)}{RT} = \int_0^{p_i^0} n_i^0(p_i)\, d\ln p_i \tag{2.23}$$

The formulas of some isotherms previously presented are shown in table 2.1. At equilibrium, all the m reduced spreading pressures are equal:

$$\pi_1^*(p_1^0) = \pi_2^*(p_2^0) = \cdots = \pi_m^*(p_m^0) \tag{2.24}$$

By Dalton's and Raoult's laws:

$$x_i = \frac{y_i P}{p_i^0} \tag{2.25}$$

y_i is the mole fraction of component i in the gas phase;
x_i is the mole fraction of component i in the adsorbed phase;
P is the total pressure of the gas mixture.
Considering:

$$\sum_{i=1}^{m} x_i = 1 \tag{2.26}$$

Only the right combination of p_i^0 solves equation 2.24 and 2.26 at a precise pressure P. The temperature of the

REDUCED SPREADING PRESSURE

Isotherm	Formula
Langmuir	$\pi^*(p^0) = Ads_M \ln(1 + K_L P)$
Henry†	$\pi^*(p^0) = K_H P$
Dual-site Langmuir	$\pi^*(p^0) = Ads_{M1} \ln(1 + K_{L1} P) + Ads_{M2} \ln(1 + K_{L2} P)$
Langmuir-Freundlich	$\pi^*(p^0) = Ads_M \frac{\ln(1+(K_{LF}P)^t)}{t}$
BET†	$\pi^*(p^0) = Ads_M \ln(\frac{1-K_B P+K_A P}{1-K_B P})$

† *divergent isotherm, use caution during extrapolation*

Table 2.1: Reduced spreading pressure of the main theoretical isotherms

adsorption isotherm of the mixture is the same as the experimental isotherms; the gas adsorption must be in molar unit (mol/g, cm^3/g,) and not mass. Now the values of x_i define the amount adsorbed by the material (n_T) with the formula:

$$\frac{1}{n_T} = \sum_{i=1}^{m} \frac{x_i}{n_i^0(p_i^0)} \tag{2.27}$$

And the quantity adsorbed of each gas is equal to:

$$n_i = x_i n_T \tag{2.28}$$

The selectivity at a precise total pressure is calculated as:

IAST Selectivity

$$S_{AB} = \frac{x_A / x_B}{y_A / y_B} \tag{2.29}$$

2.5 ADSORPTION SIMULATIONS

Computer simulation of the macroscopic proprieties of molecular fluids is a widely used technique. These simulations fall into two general categories: Molecular Dynamics (MD) and Monte Carlo (MC). While the former solves the equations of motion of the molecules to generate the configurations as a function of time, the latter generates configurations using a probabilistic approach. [37,38]

In adsorption studies the goal is to know the amount of adsorbed material as a function of the pressure and temperature. One possible approach is the use of the MD technique and simulating the experimental situation of an adsorbent in contact with the gas. Despite the theoretical validity of this approach, equilibration can takes several minutes or hours which translates into an unsustainable amount of computational time (a minute of experimental time takes on the order of 10^9 seconds on a computer). For this and other reasons, the MC method is the most used for adsorption simulations. [39]

In MC simulations, atoms are subject to random moves, which are accepted or rejected according to rules that, within the limit of a large number of trials, will produce configurations that corresponding to those in the desired statistical mechanical ensemble. [37]

Grand Canonical Monte Carlo Simulation

Grand canonical Monte Carlo (GCMC) simulation is a statistical-mechanical method, in which a rigorous molecular-level model of adsorption is solved exactly. GCMC simulation is widely used in the simulation of adsorption equilibrium, because it gives the number of moles of molecules in the pore directly.[40]

The simulation allows five different moves for the sorbate molecules inside the framework (that is always considered rigid):[41]

- *Translation*: moves the center of mass.
- *Rotation*: rotates about the center of mass.
- *Regrowth*: removes the molecule and reintroduces it with a random position and orientation.
- *Conformer*: changes the conformation.
- *Exchange*: creates a new sorbate and deletes an existing molecules.

The Monte Carlo algorithm can be simplified using the Metropolis method. This variation allows any move that reduces the total energy of the system but, if the energy increases, the move is randomly accepted. The more the energy increases, the less likely the move is accepted.[42]

GCMC simulation has been widely used for the determination of the possible adsorption capability of porous materials starting from their crystal structure. An important feature of this simulation is the possibility to simulate the adsorption of gas mixtures, offering a valid alternative to IAST.[43,44] However, the rigidity of the crystal during the simulation limits its use in very flexible systems.[45,46]

Grand Canonical Ensemble

For adsorption studies, a natural ensemble to use is the grand canonical ensemble (or μ, V, T ensemble) where chemical potential, volume and temperature are fixed. In the experimental setup the adsorbed gas is in equilibrium with the gas in the reservoir; in other words the chemical potential and temperature of the gas inside and outside the adsorbent are the same. The main difference with other ensembles is that the total number of particles is allowed to fluctuate during the simulation.[39]

Force Field

The force field is a very simple empirical approximation of the physics that should be properly expressed in terms of quantum mechanics, but is totally unmanageable in that form.[47]

Usually the force fields are limited to particular combination of atoms or fit types of structures (like CVFF for proteins and CHARMM for nucleid acids).[48] A wide variety of force field that can be applied to zeolites exist, their use depends on the computational task.[49]

MOFs are newly developed materials that are of great interest for the scientific community but they lack a dedicated force field. There are some examples of successful simulations using the Dreiding and the Universal Force Field (UFF).[50,51] Recently, a dedicated extension of the UFF was proposed (UFF4MOF).[52]

Parameters

For the adsorption simulations on MOFs (like the one presented in Fig. 6.11) we used GCMC Metropolis method and Dreiding force field. The Lennard-Jones cut-off distance for CO_2 was set to 13 Å[53] and the simulation box was formed by a supercell with all dimensions at least twice the cut-off distance. All simulations include $2 * 10^6$ cycles equilibration period and $1 * 10^7$ cycles of production for each pressure. The Ewald sum technique was used to compute the electrostatic interactions.[51,54]

Bibliography

[1] Saadi, R.; Saadi, Z.; Fazaeli, R.; Fard, N. E. Monolayer and multilayer adsorption isotherm models for sorption from aqueous media. *Korean Journal of Chemical Engineering* **2015**, *32*, 787–799.

[2] Kayser, H. Ueber die verdichtung von gasen an oberflächen in ihrer abhängigkeit von druck und temperatur. *Annalen der Physik* **1881**, *248*, 526–537.

[3] Dunne, L. J.; Manos, G. *Adsorption and Phase Behaviour in Nanochannels and Nanotubes*; Springer Netherlands, 2010; pp 1–8.

[4] Ruthven, D. M. *Principles of Adsorption and Adsorption Processes*; Wiley-Interscience, 1984.

[5] Hoda, N. *Innovations in Chemical Biology*; Springer, 2009; pp 213–223.

[6] Dada, A.; Olalekan, A.; Olatunya, A.; Dada, O. Langmuir, Freundlich, Temkin and Dubinin–Radushkevich isotherms studies of equilibrium sorption of Zn^{2+} unto phosphoric acid modified rice husk. *IOSR Journal of Applied Chemistry* **2012**, *3*, 38–45.

[7] Sips, R. On the Structure of a Catalyst Surface. *The Journal of Chemical Physics* **1948**, *18*, 1024–1026.

[8] Ebadi, A.; Mohammadzadeh, J. S. S.; Khudiev, A. What is the correct form of BET isotherm for modeling liquid phase adsorption? *Adsorption* **2009**, *15*, 65–73.

[9] Limousin, G.; Gaudet, J.-P.; Charlet, L.; Szenknect, S.; Barthes, V.; Krimissa, M. Sorption isotherms: a review on physical bases, modeling and measurement. *Applied Geochemistry* **2007**, *22*, 249–275.

[10] Butt, H.-J.; Graf, K.; Kappl, M. *Physics and Chemistry of Interfaces*; Wiley-VCH Verlag GmbH & Co. KGaA, 2003.

[11] Bhagavan, N. V. *Medical Biochemistry, Fourth Edition*; Academic Press, 2001.

[12] Baroncini, M.; d'Agostino, S.; Bergamini, G.; Ceroni, P.; Comotti, A.; Sozzani, P.; Bassanetti, I.; Grepioni, F.; Hernandez, T. M.; Silvi, S.; Venturi, M.; Credi, A. Photoinduced reversible switching of porosity in molecular crystals based on star-shaped azobenzene tetramers. *Nature Chemistry* **2015**, *7*, 634–640.

[13] Comotti, A.; Bracco, S.; Sozzani, P. Molecular rotors built in porous materials. *Accounts of Chemical Research* **2016**, *49*, 1701–1710.

[14] Chiou, C. T. *Partition and Adsorption of Organic Contaminants in Environmental Systems*; Wiley-Interscience, 2002.

[15] Lowell, S.; Shields, J. E.; Thomas, M. A.; Thommes, M. *Characterization of Porous Solids and Powders: Surface Area, Pore Size and Density*; Springer, 2010.

[16] Lowell, S.; Shields, J. E. *Powder Surface Area and Porosity*; Springer, 2010.

[17] *Handbook of Solid State Chemistry,Volume Set*; Wiley-VCH, 2017.

[18] Wu, D.; Gassensmith, J. J.; Gouvêa, D.; Ushakov, S.; Stoddart, J. F.; Navrotsky, A. Direct calorimetric measurement of enthalpy of adsorption of carbon dioxide on CD-MOF-2, a green metal–organic framework. *Journal of the American Chemical Society* **2013**, *135*, 6790–6793.

[19] Broom, D. P. *Hydrogen Storage Materials: the Characterisation of their Storage Properties*; Springer Science & Business Media, 2011.

[20] Rowley, M. M.; Innes, W. B. Application of the van't Hoff equation to adsorption equilibra. *Proceedings of the Iowa Academy of Science* **194.**, *47*, 165–170.

[21] Do, D. D. *Adsorption Analysis: Equilibria And Kinetics*; Series On Chemical Engineering; World Scientific Publishing Company, 1998.

[22] Yang, S.; Lin, X.; Lewis, W.; Suyetin, M.; Bichoutskaia, E.; Parker, J. E.; Tang, C. C.; Allan, D. R.; Rizkallah, P. J.; Hubberstey, P.; Champness, N. R.; Thomas, K. M.; Blake, A. J.; Schröder, M. A partially interpenetrated metal–organic framework for selective hysteretic sorption of carbon dioxide. *Nature Materials* **2012**, *11*, 710–716.

[23] Pillai, R. S.; Pinto, M. L.; Pires, J.; Jorge, M.; Gomes, J. R. B. Understanding gas adsorption selectivity in IRMOF-8 Using molecular simulation. *ACS Applied Materials & Interfaces* **2015**, *7*, 624–637.

[24] Lee, S.; Henthorn, K. *Particle Technology and Applications*; Green Chemistry and Chemical Engineering; CRC Press, 2016.

[25] Yang, Q.; Guillerm, V.; Ragon, F.; Wiersum, A. D.; Llewellyn, P. L.; Zhong, C.; Devic, T.; Serre, C.; Maurin, G. CH_4 storage and CO_2 capture in highly porous zirconium oxide based metal-organic frameworks. *Chemical Communications* **2012**, *48*, 9831–9833.

[26] Hirscher, M.; Panella, B.; Schmitz, B. Metal-organic frameworks for hydrogen storage. *Microporous and mesoporous materials* **2010**, *129*, 335–339.

[27] Xia, Y.; Yang, Z.; Zhu, Y. Porous carbon-based materials for hydrogen storage: advancement and challenges. *Journal of Materials Chemistry A* **2013**, *1*, 9365–9381.

[28] Makal, T. A.; Li, J.-R.; Lu, W.; Zhou, H.-C. Methane storage in advanced porous materials. *Chemical Society Reviews* **2012**, *41*, 7761–7779.

[29] Li, J.-R.; Kuppler, R. J.; Zhou, H.-C. Selective gas adsorption and separation in metal-organic frameworks. *Chemical Society Reviews* **2009**, *38*, 1477–1504.

[30] Samanta, A.; Zhao, A.; Shimizu, G. K.; Sarkar, P.; Gupta, R. Post-combustion CO_2 capture using solid sorbents: a review. *Industrial & Engineering Chemistry Research* **2011**, *51*, 1438–1463.

[31] Talu, O. Needs, status, techniques and problems with binary gas adsorption experiments. *Advances in Colloid and Interface Science* **1998**, *76*, 227–269.

[32] Schlapbach, L.; Züttel, A. Hydrogen-storage materials for mobile applications. *Nature* **2001**, *414*, 353–358.

[33] Talu, O. Measurement and analysis of mixture adsorption equilibrium in porous solids. *Chemie Ingenieur Technik* **2011**, *83*, 67–82.

[34] Myers, A.; Prausnitz, J. M. Thermodynamics of mixed-gas adsorption. *AIChE Journal* **1965**, *11*, 121–127.

[35] Sakuth, M.; Meyer, J.; Gmehling, J. Measurement and prediction of binary adsorption equilibria of vapors on dealuminated Y-zeolites (DAY). *Chemical Engineering and Processing: Process Intensification* **1998**, *37*, 267–277.

[36] Chen, H.; Sholl, D. S. Examining the accuracy of ideal adsorbed solution theory without curve-fitting using transition matrix Monte Carlo simulations. *Langmuir* **2007**, *23*, 6431–6437.

[37] D, D. *Adsorption Science and Technology, 2nd Pacific Basin Conference*; World Scientific Publishing Company, 2000.

[38] Dąbrowski, A. Adsorption - from theory to practice. *Advances in Colloid and Interface Science* **2001**, *93*, 135–224.

[39] Frenkel, D.; Smit, B. *Understanding Molecular Simulation: From Algorithms to Applications*; Computational science; Elsevier Science, 2001.

[40] Yun, J.-H.; He, Y.; Otero, M.; Düren, T.; Seaton, N. *Characterization of Porous Solids VI, Proceedings of the 6th International Symposium on the Characterization of Porous Solids (COPS-VI)*; Elsevier, 2002; pp 685–692.

[41] Akkermans, R. L.; Spenley, N. A.; Robertson, S. H. Monte Carlo methods in Materials Studio. *Molecular Simulation* **2013**, *39*, 1153–1164.

[42] Masel, R. *Principles of Adsorption and Reaction on Solid Surfaces*; Wiley Series in Chemical Engineering; Wiley, 1996.

[43] Jiang, J. *Metal-Organic Frameworks: Materials Modeling towards Engineering Applications*; Jenny Stanford Publishing, 2015.

[44] Catlow, C.; Van Speybroeck, V.; van Santen, R. *Modelling and Simulation in the Science of Micro- and Meso-Porous Materials*; Elsevier Science, 2017.

[45] Greathouse, J. A.; Kinnibrugh, T. L.; Allendorf, M. D. Adsorption and separation of noble gases by IRMOF-1: grand canonical monte carlo simulations. *Industrial & Engineering Chemistry Research* **2009**, *48*, 3425–3431.

[46] Vandenbrande, S.; Verstraelen, T.; Gutiérrez-Sevillano, J. J.; Waroquier, M.; Speybroeck, V. V. Methane adsorption in Zr-based MOFs: comparison and critical evaluation of force fields. *The Journal of Physical Chemistry C* **2017**, *121*, 25309–25322.

[47] Council, N.; Studies, D.; Sciences, C.; Modeling, C. *Computer Assisted Modeling: Contributions of Computational Approaches to Elucidating Macromolecular Structure and Function*; National Academies Press, 1987.

[48] Gubbins, K.; Quirke, N. *Molecular Simulation and Industrial Applications: Methods, Examples, and Prospects*; Current topics in molecular simulation; Gordon and Breach Science Publishers, 1996.

[49] Cejka, J.; Corma, A.; Zones, S. *Zeolites and Catalysis: Synthesis, Reactions and Applications*; Wiley, 2010.

[50] Yazaydın, A. O.; Snurr, R. Q.; Park, T.-H.; Koh, K.; Liu, J.; LeVan, M. D.; Benin, A. I.; Jakubczak, P.; Lanuza, M.; Galloway, D. B.; Low, J. J.; Willis, R. R. Screening of metal-organic frameworks for carbon dioxide capture from flue gas using a combined experimental and modeling approach. *Journal of the American Chemical Society* **2009**, *131*, 18198–18199.

[51] Basdogan, Y.; Sezginel, K. B.; Keskin, S. Identifying highly selective metal organic frameworks for CH_4/H_2 separations using computational tools. *Industrial & Engineering Chemistry Research* **2015**, *54*, 8479–8491.

[52] Addicoat, M. A.; Vankova, N.; Akter, I. F.; Heine, T. Extension of the universal force field to metal-organic frameworks. *Journal of Chemical Theory and Computation* **2014**, *10*, 880–891.

[53] Becker, T. M.; Heinen, J.; Dubbeldam, D.; Lin, L.-C.; Vlugt, T. J. H. Polarizable force fields for CO_2 and CH_4 adsorption in M-MOF-74. *The Journal of Physical Chemistry C* **2017**, *121*, 4659–4673.

[54] Kim, K. C.; Yoon, T.-U.; Bae, Y.-S. Applicability of using CO_2 adsorption isotherms to determine BET surface areas of microporous materials. *Microporous and Mesoporous Materials* **2016**, *224*, 294–301.

3. Molecular Rotors

Create an atomic engine scale is a fascinating idea. To achieve such goal, rotational control is one of the most desirable features. It is common to see rotation in molecules in solution, for example around a single bond, but controlling it is not an easy task.[1]

The interest for these studies is growing, thanks also to the Nobel Prize in Chemistry 2016 to J.P. Sauvage, J.F. Stoddart and B.L. Feringa for the design and synthesis of molecular machines. The potential applications are innumerable and could define the future of nanotechnology.

3.1 Rotor Structure

A molecular rotor is a molecule that contains two or more moieties that rotate relative to each other. The rotor consists in three main parts: rotator, axle and stator (Fig. 3.1). The rotator is the portion of the molecule that rotate while the stator is the static part. Distinguishing rotator and stator is not easy, especially in solution. Usually the stator is defined as the part with major inertia. The axle is the connection between rotator and stator.[1]

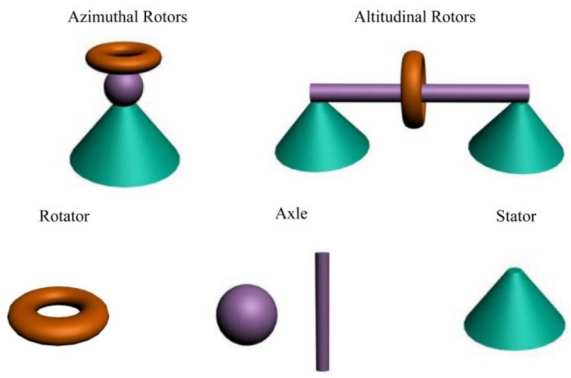

Figure 3.1: Classification for surface mounted molecular rotors showing azimuthal and altitudinal rotors. Each component make up the rotor is shown below.[2]

3.2 Biological Rotors

Biomolecular machines are very common in nature and have an astounding level of complexity and efficiency. A common examples is the muscles, in which the myosin rotor can move along an actin filament.[3,4] This small system is repeated in three dimensions to form the sarcomeres. Muscle contraction is just the macroscopic result of the nanoscale movement of thousands of molecular rotor. Other interesting motors are the kinesins, responsible for the transport of organelle and proteins. They perform this task walking along microtubules.[3,4]

The most famous, useful and sophisticated biomolecular motor is the ATP synthase.[3,4] It is ubiquitous in all kinds of mammalian cells and uses a proton gradient for the synthesis of ATP. It can also do the opposite and use ATP to generate a proton gradient. Without going into details; a rotor activates different catalytic sites where ADP is transform into ATP. The proton gradient provides the energy for the unidirectional rotation.

3.3 Synthetic Rotors

It is possible to create synthetic molecular motors, even if they lack the complexity and efficiency of the biological counterparts. So far, the only devices that use molecular scale motion are liquid crystals.[5] Thanks to an enormous research efforts in this field we are seeing increasingly complex systems that could one day be widely used.

Surface

The solution phase is the ideal medium to study the structure, function and dynamics of molecular machines. The spectrum of possibilities is wide and full of

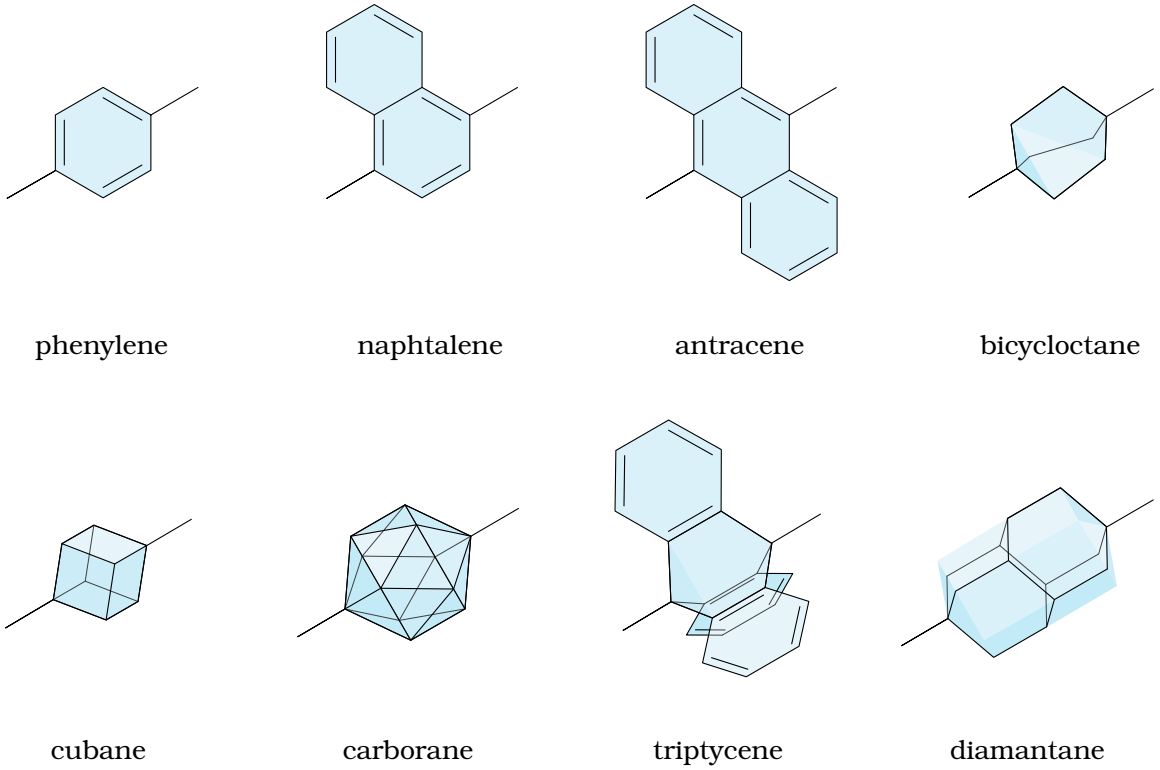

Figure 3.2: Some examples of molecular rotors used in porous systems. [10,11]

synthetic challenges. The main limitation is the complete absence of coordinate and cooperative motion that is required for a functional device. One way to overcome this problem is to attach the rotor to a surface, giving order to the system.

Motion of the molecule can be altered by the surface interaction, therefore the knowledge of molecular properties in liquid phase cannot be transferred to condense matter. Furthermore, the analysis of surface molecules can be particularly challenging. [1]

Despite the difficulties, there are already surprising results in this field such as the molecular muscle, [6,7] the nanocar [8] and the unidirectional rotor. [9]

Porous Systems

Matter in the solid state tends to be compact and with a very limited dynamic. However, some materials present pores that are often used for adsorption as previously explained. The free volume can also be used to allow motion of the structure itself and create a molecular rotor.

The principle is well documented in amorphous materials such as polymers above glass transition. [12,13] The main step was the application to materials with a permanent porosity and sufficient stability. Thanks to the discovery of new porous materials, it is now possible to find molecular rotors in structures with different nature and pore dimensions. [14]

In figure 3.2 are presented some common molecular rotors in porous materials. It is possible to notice that they are all "structural" rotors, which contribute to support the structure itself (for example as part of a linker in a MOF). These rotors often have a triple bond between them and the structure to increase mobility, potentially generating a free rotation motion. [10]

The rotors shown can be heavily modified, a common example is the substitution of hydrogen with fluorine but there are examples of more drastic modification. [15]

Substitution is a major interest in this

field because it allows the creation of dipolar molecular rotors which can lead to switchable ferroelectric materials, radiowave filters and much more.[14]

3.4 Applications

Talking about applications of molecular rotors is a little premature. These elements are, although recently discovered, and are not yet used in everyday life. However, there are several promising researches on possible future applications. The possibility of combining dynamics with solid state stability has attracted many scientists. Most projects are at an early stage but show some potential.

Compasses

A molecular rotor con be partially functionalized to generate a permanent electric dipole moment. Such rotors are often referred to as molecular compasses.[16,17] These can potentially be influenced by electric, magnetic and optical stimuli; for this reason they are of great interest for the design of electro-optical materials.[18,19]

An ordered array of dipoles could cause some interesting physical phenomena. It has already been demonstrated that 2D arrays of dipoles can manifest an orientational phase transition.[20] Dipole-dipole interactions between rotors could propagate molecular rotary waves at much lower speeds than typical phonon velocities.[21] This behaviour could be applied to radio frequency filters similar to those that now employ surface acoustic waves.[5,17] The dimensions of the device are determined in part by the speed of sound in the material and a slower propagation is related to smaller functional systems. Rotary wave excitation can be precisely regulated by controlling the dipole interactions.[22]

2D arrays of rotors are usually made by inclusion of molecular rotors as guests in a porous crystal. The most common host is TPP (tris-*o*-(phenylenedioxy)cyclotriposphazene), a hexagonal molecular crystal with a structure made of parallel hollow channels with a diameter of 5 Å located 11.5 Å apart.[23–25] The possible guests came in very different shapes, with both surface and bulk rotors.[26–28] Many arrays have been studied for the search of a ferroelectric transition, despite it is predicted by the theory this transition has not been observed probably due to disorder or an excessively high rotational barrier.[22]

Another possible use is the creation of ferroelectric materials. Ferroelectricity in these systems can be attributed to the cooperative motions of atoms or polar components in crystal lattices.[29] The problem is, of course, to generate this cooperative motion because molecular rotors tend to rotate randomly. For these reasons, the system must be balanced to have a rotational barrier high enough to freeze the rotor in position but not so high to completely hinder rotation. The most common molecular rotor for ferroelectricity is DABCO (1,4-diazabicyclo[2.2.2]octane) which has been used successfully in a considerable amount of materials.[30–33]

Adsorption

Another important research regarding molecular rotors is the control of gas adsorption. Porous materials are excellent for gas storage and separation but the tunability is particularly low. The addition of elements with very high dynamics such as molecular rotors can be used to modify the adsorption behaviour. The idea of this application for molecular rotors is relatively recent and follows the growing interest for porous materials.

It has already been demonstrated that the presence of the rotor strongly affects the diffusion of guest molecules in the pores,[34,35] but the interaction between these two dynamical elements is more complex. The presence of the gas reversibly alters the motion of the rotor, in a way that depends on the nature of gas and

rotor.[36–38] It appears that iodine has the highest stopping power, especially for *p*-phenyl rotors.[14] Also the gas motion in the restricted pore space can be very complex and not easy to study.[39–42]

The presence of a molecular rotor in the crystal structure can lead to a peculiar adsorption behaviour. Various examples of gate openings have been reported[43,44] and also selectivity seems to be greatly affected.[45] Rotors can also have positive interactions with the gas molecules, thus managing to store high amount of gases even at low pressure.

Bibliography

[1] Goddard, W.; Brenner, D.; Lyshevski, S.; Iafrate, G. *Handbook of Nanoscience, Engineering, and Technology*; Electrical Engineering Handbook; CRC Press, 2007.

[2] Xue, M.; Wang, K. L. Molecular rotors as switches. *Sensors* **2012**, *12*, 11612–11637.

[3] Kinbara, K.; Aida, T. Toward intelligent molecular machines: directed motions of biological and artificial molecules and assemblies. *Chemical Reviews* **2005**, *105*, 1377–1400.

[4] Meisenberg, G.; Simmons, W. *Principles of Medical Biochemistry*; Elsevier Health Sciences, 2011.

[5] Michl, J.; Sykes, E. C. H. Molecular rotors and motors: recent advances and future challenges. *ACS Nano* **2009**, *3*, 1042–1048.

[6] Huang, T. J.; Brough, B.; Ho, C.-M.; Liu, Y.; Flood, A. H.; Bonvallet, P. A.; Tseng, H.-R.; Stoddart, J. F.; Baller, M.; Magonov, S. A nanomechanical device based on linear molecular motors. *Applied Physics Letters* **2004**, *85*, 5391–5393.

[7] Juluri, B. K.; Kumar, A. S.; Liu, Y.; Ye, T.; Yang, Y.-W.; Flood, A. H.; Fang, L.; Stoddart, J. F.; Weiss, P. S.; Huang, T. J. A mechanical actuator driven electrochemically by artificial molecular muscles. *ACS Nano* **2009**, *3*, 291–300.

[8] Kudernac, T.; Ruangsupapichat, N.; Parschau, M.; Maciá, B.; Katsonis, N.; Harutyunyan, S. R.; Ernst, K.-H.; Feringa, B. L. Electrically driven directional motion of a four-wheeled molecule on a metal surface. *Nature* **2011**, *479*, 208–211.

[9] van Delden, R. A.; ter Wiel, M. K. J.; Pollard, M. M.; Vicario, J.; Koumura, N.; Feringa, B. L. Unidirectional molecular motor on a gold surface. *Nature* **2005**, *437*, 1337–1340.

[10] Gonzalez-Nelson, A.; Coudert, F.-X.; van der Veen, M. Rotational dynamics of linkers in Metal–Organic Frameworks. *Nanomaterials* **2019**, *9*, 330.

[11] Karlen, S. D.; Reyes, H.; Taylor, R. E.; Khan, S. I.; Hawthorne, M. F.; Garcia-Garibay, M. A. Symmetry and dynamics of molecular rotors in amphidynamic molecular crystals. *Proceedings of the National Academy of Sciences* **2010**, *107*, 14973–14977.

[12] Sozzani, P.; Bracco, S.; Comotti, A.; Simonutti, R. *Interphases and Mesophases in Polymer Crystallization II*; Advances in polymer science; Springer Berlin Heidelberg, 2005; Chapter 4, pp 153–177.

[13] Bovey, F.; Mirau, P.; Gutowsky, H. *Nuclear Magnetic Resonance Spectroscopy*; Elsevier Science, 1988.

[14] Comotti, A.; Bracco, S.; Sozzani, P. Molecular rotors built in porous materials. *Accounts of Chemical Research* **2016**, *49*, 1701–1710.

[15] Rodriguez-Molina, B.; Ochoa, M. E.; Farfan, N.; Santillan, R.; Garcia-Garibay, M. A. Synthesis, characterization, and rotational dynamics of crystalline molecular compasses with N-heterocyclic rotators. *The Journal of Organic Chemistry* **2009**, *74*, 8554–8565.

[16] Dominguez, Z.; Khuong, T.-A. V.; Dang, H.; Sanrame, C. N.; Nuñez, J. E.; Garcia-Garibay, M. A. Molecular compasses and gyroscopes with polar rotors: synthesis and characterization of crystalline forms. *Journal of the American Chemical Society* **2003**, *125*, 8827–8837.

[17] Horansky, R. D.; Clarke, L. I.; Winston, E. B.; Price, J. C.; Karlen, S. D.; Jarowski, P. D.; Santillan, R.; Garcia-Garibay, M. A. Dipolar rotor-rotor interactions in a difluorobenzene molecular rotor crystal. *Physical Review B* **2006**, *74*.

[18] Dominguez, Z.; Dang, H.; Strouse, M. J.; Garcia-Garibay, M. A. Molecular "compasses" and "gyroscopes". I. Expedient synthesis and solid dtate dynamics of an open rotor with a bis(triarylmethyl) frame. *Journal of the American Chemical Society* **2002**, *124*, 2398–2399.

[19] Winston, E. B.; Lowell, P. J.; Vacek, J.; Chocholoušová, J.; Michl, J.; Price, J. C. Dipolar molecular rotors in the metal-organic framework crystal IRMOF-2. *Physical Chemistry Chemical Physics* **2008**, *10*, 5188.

[20] Kim, K.; Sullivan, N. S. Orientational behavior of quantum rotors physisorbed on boron nitride. *Physical Review B* **1997**, *55*, R664–R667.

[21] de Jonge, J. J.; Ratner, M. A.; de Leeuw, S. W.; Simonis, R. O. Molecular dipole chains III: energy transfer. *The Journal of Physical Chemistry B* **2004**, *108*, 2666–2675.

[22] Credi, A.; Silvi, S.; Venturi, M. *Molecular Machines and Motors: Recent Advances and Perspectives*; Topics in Current Chemistry; Springer International Publishing, 2014.

[23] Allcock, H. R.; Siegel, L. A. Phosphonitrilic compounds. III. Molecular inclusion compounds of tris(o-phenylenedioxy)phosphonitrile trimer. *Journal of the American Chemical Society* **1964**, *86*, 5140–5144.

[24] Sozzani, P.; Comotti, A.; Simonutti, R.; Meersmann, T.; Logan, J. W.; Pines, A. A porous crystalline molecular solid explored by hyperpolarized xenon. *Angewandte Chemie International Edition* **2000**, *39*, 2695–2699.

[25] Sozzani, P.; Bracco, S.; Comotti, A.; Ferretti, L.; Simonutti, R. Methane and carbon dioxide storage in a porous van der waals crystal. *Angewandte Chemie International Edition* **2005**, *44*, 1816–1820.

[26] Kobr, L.; Zhao, K.; Shen, Y.; Comotti, A.; Bracco, S.; Shoemaker, R. K.; Sozzani, P.; Clark, N. A.; Price, J. C.; Rogers, C. T.; Michl, J. Inclusion compound based approach to arrays of artificial dipolar molecular rotors. a surface inclusion. *Journal of the American Chemical Society* **2012**, *134*, 10122–10131.

[27] Kobr, L.; Zhao, K.; Shen, Y.; Polívková, K.; Shoemaker, R. K.; Clark, N. A.; Price, J. C.; Rogers, C. T.; Michl, J. Inclusion compound based approach to arrays of artificial dipolar molecular rotors: bulk inclusions. *The Journal of Organic Chemistry* **2012**, *78*, 1768–1777.

[28] Kobr, L.; Zhao, K.; Shen, Y.; Shoemaker, R. K.; Rogers, C. T.; Michl, J. Inclusion compound based approach to forming arrays of artificial dipolar molecular rotors: a search for optimal rotor structures. *Advanced Materials* **2012**, *25*, 443–448.

[29] Mitsui, T.; Tatsuzaki, I.; Nakamura, E. *An Introduction to the Physics of Ferroelectrics*; Ferroelectricity and related phenomena; Gordon and Breach Science Publishers, 1976.

[30] Akutagawa, T.; Koshinaka, H.; Sato, D.; Takeda, S.; Noro, S.-I.; Takahashi, H.; Kumai, R.; Tokura, Y.; Nakamura, T. Ferroelectricity and polarity control in solid-state flip-flop supramolecular rotators. *Nature Materials* **2009**, *8*, 342–347.

[31] Hang, T.; Zhang, W.; Ye, H.-Y.; Xiong, R.-G. Metal-organic complex ferroelectrics. *Chemical Society Reviews* **2011**, *40*, 3577.

[32] Zhang, W.; Xiong, R.-G. Ferroelectric metal-organic frameworks. *Chemical Reviews* **2011**, *112*, 1163–1195.

[33] Zhang, Y.; Zhang, W.; Li, S.-H.; Ye, Q.; Cai, H.-L.; Deng, F.; Xiong, R.-G.; Huang, S. D. Ferroelectricity induced by ordering of twisting motion in a molecular rotor. *Journal of the American Chemical Society* **2012**, *134*, 11044–11049.

[34] Devautour-Vinot, S.; Maurin, G.; Serre, C.; Horcajada, P.; da Cunha, D. P.; Guillerm, V.; de Souza Costa, E.; Taulelle, F.; Martineau, C. Structure and dynamics of the functionalized MOF type UiO-66(Zr): NMR and dielectric relaxation spectroscopies coupled with DFT calculations. *Chemistry of Materials* **2012**, *24*, 2168–2177.

[35] Jiang, X.; Duan, H.-B.; Khan, S. I.; Garcia-Garibay, M. A. Diffusion-controlled rotation of triptycene in a metal-organic framework (MOF) sheds light on the viscosity of MOF-confined solvent. *ACS Central Science* **2016**, *2*, 608–613.

[36] Comotti, A.; Bracco, S.; Valsesia, P.; Beretta, M.; Sozzani, P. Fast molecular rotor dynamics modulated by guest inclusion in a highly organized nanoporous organosilica. *Angewandte Chemie International Edition* **2010**, *49*, 1760–1764.

[37] Comotti, A.; Bracco, S.; Yamamoto, A.; Beretta, M.; Hirukawa, T.; Tohnai, N.; Miyata, M.; Sozzani, P. Engineering switchable rotors in molecular crystals with open porosity. *Journal of the American Chemical Society* **2014**, *136*, 618–621.

[38] Comotti, A.; Bracco, S.; Ben, T.; Qiu, S.; Sozzani, P. Molecular rotors in porous organic frameworks. *Angewandte Chemie International Edition* **2014**, *53*, 1043–1047.

[39] Chen, S.; Lucier, B. E.; Boyle, P. D.; Huang, Y. Understanding the fascinating origins of CO_2 adsorption and dynamics in MOFs. *Chemistry of Materials* **2016**, *28*, 5829–5846.

[40] Witherspoon, V. J.; Xu, J.; Reimer, J. A. Solid-state NMR investigations of carbon dioxide gas in metal-organic frameworks: insights into molecular motion and adsorptive behavior. *Chemical Reviews* **2018**, *118*, 10033–10048.

[41] Desveaux, B. E.; Wong, Y. T. A.; Lucier, B. E. G.; Terskikh, V. V.; Boyle, P. D.; Jiang, S.; Huang, Y. CO_2 behavior in a highly selective ultramicroporous framework: insights from single-crystal X-ray diffraction and solid-state nuclear magnetic resonance spectroscopy. *The Journal of Physical Chemistry C* **2019**, *123*, 17798–17807.

[42] Wu, B.; Wong, Y. T. A.; Lucier, B. E. G.; Boyle, P. D.; Huang, Y. Exploring host-guest interactions in the α-$Zn_3(HCOO)_6$ metal-organic framework. *ACS Omega* **2019**, *4*, 4000–4011.

[43] Seo, J.; Matsuda, R.; Sakamoto, H.; Bonneau, C.; Kitagawa, S. A pillared-layer coordination polymer with a rotatable pillar acting as a molecular gate for guest molecules. *Journal of the American Chemical Society* **2009**, *131*, 12792–12800.

[44] Banerjee, D.; Wang, H.; Plonka, A. M.; Emge, T. J.; Parise, J. B.; Li, J. Direct structural identification of gas induced gate-opening coupled with commensurate adsorption in a microporous metal-organic framework. *Chemistry - A European Journal* **2016**, *22*, 11816–11825.

[45] Gee, J. A.; Sholl, D. S. Effect of framework flexibility on C_8aromatic adsorption at high loadings in metal-organic frameworks. *The Journal of Physical Chemistry C* **2015**, *120*, 370–376.

4. TACHOMETRY

MOLECULAR ROTORS ARE ELUSIVE elements of a structure, especially in the case of fast dynamics. The high rotation rate, combined with their small size, make this value very difficult to obtain. Nowadays there are different ways to study molecular rotors and many of them are based on NMR. Those measurements are complex, time consuming and not always reliable, but are a fundamental tool in this small and fast world.

4.1 ANYSOTROPY STUDY

The surroundings of a nucleus modify the magnetic field experienced at the site of the nucleus according to:

$$\boldsymbol{B_i} = \bar{\sigma} \cdot \boldsymbol{B_0} \tag{4.1}$$

Both $\boldsymbol{B_i}$ and $\boldsymbol{B_0}$ are three-components vectors, related by the matrix:

$$\bar{\sigma} = \begin{pmatrix} \sigma_{xx} & \sigma_{xy} & \sigma_{xz} \\ \sigma_{yx} & \sigma_{yy} & \sigma_{yz} \\ \sigma_{zx} & \sigma_{zy} & \sigma_{zz} \end{pmatrix} \tag{4.2}$$

$\bar{\sigma}$ is usually symmetric. The vectorial nature of the external ($\boldsymbol{B_0}$) and induced ($\boldsymbol{B_i}$) magnetic fields, together with the shielding tensor $\boldsymbol{\sigma}$, can be ignored in the liquid state. In case of high isotropic motion average interactions and the equation 4.1 can be expressed in the scalar formula:

$$B_i = \sigma_{iso} * B_0 \tag{4.3}$$

where σ_{iso} is the isotropic value of the shielding tensor.

Solid state materials lack in the high degree molecular motion of liquids and the simplified formula cannot be used. In the equation 4.1, $\boldsymbol{B_i}$ and $\boldsymbol{B_0}$ are not necessarily parallel, except for three special orthogonal directions. These are the so-called principal axes and in this reference system $\bar{\sigma}$ become diagonal ($\sigma_{xy} = \sigma_{yx} = \sigma_{xz} = \sigma_{zxy} = \sigma_{yz} = \sigma_{zy} = 0$). The remaining three matrix components must be labeled so that $|\sigma_{zz}| \geq |\sigma_{yy}| \geq |\sigma_{xx}|$.[1,2]

TENSORS CONVENTIONS

The chemical shift tensors are able to univocally describe an anisotropic NMR lineshape of a powder sample. This does not mean that there is only one way to describe them and, over the years, various conventions have been established. Each is useful for highlighting some specific characteristics of the signal. For this reason, despite an official IUPAC standardization, some unofficial conventions are still in use.

IUPAC

The IUPAC convention derives directly from the diagonalized $\bar{\sigma}$, after the conversion from shielding to chemical shift. The generated tensors (δ_{11}, δ_{22}, δ_{33}) are labeled so $|\delta_{11}| \geq |\delta_{22}| \geq |\delta_{33}|$. Thus δ_{11} is the chemical shift of the least shielded orientation, while δ_{33} corresponds to the highest shielding (Fig. 4.1). The main advantage of this convention is the direct correlation between tensors and the signal main features but fails to describe the overall shape.[3]

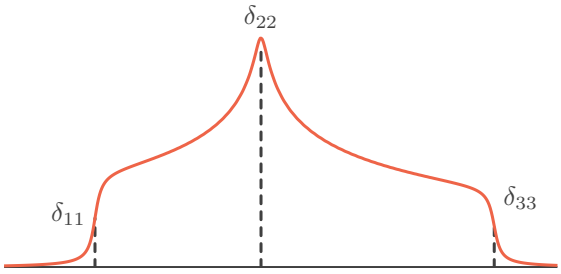

Figure 4.1: IUPAC tensor convention example.

Herzfeld-Berger

The main focus of Herzfeld's notation is on the internal proportions of the signal rather that on its position. The main component is the isotropic chemical shift value (δ_{iso}), which is an average of the IUPAC tensors. This parameter is directly connected to the σ_{iso} of equation 4.3. The second component is the span (Ω) that describe the maximum width of the powder pattern (Fig. 4.2). An anisotropic spectrum is called "axial" in the case $\delta_{22} = \delta_{11}$ or $\delta_{22} = \delta_{33}$; the third parameter of Herzfeld's notation (called skew, k) is useful for describing how axial the signal is. The skew value is between 1 ($\delta_{22} = \delta_{11}$) and -1 ($\delta_{22} = \delta_{33}$). If $k = 0$, the spectrum is symmetrical ($\delta_{22} = \delta_{iso}$).[4]

Herzfel-Berger / IUPAC

$$\begin{aligned} \delta_{iso} &= \frac{\delta_{11} + \delta_{22} + \delta_{33}}{3} \\ \Omega &\approx \delta_{11} - \delta_{33} \\ k &= 3\frac{\delta_{22} - \delta_{iso}}{\Omega} \end{aligned} \tag{4.4}$$

This notation immediately gives an idea of the size and shape of the NMR signal and facilitate the comparison between different spectra without considering the position.

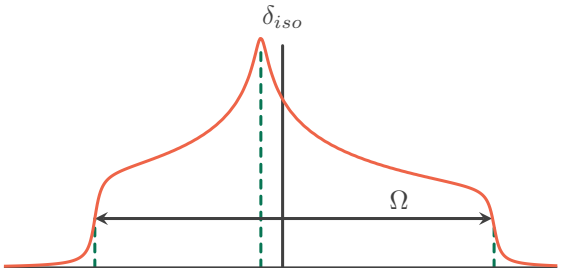

Figure 4.2: Herzfeld-Berger tensor convention example.

Haeberlen-Mehring-Spiess

The Haeberlen-Mehring-Spiess convention is the most non-IUPAC tensors definition used, the most of the NMR programs support or are entirely based on this convention (SIPSON, NMR-Weblab,...). It start defining three parameters (δ_{xx}, δ_{yy}, δ_{zz}) ordered accordingly to their separation from the isotropic value: $|\delta_{zz} - \delta_{iso}| \geq |\delta_{xx} - \delta_{iso}| \geq |\delta_{yy} - \delta_{iso}|$ (Fig. 4.3). It follows that, while $\delta_{22} = \delta_{yy}$, δ_{zz} can be δ_{11} or δ_{33} depending on the asymmetry direction. It is the same for δ_{xx}. Also in this case, the first parameter is the isotropic chemical shift (δ_{iso}) as calculated in formula 4.4. The second parameter is the asymmetry factor (η); although its value is related with the skew, it should not be confused. η is equal to 0 in the case of axial signal and is equal to 1 in the case of a symmetrical one. The anisotropy ($\Delta\delta$) indicates the distance between δ_{zz} and the centre of mass of the other two tensors. There is also a "reduced" anisotropy (δ) that indicates the distance between δ_{zz} and δ_{iso}.[5–7]

Haeberlen-Mehring-Spiess / IUPAC

$$\begin{aligned} \delta &= \delta_{zz} - \delta_{iso} \\ \Delta\delta &= \delta_{zz} - \frac{\delta_{xx} + \delta_{yy}}{2} = \frac{3}{2}\delta \\ \eta &= \frac{\delta_{yy} - \delta_{xx}}{\delta} \end{aligned} \tag{4.5}$$

The ambiguities of the convention, both in the tensors and in the anisotropies, hindered its immediate use. It is important to pay close attention while working with programs that use those parameters.

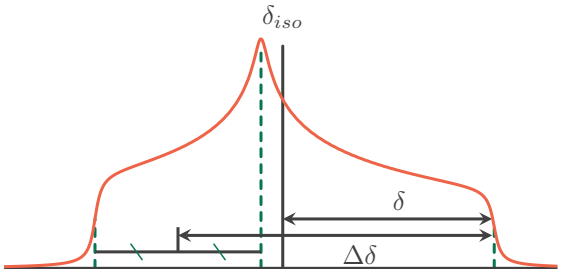

Figure 4.3: Haeberlen-Mehring-Spiess tensor convention example.

Motion Averaging

As mentioned before, the isotropic motion inside fluids, leads to a complete averaging of the tensors and the NMR measures a very narrow signal centered on δ_{iso}. Usually materials in the solid state are static, but there are cases of motion. In these situations, the tensors can be partially mediated and the resulting anisotropy is quite different from the starting one.

The explanation of how dynamics influence the lineshape is rather complicated and involves heavy mathematical analysis, fortunately there are two program able to perform the simulation: EXPRESS[9] and NMR Weblab.[10]. EXPRESS is a MatLab-base program that can handle very complex dynamics and allow a precise motion definition. Unfortunately it is not easy to obtain and is freely downloadable on some hidden sites. Another problem is the difficulty of using and exporting the simulation results. NMR Weblab is not advanced as EXPRESS but the entire calculation is performed on a free site console. Data can be downloaded in various formats. Despite being older than EXPRESS (2001 against 2009), it is continuously updated. I suggest always to start with NMR Weblab for any static analysis and, in case of complex situations, try EXPRESS if possible.

Three things are needed for simulations. First of all the static spectra tensors. This base set defines the unaveraged anisotropy that will be modified by the motion. The second parameter is the Euler angles and it is deeply analysed in the following part. The third parameter is the motion frequency of the movement.

It is important to emphasize that the motion does not change the tensors but only the signal. For this reason the anisotropy seems to change their parameters.

Euler Angles

The Euler angles are a series of parameters necessarily to describe the movement of the principal axis system (PAS) due to the motion. Despite this simple definition, they lack a uniform convention. As stated by Vold *"Few topics in NMR offer more opportunities for confusion than the conventions used to describe the rotations needed to describe tensor interactions in various coordinate systems"*.[9] Here only the definition of Rose[11] used by EXPRESS and (with some variation) by NMR Weblab will be discussed.

The Euler angles α, β and γ are defined starting from the PAS oriented so that z is the rotation axis of the movement. The first rotation is performed along z and is described by γ, then the second rotation by an angle β that is performed along the y-axis of the original PAS position. Finally the rotation by an angle α along the z-axis of the original PAS position. There is another definition; the first rotation is performed along z by α, the second rotation by an angle β along the new y-axis position and finally the rotation by γ along the new z-axis (Fig. 4.4). The two definitions are equivalent. The first is easier because it always refers to the original PAS system while the second refers to the modified reference system. EXPRESS requires the angles for each position and for this reason it allows the description of very complex, but rare, movements.

NMR Weblab uses another reference system: the cone frame, base on the variables α_0, θ and ϕ. With a small approximation, it is possible to say that α_0 is equivalent to γ and θ to β. For α and ϕ there is a big difference; while the first describes the angle of each position, the latter defines only the jump. For this reason the program is able to handle only rotations with β and γ constant, where the angular distribution of the minimum positions is uniform (with the exception for the 2-sites and 3-sites jumps).

Energy Calculation

One of the simulation parameter is the jump frequency k. Tensors and angles can be obtained from literature or calculations

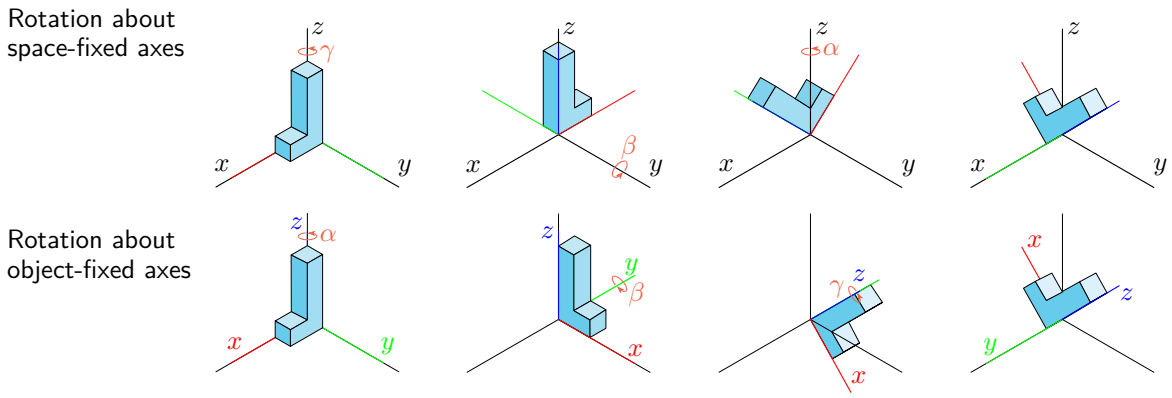

Figure 4.4: Euler angles as defined by Rose. In the example $\alpha = \pi/2$, $\beta = \pi/4$ and $\gamma = \pi$.[8]

so this parameter is usually the most interesting and important. If the acquisition is performed at variable temperatures, it is possible to measure the temperature dependence of the frequency. Motion in those systems generally follows the Arrhenius plot:

$$k(T) = k_0 e^{-E_A/RT} \tag{4.6}$$

k_0 represents the frequency of the motion at infinite temperature;
E_A is the activation energy;
R is the gas constant;
T is the temperature.
This makes it possible to measure the activation energy of the rotation process.

Experiment

The acquisition of an anisotropic NMR spectra is possible by an echo sequence. Due to the very large signals, the total experiment time can take a few hours or days. A complete analysis at variable temperature takes weeks.

Spin ½

Spectra acquisition of spin ½ nuclei is performed with the so-called Hahn echo sequence. Despite this is the most studied spin, the analysis of static spectrum is usually problematic. If the presence is abundant in nature (like ^{1}H), the strong dipole-dipole interactions deform the anisotropy[12,13] and fitting became difficult (if not impossible[14]). If the isotope is rare in nature (like ^{13}C) the signal is too weak to be acquired in reasonable time. This problem can be solved with the help of enriched nuclei.

Notably this technique is often used for gases inside porous materials; the channels hinder the isotropic motion and in particular conditions such molecules can undergo a unique pattern.[15–17]

Spin 1

Spectra acquisition is performed with a solid echo sequence. The most studied nucleus is deuterium (^{2}H) due to its low abundance, it is a perfect marker for the study of hydrogen components.[18–20] Due to its quadrupolar nature, the anisotropy is like two spin ½ signals mirrored long 0 Hz. Another peculiarity is that these spectra are represented in frequency instead of chemical shift. To simulate them, it is sufficient to define the asymmetry (η) and the coupling (δ_0) following the Haeberlen convention.

The main spectral feature is the distance between the two signal "horns". In a static spectrum the distance is equal to δ_0 (if $\eta = 0$ as in the case of deuterium) but, in case of motional averaging, it changes. A common situation is a deuterium bond with a carbon, in that case the quadrupolar splitting is given by:

$$\Delta\nu_q = \frac{3}{4}\frac{e^2qQ}{h}(3cos^2\theta - 1) \tag{4.7}$$

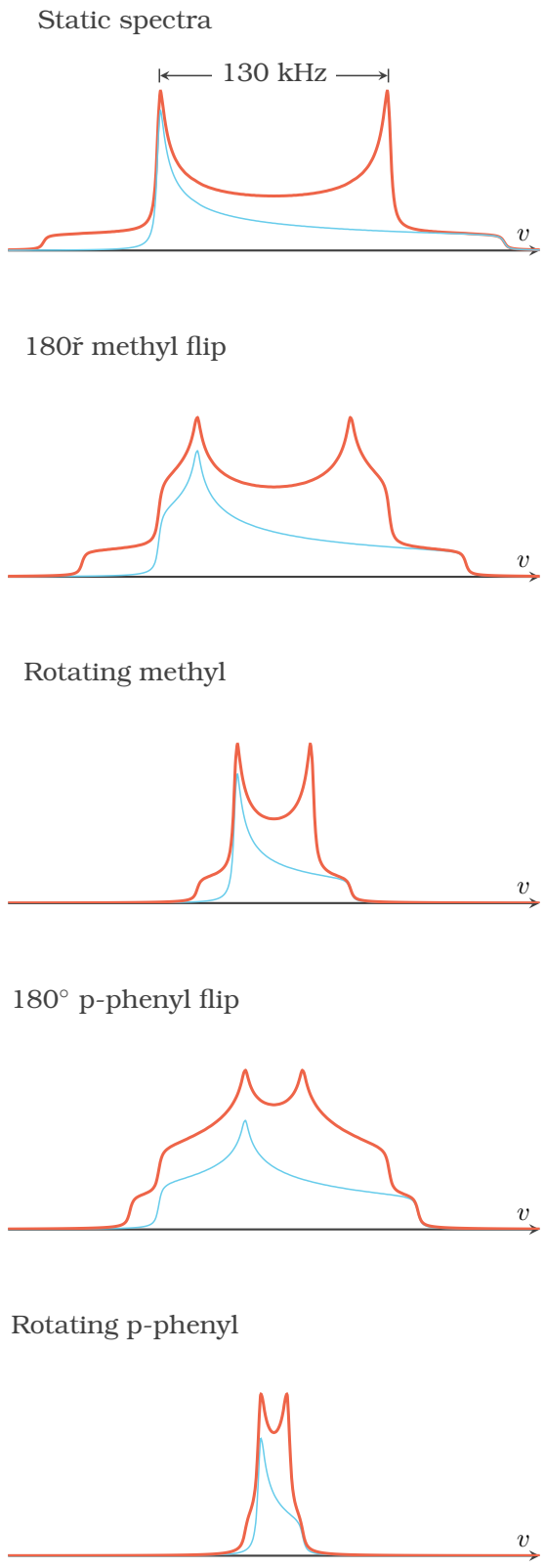

Figure 4.5: Examples of ^{2}H in C-D systems (**orange**) with different motions; is also present one of the two anisotropies that generate the signal (**light blue**).

e is the electron charge;

e^2qQ/h is the quadrupolar coupling constant;

θ is the angle between the C-D bond vector and the external magnetic field.

In the case of a powder sample or an amorphous material, the formula must be averaged over θ generating the aforementioned doubled mirror anisotropy. The distance between the singularities of the pattern (δ_0) is approximately 130 kHz. Focusing on a single anisotropy, it is possible to notice that $\delta_{11} = -\delta_0$ and $\delta_{22} = \delta_{33} = \delta_0/2$ ($\eta = 0$ and $\delta_{iso} = 0$ kHz). The rotation around an axis drastically changes the spectra (Fig. 4.5).[14] It is worth noting that the evolution from static spectra to fast rotation does not follow a gradual singularity shift; the signal of fast dynamics moieties rises from the static one.

Pros and Cons

Anisotropy analysis requires no advance instrument or complicate elaborations. It is a solid method, easily reproducible and give immediately insights about the system. This technique can be applied to the study of both molecular rotor and gases in a confined environments.

There are also some great limitations; first of all it is limited to a small range of frequencies. The anisotropy changes only between 10^3 Hz and 10^7 Hz,[14] in order to see any difference in very fast rotors it is necessary to go at very low temperature and for slow rotors dynamics to go at very high ones. Sometimes instrumental or material stability issues do not allow a wide range of temperature. Another problem is the isotopic labelling (not always necessarily, depending on the sample) which usually requires a dedicated synthesis. Finally, simulations are not extremely precise and the fitting evaluations are operator-dependent.

4.2 Second Moment

A static NMR experiment not always result in a neat anisotropy (or group of anisotropies). Often the interactions between spins average everything in a large broad signal, this is especially true for amorphous materials. Nevertheless, the spectrum still have some information about the sample.

For a resonance described by a normalized shape function $f(\omega)$ with a maximum in ω_0, the nth moment is defined as:

$$M_n = \int (\omega - \omega_0)^n f(\omega) d\omega \tag{4.8}$$

If $f(\omega)$ is symmetrical with respect to ω_0, as in most of the NMR signals, all the odd moments vanish.

The moments focus more on lineshape behaviour far from ω_0 and describe how it fall to zero. This is obviously correlated to the line width but also to the local magnetic field, not surprisingly the moments are expressed in G^n. Typically only the second and fourth moment are considered (rarely also the sixth) and for molecular motion the second moment is the most important.[1]

Measure

The moments cannot be measured directly but the value is obtained from the lineshape. Once defined a good shape function $f(\omega)$, it is sufficient to apply equation 4.8 to obtain the value. The most used function is the Gaussian curve:

$$f(\omega) = \frac{1}{\Delta\sqrt{2\pi}} \exp\left(\frac{-(\omega - \omega_0)^2}{2\Delta^2}\right) \tag{4.9}$$

It is easy to obtain that $M_2 = \Delta^2$ and $M_4 = 3\Delta^4$.

For a Gaussian curve, the full width at half maximum is:

$$FWHM = 2\Delta\sqrt{2\ln 2} \tag{4.10}$$

And it is possible to obtain directly the second moment with the formula:

$$M_2 = \frac{FWHM^2}{8\ln 2} \approx 0.18 * FWHM^2 \tag{4.11}$$

It is important to notice that the width must be measured in gauss.

In NMR also the Lorentzian curve is often used but the integral of equation 4.8 diverges so no moment can be defined.

Calculation

The moments were of great interest for solid-state NMR because they provide useful information about the spectra without dealing with the total Hamiltonian of the system. In fact the moments can be calculated from first principles only knowing the crystal structure.

Van Vleck

The formula used to calculate the second moment from the crystal structure has been described by Van Vleck[21] and is based on quantum mechanics interactions. Starting from a crystalline material made of some resonant spins I (the observed NMR nuclei) and non resonant spins S, the second moment is defined as:

$$M_{2(I)} = M_{2(II)} + \sum_S M_{2(IS)} \tag{4.12}$$

Now it is sufficient to calculate the second moment contribution of the homonuclear interactions (II) of the N_I resonant spins and the heteronuclear interaction (IS) between the resonant and the N_S non resonant spins.

$$M_{2(II)} = \frac{1}{N_I}\frac{3}{4}\left(\frac{\mu_0}{4\pi}\right)^2 \gamma_I^2 \hbar^2 I(I+1) \sum_{i=1}^{N_I}\sum_{j=1}^{N_I} B_{ij}^2 \tag{4.13}$$

$$B_{ij} = \frac{3\cos^2\Theta_{ij} - 1}{r_{ij}^3} \tag{4.14}$$

$$M_{2(IS)} = \frac{1}{N_S}\frac{1}{3}\left(\frac{\mu_0}{4\pi}\right)^2 \gamma_S^2 \hbar^2 S(S+1) \sum_{i=1}^{N_I}\sum_{k=1}^{N_S} B_{ik}^2 \tag{4.15}$$

$$B_{ik} = \frac{3\cos^2\Theta_{ik} - 1}{r_{ik}^3} \tag{4.16}$$

γ is the gyromagnetic ratio of the nucleous;

r is the atomic distance;

Θ is the angle between r and the external magnetic field.

The only real challenge is the enormous number of correlations present even in the simplest structure. Due to the dependence on r^{-3} it is sufficient to consider the interaction between a reference cell and the first neighbors (or more if the cell is small). The resulting second moment is valid for a single crystal, in case of powder sample the calculation must be averaged with respect to all possible spatial orientations.[22]

$$M_2^{powder} = \frac{1}{4\pi}\int_0^{2\pi}\int_0^{\pi} M_2 \sin\theta d\theta d\phi \qquad (4.17)$$

It has been demonstrated that it is not necessary to solve the integrals but is possible to use just some θ and ϕ values to obtain a good spatial averaging.[23]

Motion Averaging

The second moment is constant but at low temperature the static NMR signal is broader. The two statements seem contradictory and the answer is in the NMR measurement itself. The spectrum is an adsorption signal and is regulated by the system Hamiltonian. Any motion perturbs this component and can lead to a loss of the regions far from ω_0 and the signal appears close to a Lorentzian curve. Thus, even if the second moment is unaffected by the motion, its observable part become smaller.[1]

In the case of fast motion, the intramolecule (or intrarotor) contribution at the second moment is always reduced to $^1/_4$.[24] The intermolecule (or interotor) part is affected in more complex ways. Goc[25] proposes a useful program to calculate the second moment as function of the motion. The program itself is very efficient but not really easy to use and the FORTRAN language it uses is outdated. For this reason, many groups rewrite it in other languages, sometimes adding specific features (see my C++ version).

A big problem remains: the program works in jump per simulation and the conversion to temperature must be performed separately. The number of jumps n is correlated to the correlation time τ_C by the formula:

$$\tau_C = \frac{2\pi N_{axis}}{n\delta\upsilon_{1/2}} \qquad (4.18)$$

N_{axis} is the number of axis in the simulation;

$\delta\upsilon_{1/2}$ is the NMR line width of the static structure.

It is sufficient to apply the Arrhenius equation 4.6 to obtain the temperature.[26]

Usually the second moment changes very quickly from the static value to the fast limit. The transition is always present when $\tau_C^{-1} = \gamma\sqrt{M_2}$.

This variation with the motion is historically very important because it led, in 1959, to the invention of the magic angle spinning technique.[27,28]

Pros and Cons

The second moment is an easy way to obtain proof of a dynamics within the material but is incredibly limited. The transition between fast and static spectra is complete in a few degrees and it is difficult to map precisely. Even in case of success, the spectra need a great elaboration to extrapolate the data and everything must be supported by simulations (which are possible only in case of crystal materials). However, in some cases, it is possible to perform a complete analysis of the dynamics and also obtain an estimation of the activation energy.

4.3 Relaxation Times

During an NMR experiment, the magnetization evolves from a perturbed state towards equilibrium.[29] This occurs in two specific way: the exchange of energy with the lattice and the spin-spin coupling. The first mechanism is defined by the constant T_1 also known as spin-lattice

relaxation time;[30] it can occur by a single-phonon process in which the energy released matches the lattice mode energy. The latter is defined by the constant T_2 and is the coherence time between spins.[31]

The direct correlation between T_1 and the crystal dynamics allows this value to be used to study molecular rotors. The main theory describing relaxation was published by Bloembergen, Purcell and Pound in 1948[32] and is known as the BPP theory. The model was then completely formulated by Kubo and Tomita in 1954.[33]

Measure

There are different pulse sequences to measure the spin-lattice relaxation times and the choice depends on the material and instrumentation. Each one start with a hypothesis of the possible T_1 value, so it is often necessary to repeat the analysis especially in the case of new systems.

Inversion Recovery

The Inversion Recovery (IR or InvRec) method is the simplest technique used to measure the spin-lattice relaxation times. An initial pulse rotates the longitudinal magnetization (M_z) by 180°. The system is then allowed to evolve for a period τ. During this time the z component of the magnetization tends to returns to its equilibrium value M_0, at rate dependent of T_1. The final 90° pulse rotate the partially recovered magnetization in the xy plane, allowing the sampling of M_z (Fig. 4.6).[34,35] The magnetization is directly correlated to the signal intensity; following the formula:

Inversion Recovery

$$I(\tau) = I_0(1 - 2Ae^{-\tau/T_1}) \qquad (4.19)$$

I_0 is the signal intensity for $\tau \geq 5T_1$;

A is a correction parameter for the not perfect inversion ($M_z(0) \neq -M_0$).[36]

The relaxation formula is based on the assumption that the spin system is in its equilibrium state before the inversion

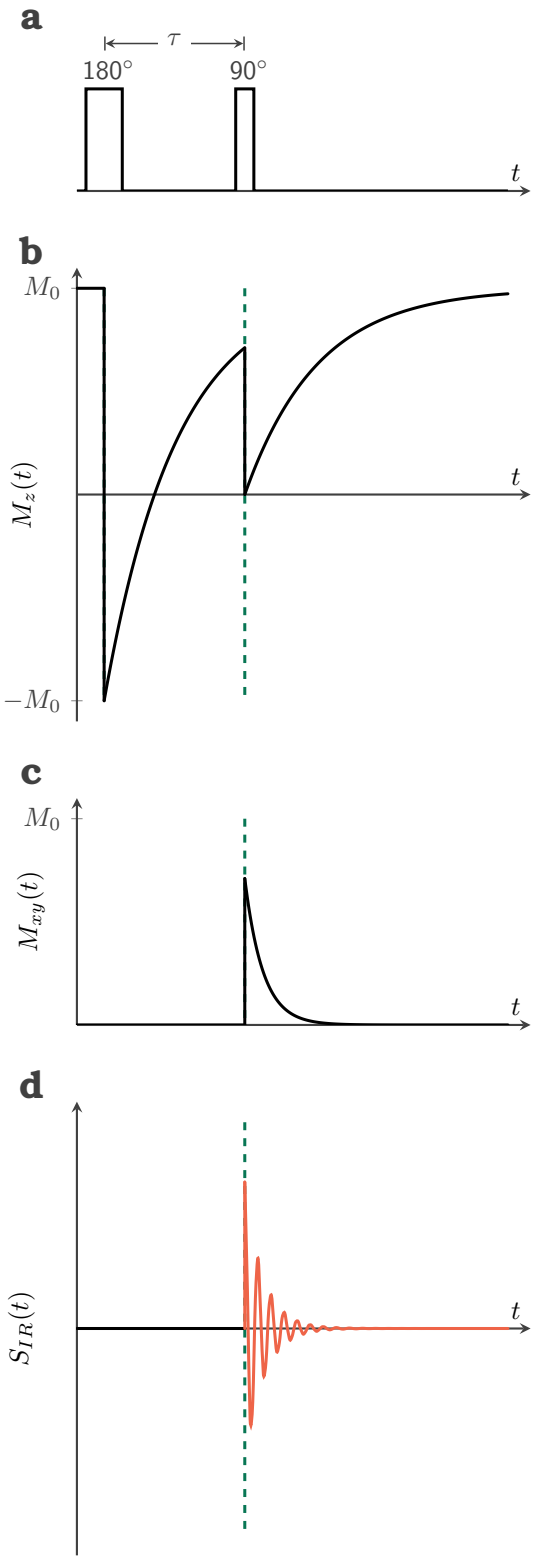

Figure 4.6: Inversion recovery sequence. **a** Pulse scheme. **b** Temporal evolution of the longitudinal magnetization. **c** Temporal evolution of the transverse magnetization. **d** Induced MR signal.[34]

pulse. An appropriate interval between measurements is commonly $5T_1$; during this time the magnetization reaches 99.3% of its equilibrium value.[14] This factor has a great influence on the experiment duration and becomes impractical for the measurement of long relaxation times.

Saturation Recovery

The Saturation Recovery (SR or SatRec) method is the most common technique used to evaluate T_1. The main advantage that has made SR so popular is that it does not need the complete magnetization recovery, accelerating the experiments.

An initial 90° pulse rotates the magnetization (M_z) in the xy plane in which the signal is acquired and allowed to evolve for a time τ. Then 90° pulses continue to rotate the reduced longitudinal magnetization in the xy plane for the acquisition (Fig. 4.7).[34] The relaxation time is then calculated with the formula:

Saturation Recovery

$$I(\tau) = I_0(1 - e^{-\tau/T_1}) \tag{4.20}$$

I_0 is the signal intensity at equilibrium.

Saturation Recovery, and a similar method called Progressive Saturation, are excellent in speeding up measurements because it is sufficient to wait for the recovery of the transverse magnetization (M_{xy}) between pulses. This component evolves with T_2 and in the solid state it is strictly less than spin lattice times ($T_2 \ll T_1$). However, these pulses cause a mixing effect that reduces the accuracy of the measurement.[37]

Torchia Sequence

Measuring the relaxation times of carbon in the solid state is quite difficult. There are two main problems: the low signal (due to the low natural abundance of the isotope ^{13}C) and the very long T_1 (from some seconds to minutes). Under these conditions, even the saturation recovery

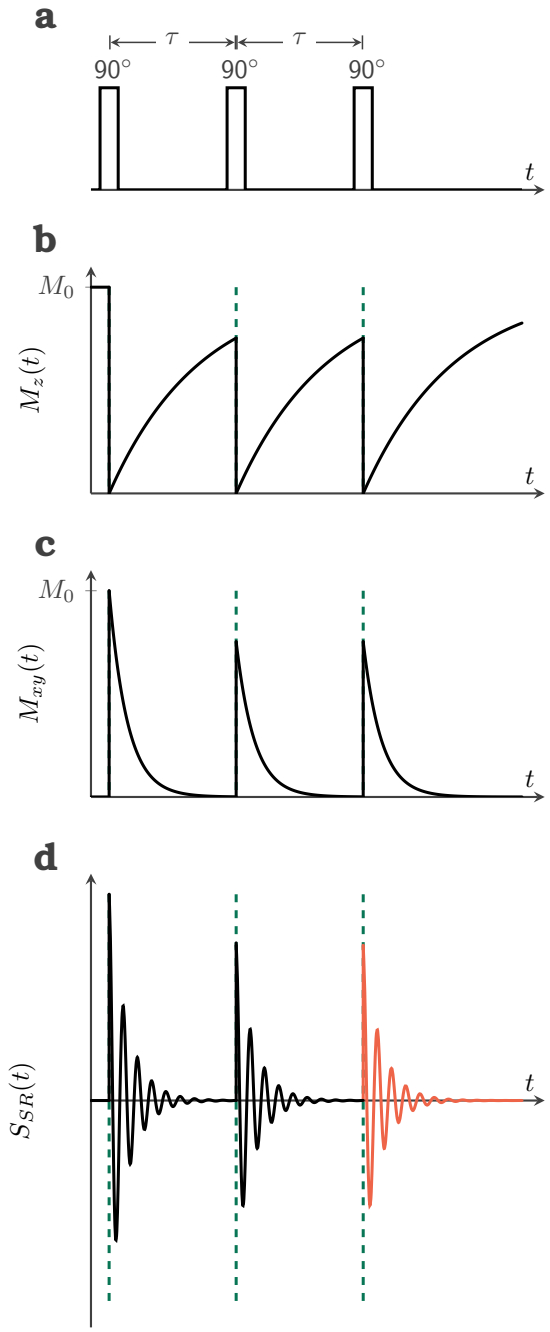

Figure 4.7: Saturation recovery sequence. **a** Pulse scheme. **b** Temporal evolution of the longitudinal magnetization. **c** Temporal evolution of the transverse magnetization. **d** Induced MR signal.[34]

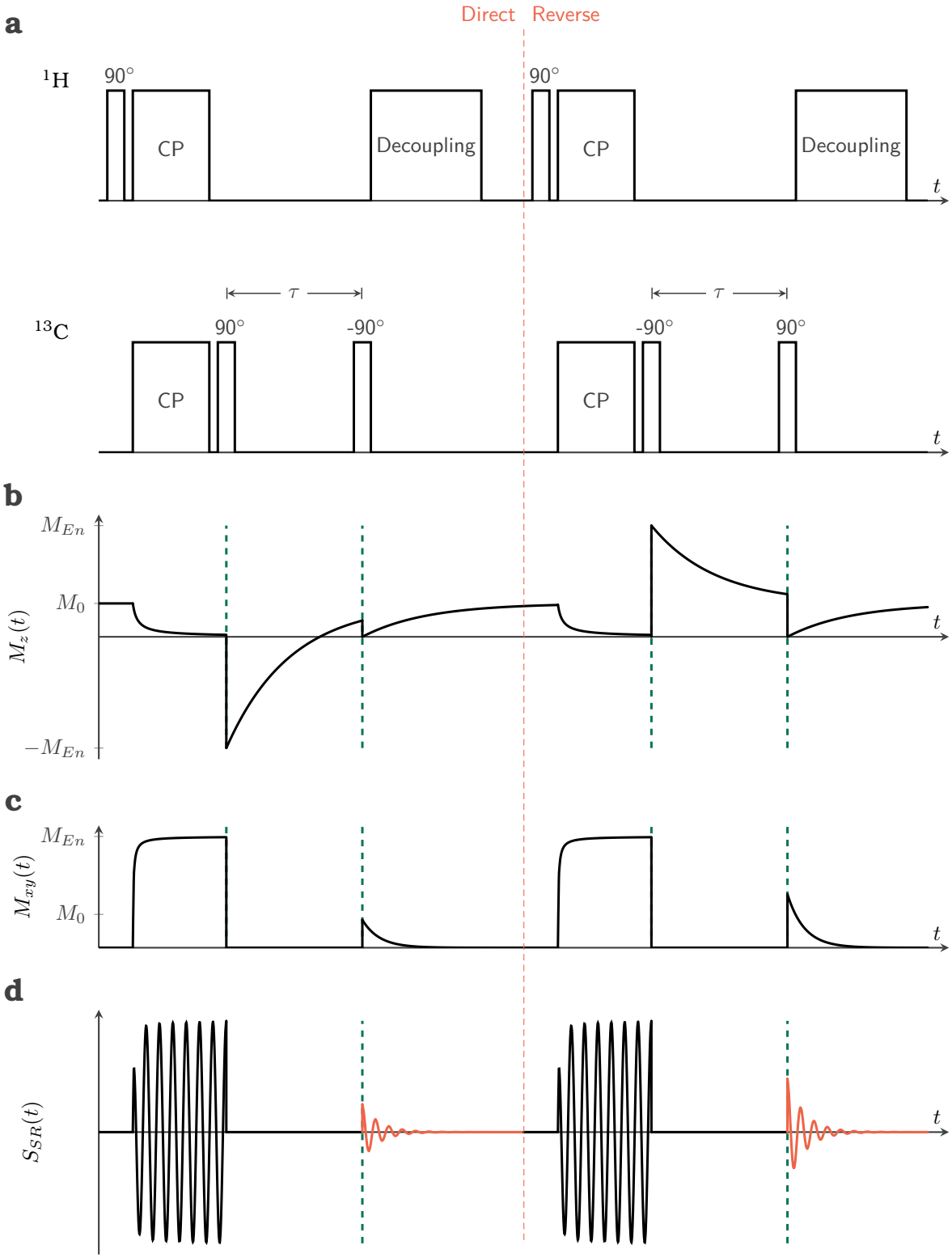

Figure 4.8: Torchia sequence. **a** Pulse scheme. **b** Temporal evolution of the longitudinal magnetization of ^{13}C. **c** Temporal evolution of the transverse magnetization of ^{13}C. **d** Induced MR signal.

offers only a little help.

A common method to enhance the carbon signal is the cross-polarization (CP). It also has the advantage of speeding up the measurement because it is sufficient to wait for the relaxation of hydrogen atoms before repeating the sequence.[38,39]

This technique solves the main problems but rises another one. A CP signal starts with a negative enhance magnetization ($-I_{En}$) which evolves towards the equilibrium (I_0) while a normal sequence starts from the negative equilibrium value ($-I_0$). Applying this correction to equation 4.19 for an InvRec sequence:

$$I(\tau) = I_0 - (I_0 + I_{En})e^{-\tau/T_1} \qquad (4.21)$$

The enhanced magnetization I_{En} is quite easy and fast to measure, but the equilibrium magnetization must be acquired without any CP. This experiment is a great improvement over InvRec, but the measurement of I_0 remains a considerable investment of time.

The solution came in 1978 from Dennis Torchia. He suggested performing also a "reverse" CP inversion recovery, aligning the magnetization with $+z$ instead of $-z$.(Fig. 4.8) In this case the signal intensity follows the formula:

$$I(\tau) = I_0 - (I_0 - I_{En})e^{-\tau/T_1} \qquad (4.22)$$

Now, subtracting equation 4.21 from equation 4.22:

Torchia

$$I(\tau) = 2I_{En}e^{-\tau/T_1} \qquad (4.23)$$

This calculation gets rid of I_0, accelerating the experiment (Fig. **??**).[40]

The formula is easy to implement thanks to the linearity of Fourier transform: the instrument first performs the "direct" acquisition changing the FID sign, then it performs the "reverse" sequence.

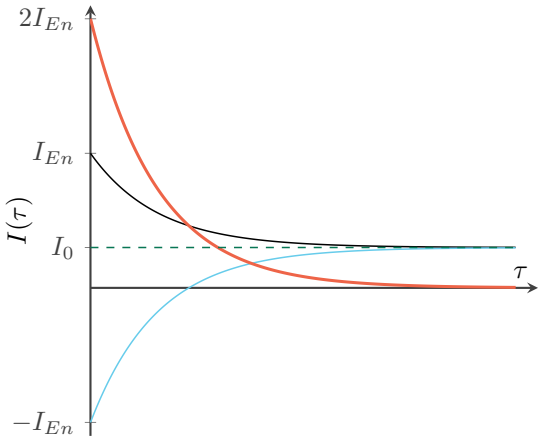

Figure 4.9: Torchia intensity plot (orange), "direct" CP InvRec (light blue) and "reverse" CP InvRec (**black**).

Sometimes the system has carbons that relax faster than hydrogens (T_1 ^{13}C $< T_1$ ^{1}H). This situation can generate a transient nuclear Overhauser effect (NOE), altering the result. In these cases, saturating the ^{1}H channel with a train of 90° pulses has been shown to reduce the effect.[41–43]

Energy Calculation

The relaxation times are related to the correlation time by the Kubo-Tomita equation.[33] Technically there are two formulas: depending on the relaxation process is necessarily to use the homonuclear or the heteronuclear version. Both use the spectral density function ($j(\omega)$) defined as:

Spectral Density Function

$$j(\omega) = \frac{\tau_C}{1 + \omega^2\tau_C^2} \qquad (4.24)$$

τ_C is the period of the motion;
ω is the angular Larmor frequency ($2\pi\upsilon_L$).

The period τ_C, for a thermally activated motion, is regulated by the Arrhenius formula:

$$\tau_C(T) = \tau_0 e^{E_A/RT} \qquad (4.25)$$

τ_0 represents the period of the motion at infinite temperature;

E_A is the activation energy;
R is the gas constant;
T is the temperature.

The Kubo-Tomita equations are linear combination of spectral density functions. As a starting point, let us suppose:

$$\frac{1}{T_1} = j(\omega) \tag{4.26}$$

Equation 4.24 describes a function (Fig. 4.10) with an absolute maximum at:

$$\begin{aligned} \tau_C &= \frac{1}{\omega} \\ T_1 &= 2\omega \\ T &= -\frac{E_A}{R\ln(\omega\tau_C)} \end{aligned} \tag{4.27}$$

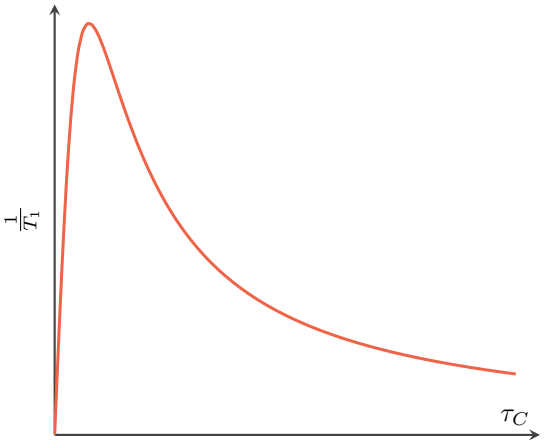

Figure 4.10: Spectral density function plot.

The function integral is:

$$\int \frac{\tau_C}{1+\omega^2\tau_C^2} d\tau_C = \frac{\ln(1+\omega^2\tau_C^2)}{2\omega^2} \tag{4.28}$$

The defined integral between zero and infinite is divergent, but is important to notice that the value is strongly dependent on ω^{-2}.

Homonuclear Kubo-Tomita

This formula is commonly applied to proton relaxation experiments. In these systems ^{1}H is the most abundant (and sometimes the only) spin-½NMR active isotope. When the protons are excited, they can only relax through homonuclear correlations:[14]

Homonuclear Kubo-Tomita Equation

$$\frac{1}{T_1} = C[j(\omega) + 4j(2\omega)] \tag{4.29}$$

C is the relaxation constant.

The formula, is composed by two spectral density function: one for ω and one for 2ω (Fig. 4.11).

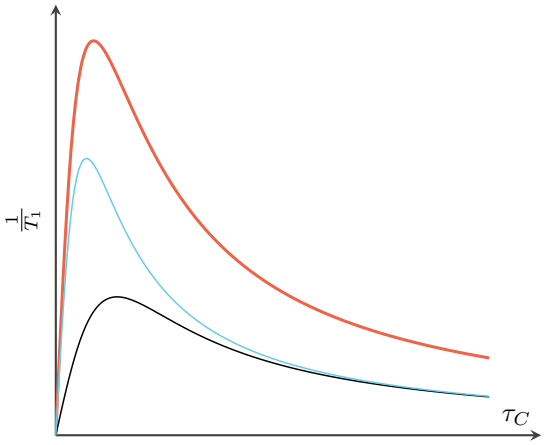

Figure 4.11: Homonuclear Kubo-Tomita assuming $C = 1$ (**orange**), $j(\omega)$ (**black**) and $4j(2\omega)$ (**light blue**).

The two components have a similar importance to defining the final shape because the "reduced area" of $j(2\omega)$ (see Equation 4.28) is compensated with the multiplication by 4. The formula is easy to derive and have an absolute maximum:

$$\begin{aligned} \tau_C &\approx \frac{0.61579}{\omega} \\ T_1 &\approx \frac{\omega}{1.4252C} \\ T &\approx -\frac{E_A}{R\ln(\frac{\omega\tau_0}{0.61579})} \end{aligned} \tag{4.30}$$

If the system is far from the maximum, it is possible to use a simplified equation:

$$\text{For } \omega\tau_C \ll 1 \rightarrow \tfrac{1}{T_1} = 5C\tau_C$$

$$\ln T_1 = -\frac{E_A}{R}\frac{1}{T} + \ln\frac{1}{5C\tau_0} \tag{4.31}$$

$$\text{For } \omega\tau_C \gg 1 \rightarrow \tfrac{1}{T_1} = \tfrac{2C}{\tau_C\omega^2}$$

$$\ln T_1 = \frac{E_A}{R}\frac{1}{T} + \ln\frac{\tau_0\omega^2}{2C} \tag{4.32}$$

It is important to notice that any fitting in these ranges cannot distinguish between C and τ_0, even without the use of the simplified formulas.

Heteronuclear Kubo-Tomita

Often, NMR studies refer to rare isotopes inside complex structures. In these samples the nuclei have some difficulties to couple with themselves and tend to interact with other NMR active elements. A common example is carbon (^{13}C with natural abundance of 1.1%) relaxing with hydrogens. In this case the relaxation is regulated by the formula:

Heteronuclear Kubo-Tomita Equation

$$\frac{1}{T_1} = C[j(\omega_2 - \omega_1) + 3j(\omega_1) + 6j(\omega_2 + \omega_1)] \tag{4.33}$$

ω_1 is the angular Larmor frequency of observed isotope;

ω_2 is the angular Larmor frequency of the other isotope;

C is the relaxation constant.

Considering the relaxation of ^{13}C with ^{1}H, the final result is shown in figure 4.12. It is important to remember that ω_{1_H} is about four times larger than ω_{13_C}. For this reason, the contribution of $j(\omega_2 - \omega_1)$ and $j(\omega_2 + \omega_1)$ are incredibly small (see Equation 4.28) and the final shape is mainly due to $j(\omega_1)$.

In the case of very similar frequencies, the factor $j(\omega_2 - \omega_1)$ becomes predominant and in the limit case $\omega_2 = \omega_1$ we obtain the homonuclear equation.[14]

The formula is quite complex and is not easy to find the maximum. Even limits are difficult to define because $\omega\tau_C$ is different for each spectral density.

$$\text{For } \omega\tau_C \ll 1 \rightarrow \tfrac{1}{T_1} = 10C\tau_C$$

$$\ln T_1 = -\frac{E_A}{R}\frac{1}{T} + \ln\frac{1}{10C\tau_0} \tag{4.34}$$

As for the homonuclear formula, far from the maximum, C and τ_0 became impossible to distinguish.

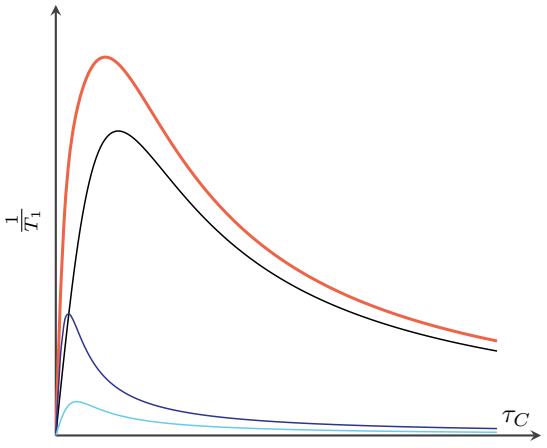

Figure 4.12: ^{13}C-^{1}H Heteronuclear Kubo-Tomita assuming $C = 1$ (**orange**), $j(\omega_2 - \omega_1)$ (**light blue**), $3j(\omega_1)$ (**black**) and $6j(\omega_2 + \omega_1)$ (**blue**).

Theoretical Values

The Kubo-Tomita equations have three main fitting parameter: C, τ_0 and E_A. During the fitting, there is an assumption of the mechanism that regulates the relaxation but it can be only a minimum part or completely different. It is important to compare the results with theoretical values: $\tilde{C}$ and $\tilde{\tau}_0$.

It is possible to define the ratios $C/\tilde{C}$ and $\tau_0/\tilde{\tau}_0$. They must be as close as possible to unity and are a good indicator of the fitting validity also taking into account the motion model.[44]

Maximum Frequency

The maximum frequency ($\tilde{\tau}_0^{-1}$) for a rotating molecule (or part of it) depends only on the rotation energy barrier and the moment of inertia.

The moment of inertia is defined as:

Moment of Inertia

$$I = \sum_i m_i r_i^2 \tag{4.35}$$

m_i is the atomic mass of the ith atom;

r_i is the distance from the rotation axis of the ith atom.

Sometimes only a small part of the

molecule rotates and the reduced moment of inertia is defined:

$$I_r = I_\alpha \left(1 - \sum_i \lambda_i^2 \frac{I_\alpha}{I_i}\right) \tag{4.36}$$

I_α is the moment of inertia of the rotating part;

I_i is the moment of inertia along the ith principal axis;

λ_i is the directional cosine of the angle between the rotational axis and the ith principal axis.

The principal axis are defined as the coordinate system that diagonalized the symmetrical matrix:[45]

$$\bar{I} = \begin{bmatrix} I_{xx} & I_{yx} & I_{zx} \\ I_{xy} & I_{yy} & I_{zy} \\ I_{xz} & I_{yz} & I_{zz} \end{bmatrix} \tag{4.37}$$

with:

$$\begin{aligned} I_{xx} &= \sum_i m_i(y_i^2 + z_i^2) \\ I_{yy} &= \sum_i m_i(z_i^2 + x_i^2) \\ I_{zz} &= \sum_i m_i(x_i^2 + y_i^2) \\ I_{xy} = I_{yx} &= \sum_i m_i x_i y_i \\ I_{yz} = I_{zy} &= \sum_i m_i y_i z_i \\ I_{zx} = I_{xz} &= \sum_i m_i x_i z_i \end{aligned} \tag{4.38}$$

x_i, y_i and z_i are the components along the axis of r_i.

Once the inertia of a rotating molecule (or part of it) is defined, it is possible to focus on the energies involved in the rotation. Considering a simple case of N equal minima distributed uniformly, the potential can be described as:

$$V(\alpha) = V_{Max} \sin^2 \frac{N\alpha}{2} \tag{4.39}$$

α is the angle variable;

V_{Max} is the energy barrier.

The entire system can be described with the equation:

$$-\frac{\hbar^2}{2I_r}\frac{d^2\psi(\alpha)}{d\alpha^2} = \left(E - V_{Max}\sin^2\frac{N\alpha}{2}\right)\psi(\alpha) \tag{4.40}$$

In the case $V_{Max} \to 0$ the potential part becomes negligible and the formula cannot be used to calculate the maximum frequency. But in the case where V_{Max} is sufficiently big, it is possible to use the parallelism between the previous formula and the harmonic oscillator of angular frequency ω.[46]

$$-\frac{\hbar^2}{2m}\frac{d^2\psi(x)}{dx^2} = \left(E - \frac{1}{2}m\omega^2 x^2\right)\psi(x) \tag{4.41}$$

Assuming low rotation amplitude, equation 4.39 can be simplified:

$$V(\alpha) = V_{Max}\left(\frac{N\alpha}{2}\right)^2 \tag{4.42}$$

Combining 4.40, 4.41 and 4.42

$$\omega = N\sqrt{\frac{V_{Max}}{2I_r}} \tag{4.43}$$

Assuming $V_{Max} \approx E_A$:

Maximum Theoretical Frequency

$$\tilde{\tau}_0^{-1} = \omega = N\sqrt{\frac{E_A}{2I_r}} \tag{4.44}$$

Relaxation Constant

The relaxation constant describes the polar interactions involved in the relaxation process.[47] In the case with a large number of nuclei very close to each other, the value is big and the relaxation times are relatively short. The formula for a rotating methyl group is:

$$\tilde{C} = c\frac{n}{N}\frac{9}{40}\left(\frac{\mu_0}{4\pi}\right)^2\frac{\gamma^4\hbar^2}{r^6} \tag{4.45}$$

n is the number of the nuclei whose dipole-dipole interaction are being modulated (are part of the rotor);

N is the total number of nuclei;

μ_0 is the permeability of free space ($\mu_0/4\pi = 10^{-7}\, m\, Kg\, s^{-2}\, A^{-2}$);

γ is the gyromagnetic ratio of the element;
$\hbar$ is the reduced Plank constant;
r is the internuclei distance.
$^9/_{40}$ is valid only for methyl groups and contains information about the rotor geometry. It is a product of three factors:

- $^3/_{20}$ from the relaxation theory.
- $^3/_4$ is due to the isotropic movement inside the plane $(^3/_4(\sin a)^4 + (\sin 2a)^2)$ with a the angle between r and the rotation axis.
- 2 is the number of spin-spin interactions.

c needs a more detailed explanation. Equation 4.45 supposes a pure intramethyl relaxation and in this case $c=1$. The intrarotor dipole interactions are preferential but not exclusive and in some systems also the coupling between rotor and structure nuclei must be taken into account. In these cases $c > 1$.[48] Unfortunately, the equation can be applied only to the specific case of hydrogens in methyl groups.

It is possible to notice some similarities between equation 4.45 and the Van Vleck formulas (equations 4.13, 4.14, 4.15,4.16). In principle both the second moment and the relaxation constant describe the dipolar interactions of nuclei so it is obvious that the formulas are similar.[49] As described in a previous section, it is possible to calculate the second moment directly from the crystal structure (or from the static spectra).

Assuming a system of two equivalent and periodic potential wells, the value of the second moment is described by the formula:[50]

$$M_2 = M_2^{stat} - \frac{3}{2}\frac{1}{\gamma^2}C + \frac{3}{2}\frac{1}{\gamma^2}C\frac{2}{\pi}\arctan(\gamma\sqrt{M_2}\tau_C) \tag{4.46}$$

As explained early, the second moment varies from the value in absence of motion (M_2^{stat}) to the fast limit (M_2^{fast}). The latter is defined as the second moment when $\tau_C^{-1} \ll \gamma\sqrt{M_2}$;[51] so the previous formula become:

$$M_2^{fast} = M_2^{stat} - \frac{3}{2}\frac{1}{\gamma^2}C \tag{4.47}$$

Theoretical Relaxation Constant

$$\tilde{C} = \frac{2}{3}\gamma^2\Delta M_2 \tag{4.48}$$

$\Delta M_2 = M_2^{stat} - M_2^{fast}$.

The main advantage of this formula is its incredible flexibility. While the equation 4.45 can only be applied to hydrogens in methyl groups, this can be used for any nucleus in any system with regular rotation. Another important feature is that the second moment values can be obtained both from the experiments and from *ab initio* calculations.

Spin-Spin Relaxation

Also the T_2 are altered by the motion and formulas are quite similar to T_1.[1,52] The main problem with spin-spin relaxation is its sensitivity and even the smallest difference can drastically change the results. This generates many reproducibility problems and the molecular rotors are mainly studied with more stable spin-lattice relaxation.

Homonuclear T_2 Relaxation

$$\frac{1}{T_2} = \frac{C}{2}[3j(0) + 5j(\omega) + 2j(2\omega)] \tag{4.49}$$

Heteronuclear T_2 Relaxation

$$\frac{1}{T_2} = \frac{C}{2}[4j(0) + 6j(\omega_2) + j(\omega_2 - \omega_1) + 3j(\omega_1) + 6j(\omega_2 + \omega_1)] \tag{4.50}$$

Quadrupolar Nuclei

All the nuclei with spin $I \geq 1$ are quadrupolar. These atoms interact with the molecular electric field gradients (EFG) and this is the main relaxation mechanism. Assuming a very fast motion in the liquid state able to erase that interaction, the relaxation formulas are defined as:[14]

$$\frac{1}{T_1} = \frac{1}{T_2} = \frac{3\pi^2}{10}\frac{2I+3}{I^2(2I-1)}\left(1+\frac{\eta^2}{3}\right)\chi^2\tau_C \quad (4.51)$$

η is the symmetry parameter;

$\chi = e^2qQ/h$ is the quadrupolar coupling constant.

In the special case of $I = 1$ is possible rewrite equations 4.29 and 4.49 as:[1]

$$\frac{1}{T_1} = \frac{3\pi^2}{10}\left(1+\frac{\eta^2}{3}\right)\chi^2[j(\omega)+4j(2\omega)] \quad (4.52)$$

$$\frac{1}{T_2} = \frac{3\pi^2}{20}\left(1+\frac{\eta^2}{3}\right)\chi^2[3j(0)+5j(\omega)+2j(2\omega)] \quad (4.53)$$

Pros and Cons

T_1 analysis is an incredibly powerful technique. The main advantages are the relatively fast measures, the precision of the results and the absence of limits due to the motion. This technique is able to analyze fast or slow rotor without problems. Furthermore it does not need any type of element labelling, so the synthesis can be kept simple.

There are some drawbacks. First of all the data need a lot of elaboration; intensities must be fitted with specific equations to extrapolate the T_1 and these data must be fitted with appropriate formula. This can introduce some errors if the procedure is performed without due attention.

But the main problem is in the relaxation mechanism itself. Relaxometry is a common technique used to characterize pore size and shapes in porous materials using the relaxation times of adsorbed fluids.[53,54] The problem is that also the relaxation time of the structure is modified by the adsorbate. Some species in the air (like O_2 and H_2O) can speed up the relaxation rate and these altered results cannot be used. The only way to overcome the problem is to study the material under vacuum, performing the NMR experiment on glass sealed vials or close the MAS rotor with a CAVERN[55] apparatus. It is possible to study the dynamics of molecular rotors in the presence of gases or volatile guests by loading the material and guest in sealed vials.

Bibliography

[1] Abragam, A. *The Principles of Nuclear Magnetism*; International series of monographs on physics; Clarendon Press, 1961.

[2] Harris, R.; Wasylishen, R.; Duer, M. *NMR Crystallography*; eMagRes Books; Wiley, 2012.

[3] Mason, J. Conventions for the reporting of nuclear magnetic shielding (or shift) tensors suggested by participants in the NATO ARW on NMR shielding constants at the University of Maryland, College Park, July 1992. *Solid State Nuclear Magnetic Resonance* **1993**, *2*, 285–288.

[4] Herzfeld, J.; Berger, A. E. Sideband intensities in NMR spectra of samples spinning at the magic angle. *The Journal of Chemical Physics* **1980**, *73*, 6021–6030.

[5] Haeberlen, U. *High Resolution NMR in Solids Selective Averaging: Supplement 1*; Advances in magnetic resonance. Supplement 1; Academic Press, 1976.

[6] Mehring, M. *Principles of High Resolution NMR in Solids*; Springer Verlag, 1983.

[7] Spiess, H. W. *NMR Basic Principles and Progress. Vol.15*; Springer Verlag, 1978.

[8] Young, R. P.; Lewis, C. R.; Yang, C.; Wang, L.; Harper, J. K.; Mueller, L. J. TensorView: a software tool for displaying NMR tensors. *Magnetic Resonance in Chemistry* **2018**, *57*, 211–223.

[9] Vold, R. L.; Hoatson, G. L. Effects of jump dynamics on solid state nuclear magnetic resonance line shapes and spin relaxation times. *Journal of Magnetic Resonance* **2009**, *198*, 57–72.

[10] Macho, V.; Brombacher, L.; Spiess, H. W. The NMR-WEBLAB: an internet approach to NMR lineshape analysis. *Applied Magnetic Resonance* **2001**, *20*, 405–432.

[11] Rose, M. *Elementary Theory of Angular Momentum*; Structure of Matter Series; New York, 1957.

[12] Pake, G. E. Nuclear resonance absorption in hydrated crystals: fine structure of the proton line. *The Journal of Chemical Physics* **1948**, *16*, 327–336.

[13] Blümich, B.; Blümler, P.; Chmelka, B.; Fleischer, G.; Fujara, F.; Grimmer, A.; Laupretre, F.; Raftery, D. *Solid-State NMR I Methods: Methods*; NMR Basic Principles and Progress; Springer Berlin Heidelberg, 2012.

[14] Bovey, F.; Mirau, P.; Gutowsky, H. *Nuclear Magnetic Resonance Spectroscopy*; Elsevier Science, 1988.

[15] Kong, X.; Scott, E.; Ding, W.; Mason, J. A.; Long, J. R.; Reimer, J. A. CO_2 dynamics in a metal–organic framework with open metal sites. *Journal of the American Chemical Society* **2012**, *134*, 14341–14344.

[16] Bassanetti, I.; Bracco, S.; Comotti, A.; Negroni, M.; Bezuidenhout, C.; Canossa, S.; Mazzeo, P. P.; Marchió, L.; Sozzani, P. Flexible porous molecular materials responsive to CO_2, CH_4 and Xe stimuli. *Journal of Materials Chemistry A* **2018**, *6*, 14231–14239.

[17] Xing, G.; Bassanetti, I.; Bracco, S.; Negroni, M.; Bezuidenhout, C.; Ben, T.; Sozzani, P.; Comotti, A. A double helix of opposite charges to form channels with unique CO_2 selectivity and dynamics. *Chemical Science* **2019**, *10*, 730–736.

[18] Lee, Y. J.; Murakhtina, T.; Sebastiani, D.; Spiess, H. W. ^{2}H solid-state NMR of mobile protons: it is not always the simple way. *Journal of the American Chemical Society* **2007**, *129*, 12406–12407.

[19] Hologne, M.; Chevelkov, V.; Reif, B. Deuterated peptides and proteins in MAS solid-state NMR. *Progress in Nuclear Magnetic Resonance Spectroscopy* **2006**, *48*, 211–232.

[20] Frischmann, P. D.; Facey, G. A.; Ghi, P. Y.; Gallant, A. J.; Bryce, D. L.; Lelj, F.; MacLachlan, M. J. Capsule formation, carboxylate exchange, and DFT exploration of cadmium cluster metallocavitands: highly dynamic supramolecules. *Journal of the American Chemical Society* **2010**, *132*, 3893–3908.

[21] Van Vleck, J. H. On dielectric constants and magnetic susceptibilities in the new quantum mechanics part III—Application to dia- and paramagnetism. *Physical Reviews* **1928**, *31*, 587–613.

[22] Goc, R. Calculation of the NMR second moment for materials with different types of internal rotation. *Solid State Nuclear Magnetic Resonance* **1998**, *13*, 55–61.

[23] Goc, R. Effective spatial averaging for NMR second moment calculation. *Journal of Magnetic Resonance* **1998**, *132*, 78–80.

[24] Gutowsky, H. S.; Pake, G. E. Structural investigations by means of nuclear magnetism. II. Hindered rotation in solids. *The Journal of Chemical Physics* **1950**, *18*, 162–170.

[25] Goc, R. Computer calculation of the Van Vleck second moment for materials with internal rotation of spin groups. *Computer Physics Communications* **2004**, *162*, 102–112.

[26] Goc, R. Simulation of the NMR second moment as a function of temperature in the presence of molecular motion. Application to $(CH_3)_3NBH_3$. *Zeitschrift für Naturforschung A* **2002**, *57*.

[27] Lowe, I. J. Free induction decays of rotating solids. *Physical Review Letters* **1959**, *2*, 285–287.

[28] Andrew, E. R.; Bradbury, A.; Eades, R. G. Removal of dipolar broadening of nuclear magnetic resonance spectra of solids by specimen rotation. *Nature* **1959**, *183*, 1802–1803.

[29] MacKenzie, K. J.; Smith, M. *Multinuclear Solid-State Nuclear Magnetic Resonance of Inorganic Materials, Vol. 6*; Pergamon, 2002.

[30] Walstedt, R. E. *The NMR Probe of High-Tech Materials*; Springer, 2010.

[31] Goldfarb, D.; Stoll, S. *EPR Spectroscopy: Fundamentals and Methods*; Wiley, 2018.

[32] Bloembergen, N.; Purcell, E. M.; Pound, R. V. Relaxation effects in nuclear magnetic resonance absorption. *Physical Review* **1948**, *73*, 679–712.

[33] Kubo, R.; Tomita, K. A general theory of magnetic resonance absorption. *Journal of the Physical Society of Japan* **1954**, *9*, 888–919.

[34] Reiser, M.; Semmler, W.; Hricak, H. *Magnetic Resonance Tomography*; Springer Berlin Heidelberg, 2007.

[35] Bruch, M. *NMR Spectroscopy Techniques, Second Edition,*; Practical Spectroscopy; Taylor & Francis, 1996.

[36] Sass, M.; Ziessow, D. Error analysis for optimized inversion recovery spin-lattice relaxation measurements. *Journal of Magnetic Resonance (1969)* **1977**, *25*, 263–276.

[37] Tipson, R.; Horton, D. *Advances in Carbohydrate Chemistry and Biochemistry*; Advances in Carbohydrate Chemistry and Biochemistry v. 45; Elsevier Science, 1988.

[38] Fyfe, C. *Solid State NMR for Chemists*; C.F.C. Press, 1983.

[39] Stejskal, E.; Memory, J. *High Resolution NMR in the Solid State: Fundamentals of CP/MAS*; Oxford University Press, 1994.

[40] Torchia, D. A. The measurement of proton-enhanced carbon-13 T_1 values by a method which suppresses artifacts. *Journal of Magnetic Resonance* **1978**, *30*, 613–616.

[41] Alamo, R.; Blanco, J.; Carrilero, I.; Fu, R. Measurement of the ^{13}C spin–lattice relaxation time of the non-crystalline regions of semicrystalline polymers by a CP MAS-based method. *Polymer* **2002**, *43*, 1857–1865.

[42] Fu, R.; Li, J.; Cui, J.; Peng, X. Revisiting spin–lattice relaxation time measurements for dilute spins in high-resolution solid-state NMR spectroscopy. *Journal of Magnetic Resonance* **2016**, *268*, 107–113.

[43] Cui, J.; Li, J.; Peng, X.; Fu, R. Transient NOE enhancement in solid-state MAS NMR of mobile systems. *Journal of Magnetic Resonance* **2017**, *284*, 73–79.

[44] Beckmann, P. A.; Schneider, E. Methyl group rotation, ^1H spin-lattice relaxation in an organic solid, and the analysis of nonexponential relaxation. *The Journal of Chemical Physics* **2012**, *136*, 054508.

[45] Todeschini, R.; Consonni, V.; Mannhold, R.; Kubinyi, H.; Timmerman, H. *Handbook of Molecular Descriptors*; Methods and Principles in Medicinal Chemistry; Wiley, 2008.

[46] Owen, N. L. *Internal Rotation in Molecules*; Wiley monographs in chemical physics; Wiley-Interscience, 1974; Chapter 5, pp 150 – 200.

[47] Vogelsberg, C. S.; Uribe-Romo, F. J.; Lipton, A. S.; Yang, S.; Houk, K. N.; Brown, S.; Garcia-Garibay, M. A. Ultrafast rotation in an amphidynamic crystalline metal organic framework. *Proceedings of the National Academy of Sciences* **2017**, *114*, 13613–13618.

[48] Beckmann, P. A.; Dybowski, C.; Gaffney, E. J.; Mallory, C. W.; Mallory, F. B. Methyl group rotation and ^1H and ^2H Zeeman relaxation in organic solids. *The Journal of Physical Chemistry A* **2001**, *105*, 7350–7355.

[49] Andrew, E.; Latanowicz, L. Solid-state proton transfer dynamics and the proton NMR second moment and proton relaxation rates. *Journal of Magnetic Resonance* **1986**, *68*, 232–239.

[50] Latanowicz, L.; Andrew, E.; Reynhardt, E. Second moment of an NMR spectrum of a solid narrowed by molecular jumps in potential wells with nonequivalent sites. *Journal of Magnetic Resonance, Series A* **1994**, *107*, 194–202.

[51] Reynhardt, E.; Latanowicz, L. Molecular motions in solid saccharides studied by NMR spectroscopy. *Chemical Physics Letters* **1996**, *251*, 235–241.

[52] Peng, J. W.; Wagner, G. Mapping of spectral density functions using heteronuclear NMR relaxation measurements. *Journal of Magnetic Resonance* **1992**, *98*, 308–332.

[53] Valiullin, R. *Diffusion NMR of Confined Systems: Fluid Transport in Porous Solids and Heterogeneous Materials*; New Developments in NMR; Royal Society of Chemistry, 2016.

[54] Aligizaki, K. *Pore Structure of Cement-Based Materials: Testing, Interpretation and Requirements*; Modern Concrete Technology; Taylor & Francis, 2005.

[55] Xu, T.; Haw, J. The development and applications of CAVERN methods for in situ NMR studies of reactions on solid acids. *Topics in Catalysis* **1997**, *4*, 109–118.

5. Hyperpolarization

Signals in NMR have intensities correlated to the polarization of nuclear spin levels. The population of these levels is governed by the Boltzmann distribution, so the polarization is proportionally inverse to temperature and proportionally direct to the applied field. However, there are always some limitations to the maximum applicable field and the minimal achievable temperature (especially for biomedical applications).[1]

It is possible to artificially increase the polarization well above the thermal equilibrium. The first demonstration was performed by Carver and Slitcher in 1953 on ^{7}Li,[2] with a good enhancement. Lately the increase of the polarization above thermal equilibrium has been called hyperpolarization (HP) and is quantified by the factor ϵ called polarization enhancement which can be of a few orders of magnitude.[3]

5.1 Strategies

After more than 60 years from the first hyperpolarization experiments, the methodology has evolved into more complex and efficient systems capable of obtaining enhancements of orders of magnitude. The existing techniques are:[4,5]

- DNP: Dynamic Nuclear Polarization
- SEOP: Spin Exchange Optical Pumping
- MEOP: Metastability Exchange Optical Pumping
- PHIP: ParaHydrogen Induced Polarization
- SABRE: Signal Amplification By Reversible Exchange

All this experiments are incredibly complex and usually have very specific applications. For this reason I will present in detail only those used in this thesis.

5.2 Dynamic Nuclear Polarization (DNP)

Historically, this was the first hyperpolarization and was theorized by Overhauser in 1953.[6] This led to the previously mentioned experiment of Carver and Slitcher. Nowadays the method has evolved, going beyond metal samples and becoming widely used for both organic and inorganic compounds.[7]

Mechanisms

Inside a magnetic field not only the nuclei polarize but also the electrons. The polarization depends by the gyromagnetic ratio (γ) which for the electron is 685 times the proton ratio.[8] The idea is to transfer this polarization to the desire nuclei using microwaves and thus enhance their signal.[9] There are several possible mechanisms for DNP and they strongly depend on field, temperature and polarization target.

For the sake of clarity, I will use some modified Salomon diagrams to highlight transitions and state population identifying with I the nuclear (assuming $\gamma > 0$) and with S the electron spin (Fig. 5.1).

Overhauser Effect

This is the first DNP mechanism used and rely on a system with mobile electrons such as metals. The microwave source is tuned on the EPR transition which leads to an increase population in the excited state. The system can relax with the classical single quantum (SQ) transition than with forbidden zero quantum (ZQ) or double quantum (DQ) transitions. The imbalance between the two ZQ and DQ transition rates leads to the enhancement (Fig. 5.2).[10]

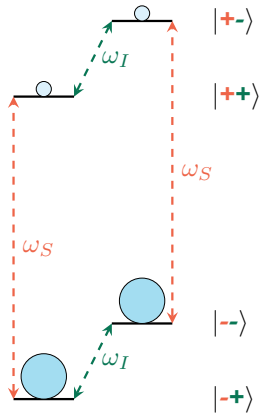

Figure 5.1: Equilibrium energy levels diagram with EPR (**orange**) and NMR (**green**) transitions.

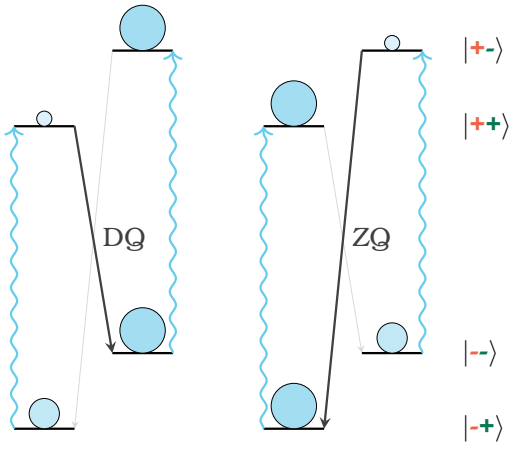

Figure 5.2: DNP Overhauser effect. Negative (left) and positive (right) enhancement. The microwave radiation ω_S is also presented (**light blue**).

This mechanism is usually limited to metals and liquids,[11] but Overhauser Effect was also recently observed in insulating solid[12] and is under deeper investigation.[13,14]

Solid Effect

The solid effect is very similar to the Overhauser effect but the microwave radiation is tuned on one of the two forbidden transitions (ZQ or DQ). This radiation perturbs the Hamiltonian and the energy levels are mixed by a mixing coefficient q. As a result, ZQ and DQ transitions become slightly allowed and can yield to the enhancement (Fig. 5.3).

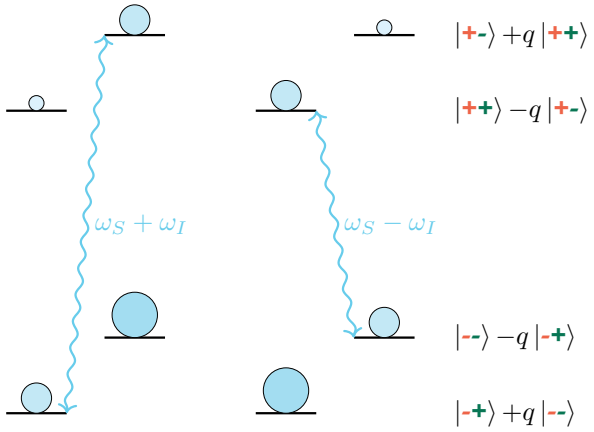

Figure 5.3: DNP Solid effect. Negative (left) and positive (right) enhancement. The microwave radiations are also presented (**light blue**).[15]

The transition probability is proportional to ω_I^{-2} so the solid effect becomes less efficient at high magnetic fields (>3 T) and must be compensated with higher microwave power. It is also possible to achieve good enhancement at high fields using polarizing agents with high molecular symmetry or transition metals complexes.[10,11,15]

Cross Effect

At high fields, it is possible to obtain a three spin polarization transfer (2 electrons and 1 nucleus) matching the condition $\omega_I = |\omega_{S_1} - \omega_{S_2}|$. In figure 5.4 it is possible to see that in this condition the central energy levels are degenerate, leading to the saturation of the four connected energy levels. Also in this case the enhancement can be positive or negative.

Cross effect is often present with solid effect, especially in static samples at low temperature (<10 K).[10,15]

The usual polarizing agents are biradicals containing two tethered nitroxide moieties, but it is also possible with other radicals such as TEMPO.[16]

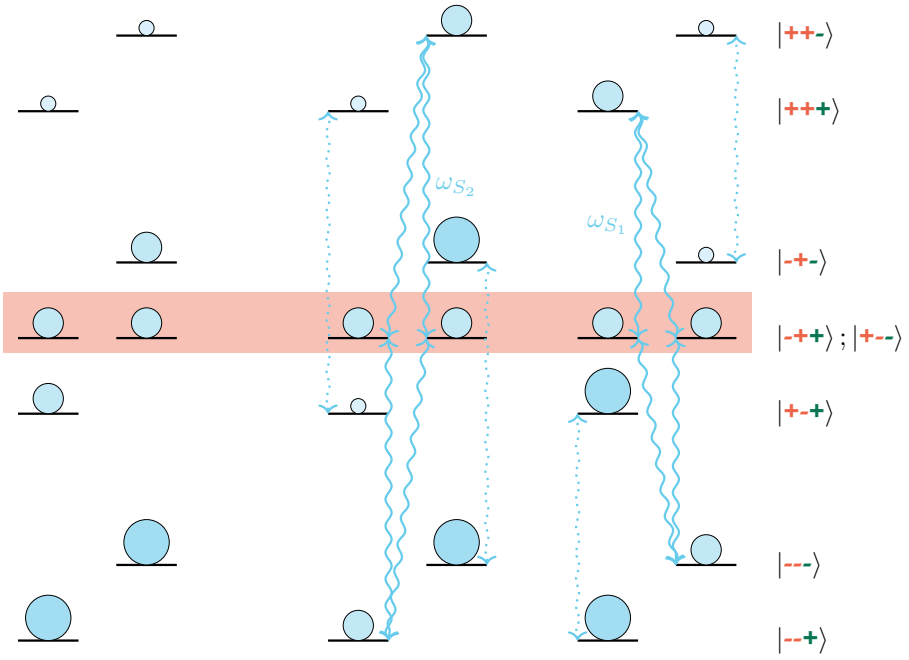

Figure 5.4: DNP Cross effect. Equilibrium (left), negative (center) and positive (right) enhancement. The degenerate ideal states are highlighted. The microwave radiations are also presented (light blue). [15]

Thermal Mixing

There are several possible models for thermal mixing, each with slightly changes. In general it is possible to state that microwave radiation disturbs the electron energy distribution and the system reacts with spin diffusion to find a steady state different from the initial Boltzmann equilibrium. Using the three spins model introduced for cross effect, also the nuclear population is perturbed. [16–19]

Polarizing Agents

DNP requires unpaired electrons in the system, but they are not present in all materials. To solve the problem, multi-radical molecules or transition metal ions are added during sample preparation as polarizing agents.

The concentration of these unpaired electrons must be diluted to reduce the paramagnetic broadening of NMR, so they are usually dissolved within a solution (which is frozen during the experiment). [20]

Solvent

The choice of solvent is particularly complex and varies from sample to sample. A good solvent must be able to dissolve the polarizing agent without altering the sample, it must have a good number of protons to allow spin diffusion but not so much to reduce the enhancement and it must also form amorphous glass upon freezing. [21,22]

The most common solvent is a mixture of 60% glycerol-d_8/ 30% D_2O/ 10% H_2O in volume, also known as "DNP juice". Sometimes the glycerol can be substituted by DMSO-d_6. [23]

TEMPO

Also known as 2,2,6,6-tetramethyl-1-piperidiny-1-oxyl, this is the most common and simple polarizing agent (Fig. 5.5). It is very soluble in water and the enhancement is achieved through cross effect. [15,23]

TOTALPOL

The biggest limit of TEMPO is that it must be present in high concentration

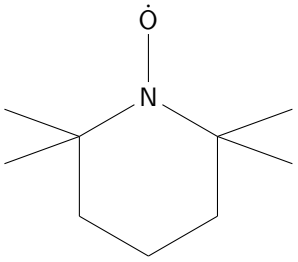

Figure 5.5: TEMPO radical.

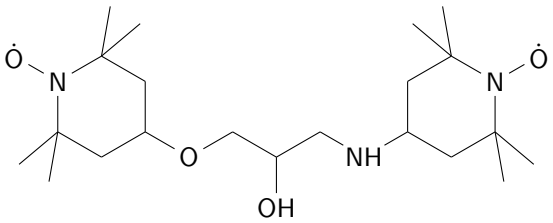

Figure 5.6: TOTALPOL radical.

to achieve a good electron-electron dipolar coupling. This intermolecular coupling leads to undesirable line broadening in the NMR spectra. A common approach is to create bis-TEMPO radicals which, due to the covalent tethering of the two radicals, present better coupling at a lower concentration. TOTALPOL is one of the first examples and is frequently used (Fig. 5.6).

Similar in design but with a better enhancemet is the bTbk. Unfortunately, its spare solubility in water/glycerol mixtures strongly limits its applications even if there are studies to improve it.[24]

AMUPol

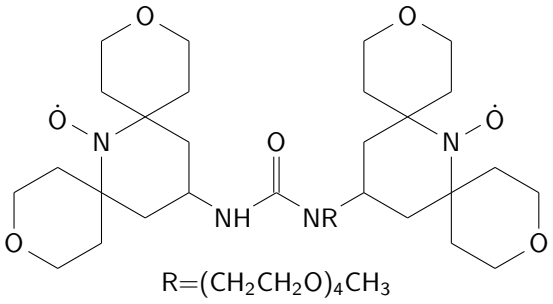

Figure 5.7: AMUPol radical.

A common approach to increase the enhancement was to replace geminal dimethyl groups with heavier moieties. This increases the rigidity of the radical, slowing the electron relaxation rate. AMUPol is a direct evolution of TOTALPOL following this theory and presents a larger enhancement especially in the high fields (Fig. 5.7). The better cross effect is also due to a stronger ee exchange interaction.[23,25]

Following the same idea, TEKPol was created from bTbk. It has the same solubility problems as bTbk and is often used in TCE mixtures.[23]

Metal Ions

Open-shell metal ions feature one or more unpaired electrons available for DNP. Some of the early experiments were performed using Ce(III) and Cr(V). The interest in these polarizing agents was limited by instrumentation constrains. In 2011 the use of Gd(III) and Mn(II) bound in complexes of chelators DOTA and DTPA began. Manganese has an important biological relevance and is studied as an endogenous polarizing agent in biomolecular systems.[23,26]

Microwave Sources

The main constraint in choosing the microwave source is the power. There are many ways to generate radiation in the microwave range, but only few of them can operate at high power.[27]

DNP is very demanding; it needs not only high-power radiation but also frequency stability and long operating time. The typical source of choice is the gyrotron. Sometimes also less powerful sources are used (like Gunn diode) but they are rare and less efficient.[15]

Gyrotron

A gyrotron is composed by: an electron gun, magnets, cavity, output circuit and collector (Fig. 5.8). The electron gun generates a circular electron beam towards the main magnet. Generally the external magnetic field is generated by a superconducting solenoid at cryogenic temperatures. The

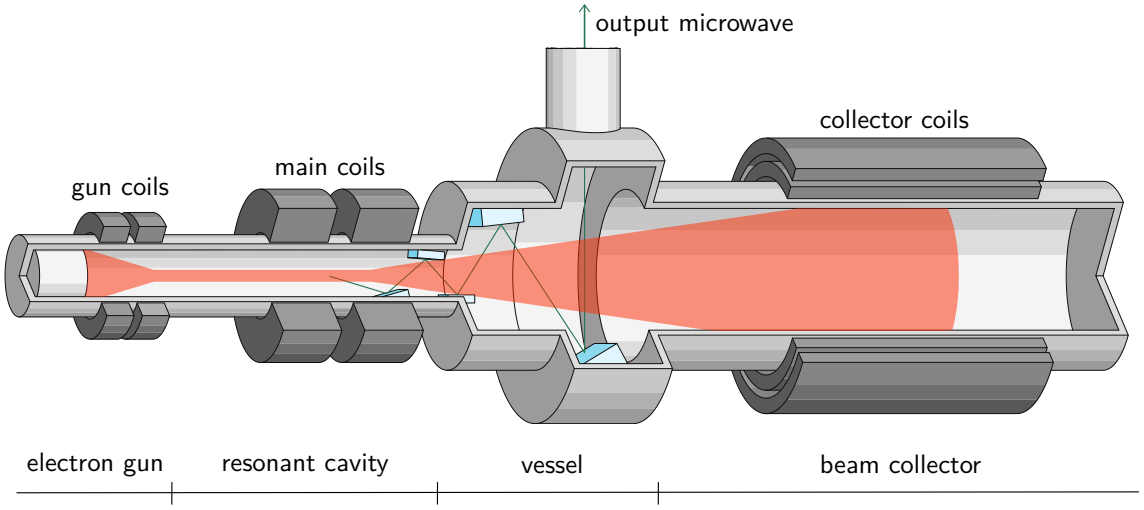

Figure 5.8: Schematic representation of a gyrotron. It is possible to see the electrons beam (orange) and the microwaves (green).[28]

beam is compressed by the field, which gradually becomes stronger until it reaches its maximum value in the centre of the solenoid. This area is called cavity and is where the desired microwaves are emitted, the frequency is a function of the magnetic field and the accelerating voltage. The microwaves interact strongly with the beam inside the cavity, are then collected by a system of mirrors and directed to the output waveguide. The residual electron beam is than scattered in a collector.[27]

Dissolution DNP

DNP in liquids can be achieved in low magnetic fields (< 1 T), while high field studies present significant problems. The main limitation is the availability of microwave sources with sufficient power, a problem now solved with the modern gyrotrons, but the high radiation power tends to overheat the sample. Liquid DNP at high fields is also limited to protons and there are few studies focused on low gyromagentic rateo nuclei.[29,30]

In 2003 a possible solution to this problem was presented: the dissolution DNP (dDNP). The main idea is to freeze a liquid sample with the polarizing agent at very low temperature (liquid helium and below) inside a low field magnet and start irradiating. When the polarization is sufficient, a liquid at high temperature is injected into the sample space where it dissolves the polarized solution. The mixture is than quickly transferred to a more powerful magnet where the measurement is performed.[31]

dDNP has great potential for clinical use, especially for *in vivo* imaging of different tissues.[32] It is also applied in chemistry for short T_1 nuclei analysis and for the study of reaction mechanism (including intermediate products).[33]

Developments

DNP offers many possibilities for further developments in many aspects. A great part of the research focuses on new ways of using this tool, such as using the spin diffusion to probe the homogeneity of a sample.[34] Other studies are instead focused on more efficient polarizing agents.[35,36] An interesting research is the creation of non persistent radical for clinical use.[37,38]

Much attention is paid to the instrumentation. From one side there is a great impulse to stretch the limits of this technique (for example with faster MAS rotation and lower temperatures) and from the other to make cheaper and smaller

microwave sources.[39]

During my stay at EPFL by prof. Lyndon Emsley I performed a few experiments applying DNP technique.

5.3 Spin-Exchange Optical Pumping (SEOP)

The first optical pumping can be dated back to 1897 with Zeeman studies of sodium vapours,[40] but it was Kastler in 1950 who discovered that rubidium could be electronically spin-polarized when placed in a magnetic field and illuminated with resonant circularly polarized light.[41] It would take other ten years before this polarization was first transferred to the nuclear spin of noble gases.[42]

Although the SEOP technique could be applied to any noble gas, it is generally associated with ^{129}Xe. It is also used for ^{3}He but it is a very rare and expensive isotope (it is typically obtained from tritium decay, while ^{129}Xe have a natural abundance of 26%). Other noble gas isotopes are quadrupolar and present faster T_1, limiting their use. However, ^{83}Kr is promising and sometimes used.[1]

Mechanism

The whole process is divided into two main parts: the first one is the hyperpolarization of the alkali metal and the second part is the transfer to the noble gas nuclei.

Optical Pumping

When some vapours of an alkali metal in a magnetic field are irradiated with the right light source, they can be hyperpolarized. The wavelength light of the D_1 transition cannot induce hyperpolarization because it excites both the sublevels $+1/2$ and $-1/2$ of the ground state $S_{1/2}$. However, if this radiation is circularly polarized (σ^+), only the electrons in the $-1/2$ sublevel can accommodate the extra angular momentum. These electrons are now in the sublevel $+1/2$ of $P_{1/2}$ and, according to the Clebsch-Gordon coefficients, have a $2/3$ probability to return to the $-1/2$ ground level and $1/3$ probability to relax to the $+1/2$ ground level (contributing to the polarization).[43]

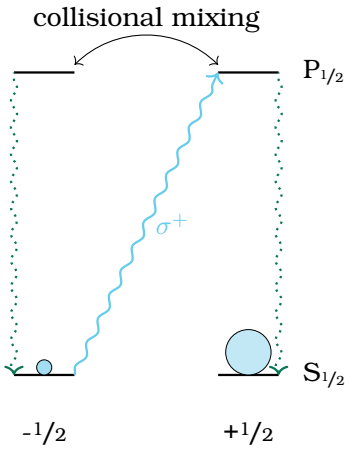

Figure 5.9: Simplified scheme of optical pumping of an alkali atom. The circularly polarized radiation (light blue) and the relaxations are presented (green).

With this mechanism, only one excited electron every 3 contributes to the polarization. The alkali vapours can collide with gases and this mixes the sublevels of $P_{1/2}$. In that situation, the probability of a favourable relaxation is 50% (Fig. 5.9). The gas for the collisional mixing must be inert.[44] The high chamber pressure also broad the alkali spectral lines, resulting in a more efficient light adsorption.

A major limitation of optical pumping is the radiation trapping. The relaxation from level $P_{1/2}$ involves the emission of an unpolarized photon that can depolarize many alkali atoms. To solve this problem, N_2 is often added to the gas mixture to quench the excited state non radiatively.[45]

It is possible to achieve good optical pumping with any alkali metal, but the most commonly used is rubidium. The choice is due to its good spin exchange cross section, to the high vapour pressure and to the optical transition wavelength (794.76 nm) which can be obtained

with low-cost laser sources. Cesium is also sometimes used and present some interesting advantages.[46]

It is worth remembering that alkali metals are very reactive with water; Rubidium and Cesium spontaneously ignite upon exposure to air.

Spin Exchange

The purpose of spin exchange is to transfer the electrical polarization of alkali vapour to the nucleus of the noble gas. The simplest way is a binary collision between vapour and gas, it is independent from the gas density.

A second and more interesting mechanism is the formation of long-lived Van der Waals complexes. In this configuration, the exchange is more efficient of a few orders of magnitude.[47] However, efficiency is low at high gas concentration because a collision can break the complex, especially a collision with other xenon atoms. Nitrogen is also able to breakthe complex but it also helps its formation through a three-body collision.[46]

Since the optical pumping is more efficient at high total pressure and the spin exchange is at a low polarizing gas concentration, the experiment is often performed on a gas mixture where the main component is a buffer gas. Typical buffer gases are nitrogen, helium and methane.[46]

Applications

SEOP technique enhance the signal of the target noble gas, so the applications are directly related to the properties of that gas. Although this may seem a limitation compared to other hyperpolarization techniques (such as DNP), the peculiar nature of noble gases makes it an interesting tool for very specific analysis.

MRI

Since 1994, xenon has been used as a contrast agent for magnetic resonance imaging.[48] However, the lungs are difficult to analyse due to the lack of protons, an abundance of air that induces field heterogeneities and respiratory motion.[49] Thanks to the SEOP technique, it is possible to easily obtain high quality images of lungs and also monitor the diffusion of gas inside the alveoli. Xenon is also lipophilic and soluble in biological tissues; thanks also to its long T_1, it was also possible to obtain functional images of lungs and brain.[50]

Probe for Porous Materials

Xenon is an invaluable probe for porous materials due to its sensitivity to the channel size and shape.[46] Hyperpolarization allows the use of xenon also for single crystals or the possibility of acquiring 2D experiments. While the first helps to better understand the channels orientations, the latter provides information on the pore connectivity.

The relation between ^{129}Xe chemical shift and pores was presented by Ito and Freissard in 1982.[51] It can be written as a sum of contributions:[52]

$$\delta = \delta_0 + \delta_{Xe} + \delta_S + \delta_{SAS} + \delta_E + \delta_M \qquad (5.1)$$

δ is the detected chemical shift;
δ_0 is the free gas chemical shift;
δ_{Xe} is due to Xe-Xe collisions;
δ_S is the surface interactions;
δ_{SAS} is due to strong adsorption sites;
δ_E is caused by electric fields;
δ_M is caused by magnetic fields.

The last two terms must be taken into account only in the case of materials that contain cations or paramagnetic particles.[53]

Assuming also the lack of strong adsorption sites, equation 5.1 can be rewritten as:

$$\delta = \delta_0 + \delta_{Xe}\rho_{Xe} + \delta_S x_{ads} \qquad (5.2)$$

ρ_{Xe} is the xenon density;
x_{ads} is the molar fraction of adsorbed xenon atoms.

In a SEOP experiment, the concentration of xenon is very low and δ_{Xe} tend to zero, δ_0

is a reference and can be set to zero but δ_S is a complicated function.[54]

Rewriting the formula expanding x_{ads} in mole n, we obtain:

$$\delta = \delta_S \frac{n_{ads}}{n_{ads} + n_{gas}} \tag{5.3}$$

Considering a simple Henry's adsorption model and the ideal gas behaviour:[55]

$$n_{ads} = KPS \tag{5.4}$$

$$n_{gas}RT = PV \tag{5.5}$$

K is the Henry constant;
S is the specific area.
Combining equations 5.3, 5.4 and 5.5:

$$\delta = \frac{\delta_S}{1 + \frac{V}{RKST}} \tag{5.6}$$

The constant K can be used to determine the enthalpy of adsorption of xenon (Q):[52]

$$K = K_0 \frac{e^{\frac{Q}{RT}}}{\sqrt{T}} \tag{5.7}$$

Performing different experiments at different temperatures, it is possible to obtain geometry (V and S) information about the channel and its interaction energy (Q) with xenon. The final Fraissard formula is:

$$\ln\left(\frac{\delta_S}{\delta - 1}\sqrt{T}\right) = \ln\frac{V}{SRK_0} - \frac{Q}{RT} \tag{5.8}$$

With HP xenon it is possible to study the change in porosity after surface functionalization of porous materials.[56–58] The technique is so sensitive that it was able to notice differences in mesoporous silica not visible with the study of N_2 adsorption or TEM observations.[59]

In single crystals, the signal of xenon changes according to the angle between the channels and the magnetic field. In this situation it is possible to isolate the contribution of Xe-Xe and Xe-wall interactions and analyse them separately. This type of study has opened up the possibility of describing the orientation of cavities.[60]

2D ^{129}Xe NMR chemical shift exchange spectroscopy (EXSY) is able to evaluate the interconnectivity between different regions of porous materials. It reveals not only the presence of exchange, but also the possible pathway and the timescale of the process; thanks to the proportionality of the cross-peaks to the exchange time. The experiment is quantitative but the resolution needed is extremely high, for this reason it is rarely applied without hyperpolarization. It has already been used in different porous materials, but it is more effective in case of fast diffusion and long relaxation times (like mesoporous materials).[61–67]

Xenon is also used to probe the connectivity in porous electrode materials for their use as anode in Li ion batteries. A good example is the TiO_2-graphene hybrid material, whose uniform nanoscale mixing was demonstrated by HP Xe NMR. The better channel connectivity enhances the transport property for Li-insertion/extraction.[68]

Bibliography

[1] Nikolaou, P.; Goodson, B. M.; Chekmenev, E. Y. NMR hyperpolarization techniques for biomedicine. *Chemistry - A European Journal* **2014**, *21*, 3156–3166.

[2] Carver, T. R.; Slichter, C. P. Polarization of nuclear spins in metals. *Physical Review* **1953**, *92*, 212–213.

[3] Ravera, E.; Parigi, G.; Luchinat, C. *Paramagnetism in Experimental Biomolecular NMR*; New Developments in NMR; Royal Society of Chemistry, 2018.

[4] Kuhn, L. *Hyperpolarization Methods in NMR Spectroscopy*; Topics in Current Chemistry; Springer Berlin Heidelberg, 2013.

[5] Albert, M.; Hane, F. *Hyperpolarized and Inert Gas MRI: From Technology to Application in Research and Medicine*; Elsevier Science, 2016.

[6] Overhauser, A. W. Polarization of nuclei in metals. *Physical Review* **1953**, *92*, 411–415.

[7] Rossini, A. J. Materials characterization by dynamic nuclear polarization-enhanced solid-state NMR spectroscopy. *The Journal of Physical Chemistry Letters* **2018**, *9*, 5150–5159.

[8] Codd, S.; Seymour, J. *Magnetic Resonance Microscopy: Spatially Resolved NMR Techniques and Applications*; Wiley, 2008.

[9] Zaidi, H. *Molecular Imaging of Small Animals: Instrumentation and Applications*; Springer New York, 2014.

[10] Can, T.; Ni, Q.; Griffin, R. Mechanisms of dynamic nuclear polarization in insulating solids. *Journal of Magnetic Resonance* **2015**, *253*, 23–35.

[11] Wenckebach, W. T. The solid effect. *Applied Magnetic Resonance* **2008**, *34*, 227–235.

[12] Can, T. V.; Caporini, M. A.; Mentink-Vigier, F.; Corzilius, B.; Walish, J. J.; Rosay, M.; Maas, W. E.; Baldus, M.; Vega, S.; Swager, T. M.; Griffin, R. G. Overhauser effects in insulating solids. *The Journal of Chemical Physics* **2014**, *141*, 064202.

[13] Ravera, E.; Luchinat, C.; Parigi, G. Basic facts and perspectives of Overhauser DNP NMR. *Journal of Magnetic Resonance* **2016**, *264*, 78–87.

[14] Pylaeva, S.; Ivanov, K. L.; Baldus, M.; Sebastiani, D.; Elgabarty, H. Molecular mechanism of Overhauser dynamic nuclear polarization in insulating solids. *The Journal of Physical Chemistry Letters* **2017**, *8*, 2137–2142.

[15] Ni, Q. Z.; Daviso, E.; Can, T. V.; Markhasin, E.; Jawla, S. K.; Swager, T. M.; Temkin, R. J.; Herzfeld, J.; Griffin, R. G. High frequency dynamic nuclear polarization. *Accounts of Chemical Research* **2013**, *46*, 1933–1941.

[16] Shimon, D.; Hovav, Y.; Feintuch, A.; Goldfarb, D.; Vega, S. Dynamic nuclear polarization in the solid state: a transition between the cross effect and the solid effect. *Physical Chemistry Chemical Physics* **2012**, *14*, 5729.

[17] Serra, S. C.; Rosso, A.; Tedoldi, F. Electron and nuclear spin dynamics in the thermal mixing model of dynamic nuclear polarization. *Physical Chemistry Chemical Physics* **2012**, *14*, 13299.

[18] Hovav, Y.; Feintuch, A.; Vega, S. Theoretical aspects of dynamic nuclear polarization in the solid state-spin temperature and thermal mixing. *Physical Chemistry Chemical Physics* **2013**, *15*, 188–203.

[19] Wenckebach, W. Dynamic nuclear polarization via thermal mixing: beyond the high temperature approximation. *Journal of Magnetic Resonance* **2017**, *277*, 68–78.

[20] Hu, K.-N. Polarizing agents and mechanisms for high-field dynamic nuclear polarization of frozen dielectric solids. *Solid State Nuclear Magnetic Resonance* **2011**, *40*, 31–41.

[21] Hu, K.-N.; Song, C.; hua Yu, H.; Swager, T. M.; Griffin, R. G. High-frequency dynamic nuclear polarization using biradicals: a multifrequency EPR lineshape analysis. *The Journal of Chemical Physics* **2008**, *128*, 052302.

[22] Leavesley, A.; Wilson, C. B.; Sherwin, M.; Han, S. Effect of water/glycerol polymorphism on dynamic nuclear polarization. *Physical Chemistry Chemical Physics* **2018**, *20*, 9897–9903.

[23] Thankamony, A. S. L.; Wittmann, J. J.; Kaushik, M.; Corzilius, B. Dynamic nuclear polarization for sensitivity enhancement in modern solid-state NMR. *Progress in Nuclear Magnetic Resonance Spectroscopy* **2017**, *103*, 120–195.

[24] Dane, E. L.; Corzilius, B.; Rizzato, E.; Stocker, P.; Maly, T.; Smith, A. A.; Griffin, R. G.; Ouari, O.; Tordo, P.; Swager, T. M. Rigid orthogonal bis-TEMPO biradicals with improved solubility for dynamic nuclear polarization. *The Journal of Organic Chemistry* **2012**, *77*, 1789–1797.

[25] Gast, P.; Mance, D.; Zurlo, E.; Ivanov, K. L.; Baldus, M.; Huber, M. A tailored multi-frequency EPR approach to accurately determine the magnetic resonance parameters of dynamic nuclear polarization agents: application to AMUPol. *Physical Chemistry Chemical Physics* **2017**, *19*, 3777–3781.

[26] Corzilius, B. Paramagnetic metal ions for dynamic nuclear polarization. *eMagRes* **2018**, *7*, 179–194.

[27] Hruszowiec, M.; Czarczyski, W.; Plinski, E. F.; Wickowski, T. Gyrotron technology. *Journal of Telecommunications and Information Technology* **2014**, *1*, 68–76.

[28] Sosa, E. N. Electron tube. *Encyclopædia Britannica* **2013**,

[29] Neugebauer, P.; Krummenacker, J. G.; Denysenkov, V. P.; Helmling, C.; Luchinat, C.; Parigi, G.; Prisner, T. F. High-field liquid state NMR hyperpolarization: a combined DNP/NMRD approach. *Physical Chemistry Chemical Physics* **2014**, *16*, 18781–18787.

[30] Bennati, M.; Orlando, T. Overhauser DNP in Liquids on ^{13}C Nuclei. *eMagRes* **2019**, *8*, 11–18.

[31] Ardenkjær-Larsen, J. H.; Fridlund, B.; Gram, A.; Hansson, G.; Hansson, L.; Lerche, M. H.; Servin, R.; Thaning, M.; Golman, K. Increase in signal-to-noise ratio of > 10, 000 times in liquid-state NMR. *Proceedings of the National Academy of Sciences* **2003**, *100*, 10158–10163.

[32] Ardenkjær-Larsen, J. H. On the present and future of dissolution-DNP. *Journal of Magnetic Resonance* **2016**, *264*, 3–12.

[33] Jensen, P. R.; Meier, S.; Ardenkjær-Larsen, J. H.; Duus, J. Ø.; Karlsson, M.; Lerche, M. H. Detection of low-populated reaction intermediates with hyperpolarized NMR. *Chemical Communications* **2009**, 5168.

[34] Rankin, A. G.; Trébosc, J.; Pourpoint, F.; Amoureux, J.-P.; Lafon, O. Recent developments in MAS DNP-NMR of materials. *Solid State Nuclear Magnetic Resonance* **2019**, *101*, 116–143.

[35] Kubicki, D. J.; Casano, G.; Schwarzwälder, M.; Abel, S.; Sauvée, C.; Ganesan, K.; Yulikov, M.; Rossini, A. J.; Jeschke, G.; Copéret, C.; Lesage, A.; Tordo, P.; Ouari, O.; Emsley, L. Rational design of dinitroxide biradicals for efficient cross-effect dynamic nuclear polarization. *Chemical Science* **2016**, *7*, 550–558.

[36] Thurber, K. R.; Le, T.-N.; Change-coco, V.; Brook, D. J. Verdazyl-ribose: a new radical for solid-state dynamic nuclear polarization at high magnetic field. *Journal of Magnetic Resonance* **2018**, *289*, 122–131.

[37] Eichhorn, T. R.; Takado, Y.; Salameh, N.; Capozzi, A.; Cheng, T.; Hyacinthe, J.-N.; Mishkovsky, M.; Roussel, C.; Comment, A. Hyperpolarization without persistent radicals for in vivo real-time metabolic imaging. *Proceedings of the National Academy of Sciences* **2013**, *110*, 18064–18069.

[38] Capozzi, A.; Hyacinthe, J.-N.; Cheng, T.; Eichhorn, T. R.; Boero, G.; Roussel, C.; van der Klink, J. J.; Comment, A. Photoinduced nonpersistent radicals as polarizing agents for x-nuclei dissolution dynamic nuclear polarization. *The Journal of Physical Chemistry C* **2015**, *119*, 22632–22639.

[39] Rosay, M.; Blank, M.; Engelke, F. Instrumentation for solid-state dynamic nuclear polarization with magic angle spinning NMR. *Journal of Magnetic Resonance* **2016**, *264*, 88–98.

[40] Zeeman, P. The effect of magnetisation on the nature of light emitted by a substance. *Nature* **1897**, *55*, 347–347.

[41] Kastler, A. Quelques suggestions concernant la production optique et la détection optique d'une inégalité de population des niveaux de quantifigation spatiale des atomes. Application à l'expérience de Stern et Gerlach et à la résonance magnétique. *Journal de Physique et le Radium* **1950**, *11*, 255–265.

[42] Bouchiat, M. A.; Carver, T. R.; Varnum, C. M. Nuclear polarization in ^{3}He gas induced by optical pumping and dipolar exchange. *Physical Review Letters* **1960**, *5*, 373–375.

[43] Happer, W. Optical pumping. *Reviews of Modern Physics* **1972**, *44*, 169–249.

[44] Vo-Dinh, T. *Biomedical Photonics Handbook*; SPIE press monograph; CRC Press, 2003.

[45] Kimura, M.; Walther, H. *Advances in Atomic, Molecular, and Optical Physics*; Advances in Atomic, Molecular, and Optical Physics v. 45; Elsevier Science, 2000.

[46] Meersmann, T., Brunner, E., Eds. *Hyperpolarized Xenon-129 Magnetic Resonance*; Royal Society of Chemistry, 2015.

[47] Rice, C. V.; Raftery, D. Rubidiumxenon spin exchange and relaxation rates measured at high pressure and high magnetic field. *The Journal of Chemical Physics* **2002**, *117*, 5632–5641.

[48] Albert, M. S.; Cates, G. D.; Driehuys, B.; Happer, W.; Saam, B.; Springer, C. S.; Wishnia, A. Biological magnetic resonance imaging using laser-polarized ^{129}Xe. *Nature* **1994**, *370*, 199–201.

[49] Kauczor, H.-U.; Kreitner, K.-F. MRI of the pulmonary parenchyma. *European Radiology* **1999**, *9*, 1755–1764.

[50] Barskiy, D. A. et al. NMR hyperpolarization techniques of gases. *Chemistry - A European Journal* **2016**, *23*, 725–751.

[51] Ito, T.; Fraissard, J. ^{129}Xe NMR study of xenon adsorbed on Y zeolites. *The Journal of Chemical Physics* **1982**, *76*, 5225–5229.

[52] Filimonova, S.; Nossov, A.; Dümig, A.; Gédéon, A.; Kögel-Knabner, I.; Knicker, H. Evaluating pore structures of soil components with a combination of "conventional" and hyperpolarised ^{129}Xe NMR studies. *Geoderma* **2011**, *162*, 96–106.

[53] Romanenko, K. V.; Lapina, O. B.; Py, X.; Fraissard, J. ^{129}Xe NMR spectroscopy of adsorbed xenon: possibilities for exploration of microporous carbon materials. *Russian Journal of General Chemistry* **2008**, 2171–2181.

[54] Ripmeester, J. A.; Ratcliffe, C. I. On the application of ^{129}xenon NMR to the study of microporous solids. *The Journal of Physical Chemistry* **1990**, *94*, 7652–7656.

[55] Terskikh, V. V.; Mudrakovskii, I. L.; Mastikhin, V. M. ^{129}Xe nuclear magnetic resonance studies of the porous structure of silica gels. *Journal of the Chemical Society, Faraday Transactions* **1993**, *89*, 4239.

[56] Huang, S.-J.; Huang, C.-H.; Chen, W.-H.; Sun, X.; Zeng, X.; Lee, H.-K.; Ripmeester, J. A.; Mou, C.-Y.; Liu, S.-B. Probing the alkyl ligands on silylated mesoporous MCM-41 using hyperpolarized ^{129} Xe NMR spectroscopy. *The Journal of Physical Chemistry B* **2005**, *109*, 681–684.

[57] Lo, A.-Y.; Liu, S.-H.; Huang, S.-J.; Shen, H.-K.; Kuo, C.-T.; Liu, S.-B. *Studies in Surface Science and Catalysis*; Elsevier, 2007; Vol. 165; pp 409–412.

[58] Nader, M.; Guenneau, F.; Boissiere, C.; Grosso, D.; Sanchez, C.; Gédéon, A. *Studies in Surface Science and Catalysis*; Elsevier, 2007; Vol. 165; pp 555–558.

[59] A ^{129}Xe NMR study of functionalized ordered mesoporous silic.

[60] Comotti, A.; Bracco, S.; Ferretti, L.; Mauri, M.; Simonutti, R.; Sozzani, P. A single-crystal imprints macroscopic orientation on xenon atoms. *Chemical Communications* **2007**, 350–352.

[61] Larsen, R.; Shore, J.; Schmidt-Rohr, K.; Emsley, L.; Long, H.; Pines, A.; Janicke, M.; Chmelka, B. NMR study of xenon dynamics and energetics in NaA zeolite. *Chemical Physics Letters* **1993**, *214*, 220–226.

[62] Moudrakovski, I.; Ratcliffe, C.; Ripmeester, J. *Studies in surface science and catalysis*; 1995; Vol. 97; pp 243–250.

[63] Moudrakovski, I. L.; Wang, L.-Q.; Baumann, T.; Satcher, J. H.; Exarhos, G. J.; Ratcliffe, C. I.; Ripmeester, J. A. Probing the geometry and interconnectivity of pores in organic aerogels using hyperpolarized ^{129}Xe NMR spectroscopy. *Journal of the American Chemical Society* **2004**, *126*, 5052–5053.

[64] Comotti, A.; Bracco, S.; Valsesia, P.; Ferretti, L.; Sozzani, P. 2D multinuclear NMR, hyperpolarized xenon and gas storage in organosilica nanochannels with crystalline order in the walls. *Journal of the American Chemical Society* **2007**, *129*, 8566–8576.

[65] Comotti, A.; Bracco, S.; Sozzani, P.; Horike, S.; Matsuda, R.; Chen, J.; Takata, M.; Kubota, Y.; Kitagawa, S. Nanochannels of two distinct cross-sections in a porous Al-based coordination polymer. *Journal of the American Chemical Society* **2008**, *130*, 13664–13672.

[66] Keenan, C. D.; Herling, M. M.; Siegel, R.; Petzold, N.; Bowers, C. R.; Rössler, E. A.; Breu, J.; Senker, J. Porosity of pillared clays studied by hyperpolarized ^{129}Xe NMR spectroscopy and Xe adsorption isotherms. *Langmuir* **2013**, *29*, 643–652.

[67] Giovine, R.; Volkringer, C.; Springuel-Huet, M.-A.; Nossov, A.; Blanc, F.; Trébosc, J.; Loiseau, T.; Amoureux, J.-P.; Lafon, O.; Pourpoint, F. Study of xenon mobility in the two forms of MIL-53(Al) using solid-state NMR spectroscopy. *The Journal of Physical Chemistry C* **2017**, *121*, 19262–19268.

[68] Wang, L.-Q.; Wang, D.; Liu, J.; Exarhos, G. J. Probing porosity and pore interconnectivity in self-assembled TiO_2graphene hybrid hanostructures using hyperpolarized ^{129}Xe NMR. *The Journal of Physical Chemistry C* **2012**, *116*, 22–29.

6. Rotor-Gas Interaction

Summary

Void space in a porous material is used both for gas adsorption and for rotor dynamics. In literature there are some examples of rotor-gas interactions, especially with the *p*-phenylene moieties used as molecular rotors. The adsorption of guest molecules can slow down the rotor dynamics by increasing its activation energy[1] or by completely hampering the motion.[2,3]

My purpose is to build new molecular rotors in porous materials and to study the rotor-guest interactions in depth using CO_2 as a guest. Due to the great interest in this field, there are many suitable porous materials with high gas adsorption and high-speed molecular rotors.[4] Another important factor is the good affinity between CO_2 and *p*-phenylene rotors,[5] that create interactions and gradually slow down the motion with the CO_2 loading.

6.1 Molecular Rotors in a Porous Organic Framework

The first materials analysed are two porous organic crystals synthesized for this study, in particular one containing *p*-phenylene units and the other with deuterated central aromatic rings. They belong to the family of organic porous materials held together by the charge-assisted hydrogen bonds between sulfonate anions and ammonium cations. They exhibit a low rotation energy barrier as measured by ^{2}H NMR. The main goal is to build fast molecular rotors and modulate its dynamic by the adsorption of CO_2.[6]

Crystal Structure

The structure is created by the precipitation of BSPEB (4,4'-bis(sulfophenylethynyl)benzene) and *n*-benzylammonium during the slow evaporation of the solvent (1,4-dioxane). The system is formed by a series of non-

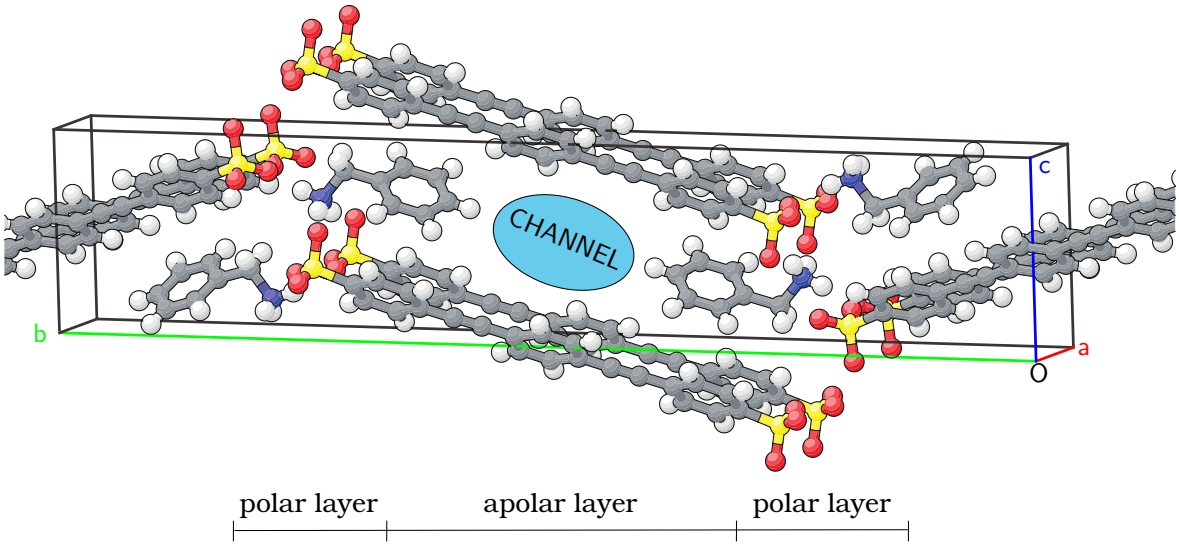

Figure 6.1: Crystal structure of BSPEB and *n*-benzylamine.

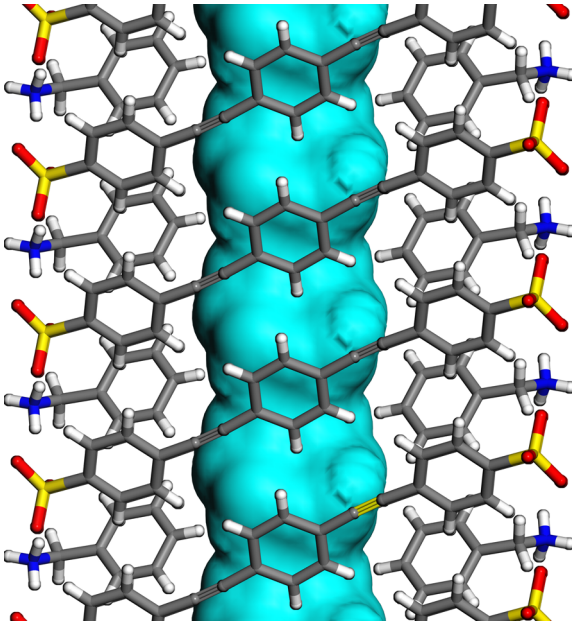

Figure 6.2: Crystal structure of the permanently porous compound as viewed perpendicular to the channel axis. The empty channel is calculated by a sphere of 1.65 Å.

polar layers and polar double-layers consisting in a 2D hydrogen bond network (Fig. 6.1).

The crystal structure reveals a series of parallel and independent channels in the non-polar layers, with a rectangular cross section of 4.4 x 7.5 $Å^2$. The rotors are directly exposed to the pores; considering that each aromatic ring possesses a lateral van der Waals hindrance around 1.7 Å (Fig. 6.2), a complete rotation is expected.

X-ray diffraction data show no change in crystal structure after CO_2 adsorption up to 10 bar. No substantial changes were observed from 298 K to 130 K, indicating the maintenance of the porous architecture with temperature.

Gas Adsorption

The porosity of the system was confirmed by the adsorption isotherm of N_2 at 77 K, revealing a structure with surface areas of 332 m^2/g (Langmuir) and 291 m^2/g (BET).

CO_2 adsorption isotherm (Fig. 6.3) show a Langmuir profile, with an uptake of 86 cm^3/g at p/p^0 = 0.97 at 195 K. This result is consistent with 2 CO_2 moles per mole of host, corresponding to the complete filling of the structure. Isotherms at 273 K and 298 K reach the 80 % filling at 5 bar and 10 bar respectively. The uptake is comparable to that of best-performing porous molecular crystals containing 1D channels with similar cross-sections.[7–10]

The calculated CO_2 isosteric heat of adsorption by van't Hoff equation (see chapter 2) is 30 kJ/mol at low coverage (< 5 cm^3/ g) and 27 kJ/mol above 10 cm^3/ g. These values are compatible with the adsorption of CO_2 in the electron-rich environment of the π-system.[11]

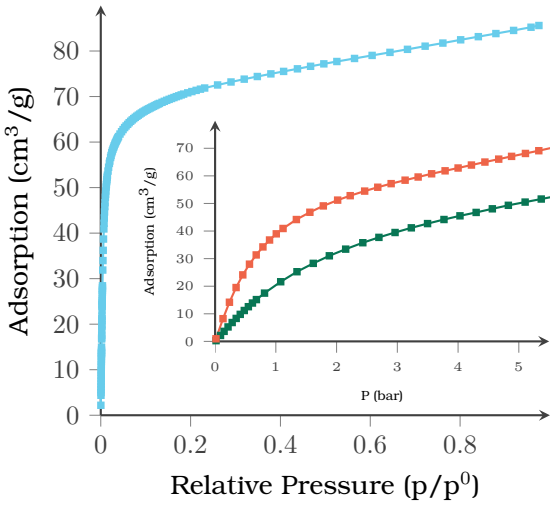

Figure 6.3: CO_2 isotherms of the deuterated compound at 195 K (light blue), 273 K (orange) and 298 K (green).

MAS NMR Spectroscopy

Both porous materials, with deuterated and non-deuterated central *p*-phenylene moiety, were analysed with ^{13}C MAS NMR spectroscopy and show similar spectra (Fig. 6.4). Notably, carbon 10 and 11 are shifted upfield due to the deuterium substitution. The ^{13}C T_1 NMR study at room temperature measures a relaxation time of 0.5 s for carbon 10 and 11, suggesting the presence of a high motion rate.

The deuterated sample was loaded with gas at 2 bar and the 2D ^1H-^{13}C hetero

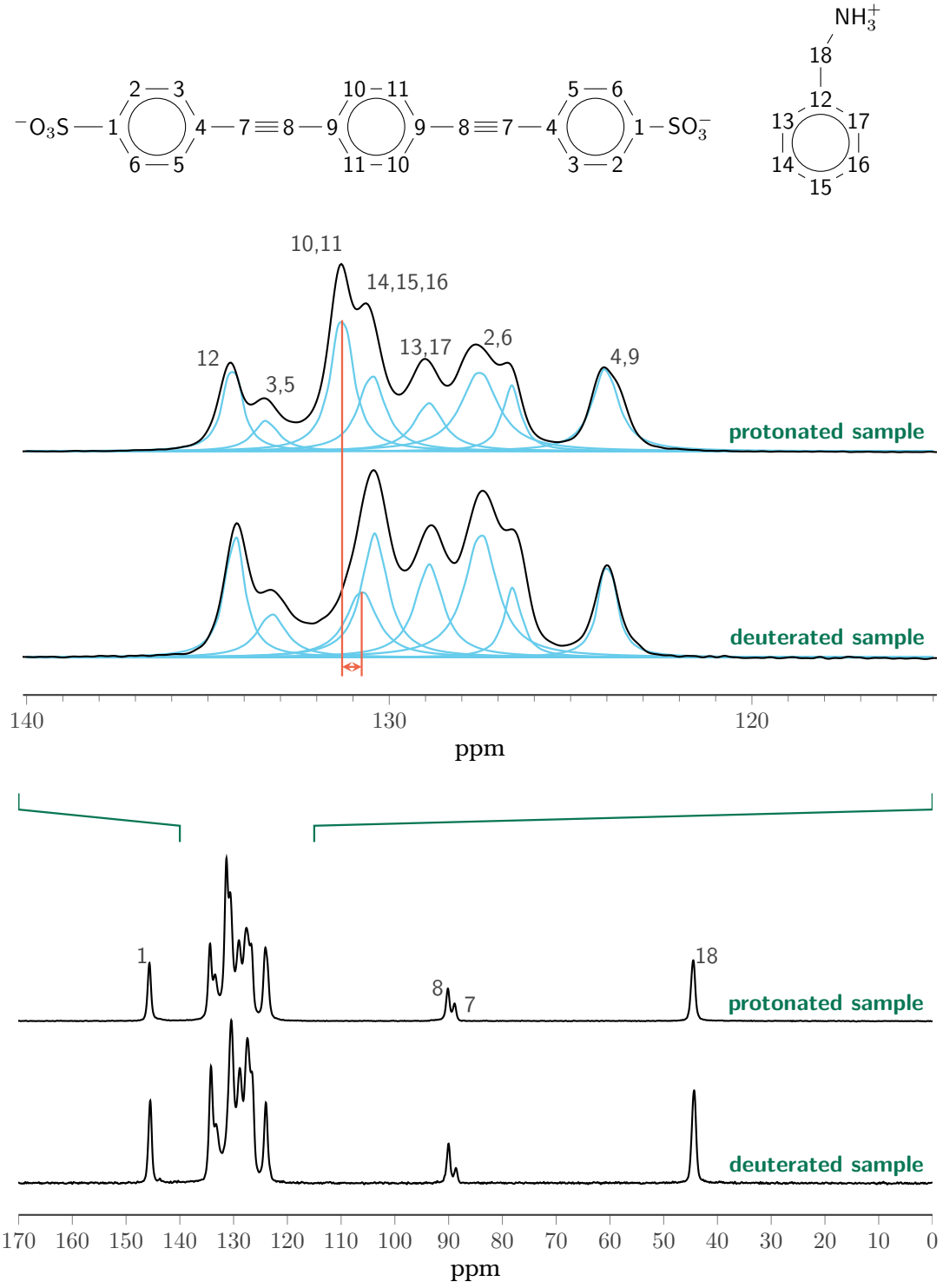

Figure 6.4: ^{13}C CP MAS NMR spectra of the compounds with contact time of 2 ms. It is possible to notice how deuteration affects the chemical shifts of the rotor (carbon 10 and 11).

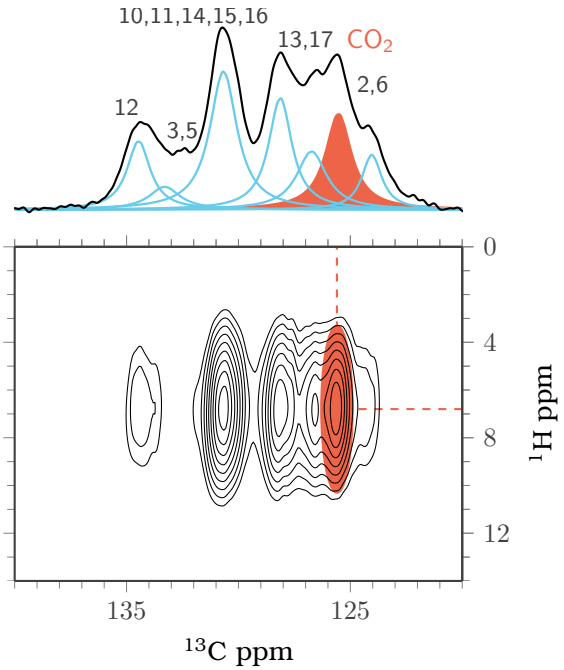

Figure 6.5: 2D ^{1}H-^{13}C hetero correlated NMR spectrum of CO_2 loaded compound at 220 K with a contact time of 5 ms.

correlated experiment (Fig. 6.5) was performed at 220 K to better understand the position of CO_2 within the channel. The NMR spectrum results in a clear signal for the gas; although depleted of ^{1}H, CO_2 can receive magnetization from the aromatic hydrogens of the host through nuclear dipolar interactions and under cross-polarization conditions, producing a correlation signal.[12–18] The signal intensity decays rapidly with internuclear distance ($\propto r^{-6}$) and requires relatively long residence times of the gas molecule on the site. Specifically, the notable intensity of the CO_2 cross-peak demonstrates the occurrence of internuclear distances shorter than 4 Å. 2D heteronuclear NMR correlations and cross-polarization from a solid to a gaseous molecule are rare,[19] providing clear evidence of gas associated with interaction sites.

Furthermore, the location of CO_2 molecules along the channels could be determined by GCMC simulation and by synchrotron radiation XRD experiments on single-crystals sealed at 20 bar. The

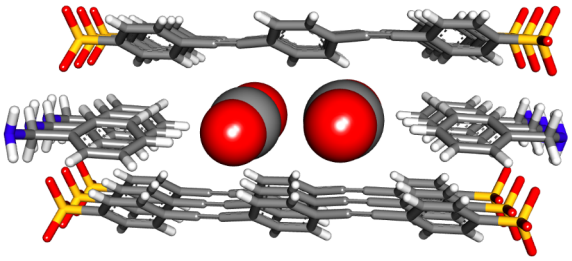

Figure 6.6: Location of CO_2 molecules diffused into the channel. CO_2 molecules are depicted by a space-filling model.

channel architecture was retained with respect to the empty structure and the distance of the adjacent rod-like molecules remained unaltered (Fig. 6.6). Two CO_2 molecules are located per host: they are aligned parallel to the channel axis and arranged in close association with the rod-like struts, which bear the rotors, in agreement with NMR results. In particular, CO_2 molecules lie in close proximity to the alkyne groups and one of their oxygen atoms points toward the CH group of the rotor, likely stabilizing this configuration as the ground state.

^{2}H spin-echo Spectra

The molecular rotor was analysed with ^{2}H solid state NMR using quadrupolar spin-echo pulse sequence from 155 K to 290 K. The sample was insert in a glass vial and flame sealed under vacuum to prevent gas adsorption. The line shape analysis indicates a mechanism of motion consistent with a rapid two-site 180° flip reorientation of *p*-phenylene moieties about their *para*-axis (Fig. 6.7).

At high temperatures (> 250 K) the linewidth restriction is evident together with the weakening of the spectral shoulders, demonstrating that the rapid libration of the rotor must be included. The horns of the Pake doublet are at a distance of 130 kHz for the static spectra and decreases to 27.5 kHz in the fast motion regime.

Moreover, as the rotors are easily accessible by the gas phase, CO_2 can effectively regulate the rotor dynamics.

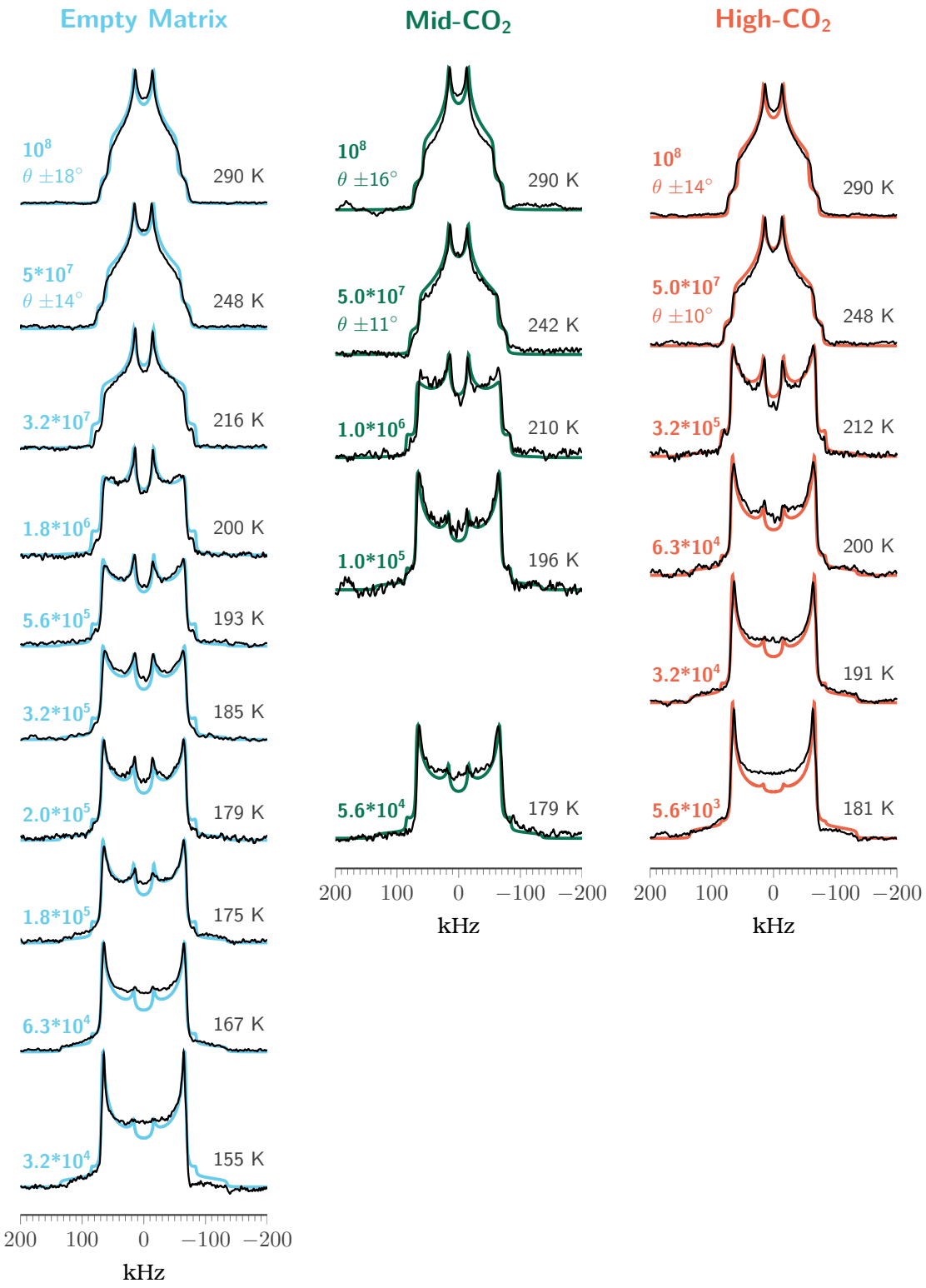

Figure 6.7: Experimental ^{2}H spin-echo NMR spectra as function of temperature of the empty material, the compound loaded with CO_2 at 3.3 bar and 5.4 bar. Profiles were simulated considering a two-site 180° flip mechanism (**light blue**, **green** and **orange**). θ corresponds to the libration semi-amplitude; the reorientation rates in hertz are also reported.

Thus, the crystalline powders were sealed under pressurized CO_2 at 3.3 bar and 5.4 bar at room temperature (denoted mid-CO_2 and high-CO_2, respectively). The crystal structure of the matrix after CO_2 loading at these pressures does not change, as shown by X-ray diffraction and ^{13}C CP MAS NMR at room and low temperatures.

^2H NMR spectra of CO_2-loaded samples show that, at the same temperature, the motion frequency is inversely proportional to the gas pressure. Adsorption extrapolation from the experimental data shows a constant loading of 1.8 CO_2 per rotor for the high-CO_2 sample below 212 K (the mid-CO_2 sample is constant at 1.7 below 210 K). This ensures that the role played by the guest does not change.

Energy evaluation by the Arrhenius plot (Fig. 6.8) gives an activation energy of 5.7 kcal/mol for the empty material and 7.0 kcal/mol for the sample with high CO_2 loading. This increased energy is probably due to the rotor-guest interaction leading to a more favourable ground state. Grand Canonical Monte Carlo simulations support this theory, while the steric hindrance generated by CO_2 appears to have a minor effect because favourable interactions with ethynyl units keep CO_2 at the side of the rotor.[20] Treatment of the crystals under vacuum resulted in the reverse phenomenon, and the regaining of pristine fast rotor-dynamics.

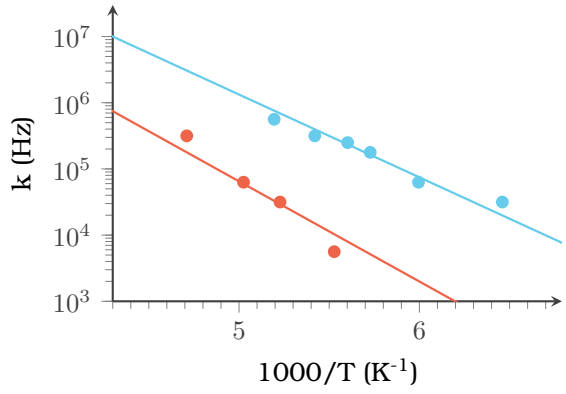

Figure 6.8: Arrhenius plots of the simulated ^2H spectra of the empty sample (light blue) and loaded at 5.4 bar (orange).

In these experiments we were able to manipulate the rotor dynamics from the gas phase by exposing the material to CO_2. The molecules diffuse easily into the crystalline channels and interact individually with the rotors, increasing by 1.3 kcal/mol the activation energy for rotation and putting the brakes on the dynamics in the crystal. Moreover, this study demonstrated the dependence of the phenomenon on pressure.

6.2 Ultrafast Molecular Rotors in a Metal Organic Framework

After the proof of concept that the rotational frequency of a rotor can be a function of the guest loading, a new complex system was studied. The material of interest is a zinc MOF with the potential of a fast rotor dynamic. More interestingly, the framework contains pores that allow the generation of complex CO_2-rotor interactions.[21] Another important aspect is the presence of only two hydrogen species, allowing a clear measure of the relaxation times and estimate the activation energy of the rotation with the Kubo-Tomita equation.[22]

Crystal Structure

The porous and absorptive architecture was realized through the robustness of metal-organic bonds and the use of rigid molecular rods bearing the rotors. We selected a suitable rod-like strut that contains a central *p*-phenylene unit (the rotor) connected through ethynyl groups to two pyrazole moieties 1,4-bis(1*H*-pyrazol-4-ylethynyl)benzene (BPEB) which interact with Zn(II) ions to fabricate the microporous MOF Zn-BPEB (Fig. 6.9).[21] The isostructural MOF d_4-Zn-BPEB selectively deuterated on the central *p*-phenylene moiety was prepared to

investigate the rotor dynamics.

The crystal structure of Zn-BPEB features 1D square channels with 10 x 10 $Å^2$ cross section and small pores with aperture of 4.3 Å diameter connecting the large channels, accounting, respectively, for an empty volume of 1356 $Å^3$ and 696 $Å^3$ per unit cell, (calculated through an exploring sphere of 1.2 Å radius and the contact surface model). Each *p*-phenylene unit, which constitutes the mobile element capable of rotating, is exposed to both channels. The tetrahedral metal node plays a key role in the separation of the rod-like ligands, providing the molecular rotor with enough room to rotate. The robustness of the MOF structure is guaranteed by the coordination of pyrazolate rings at the end of the rods with metal node (Zn^{+2}).

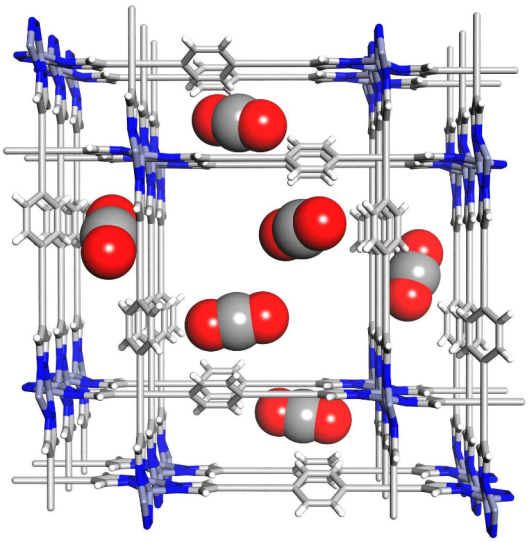

Figure 6.9: Zn-BPEB showing CO_2 molecules diffusing in both small and large cavities

Structure analysis reveals that the minimum distance between adjacent axes of central *p*-phenylene rings is 7.3 Å along the *c*-axis. On the other hand, being an interpenetrated network, in the *ab* plane each *p*-phenylene ring faces both the ethynyl and the pyrazolate groups of the adjacent linker. The pyrazolate plane is at a distance of 5.2 Å and does not interfere with the rotor. Such a relatively large distance allows for the rotation of the *p*-phenylene ring and, considering the low rotation barrier about Csp_2-Csp bonds (as the *p*-phenylene-ethynyl bond), the *p*-phenylene moieties are expected to be efficient as fast molecular rotors.

Adsorption

The porosity of the system was confirmed by the adsorption isotherm of N_2 at 77 K, revealing a structure with surface areas of 1366 m^2/g (Langmuir) and 1214 m^2/g (BET).

CO_2 adsorption isotherms (Fig. 6.10) show a Langmuir profile, with an uptake of 200 cm^3/g at p/p^0 = 1 at 195 K. Isotherms at 273 K and 298 K reach at 10 bar the 80% and 56% filling respectively. The isosteric heat of adsorption is 25 kJ/mol at low coverage, indicating a good interaction between CO_2 and the channel walls.

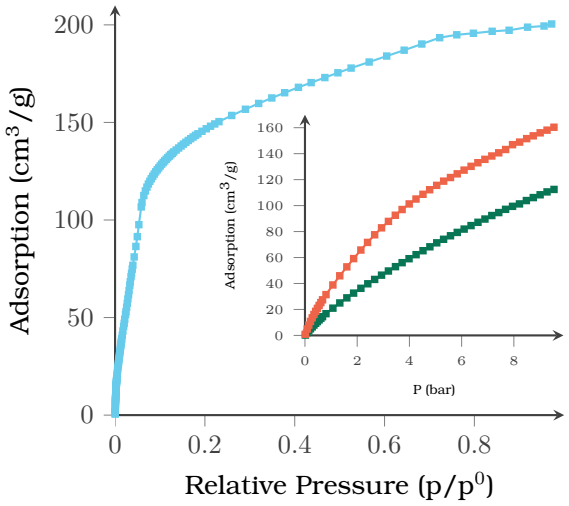

Figure 6.10: CO_2 isotherms of d_4-Zn-BPEB at 195 K (light blue), 273 K (orange) and 298 K (green).

Gran Canonical Monte Carlo simulations at 298 K show that the preferential CO_2 adsorption site is located in the small pores while the main channel is loaded only at higher pressure (Fig. 6.11).

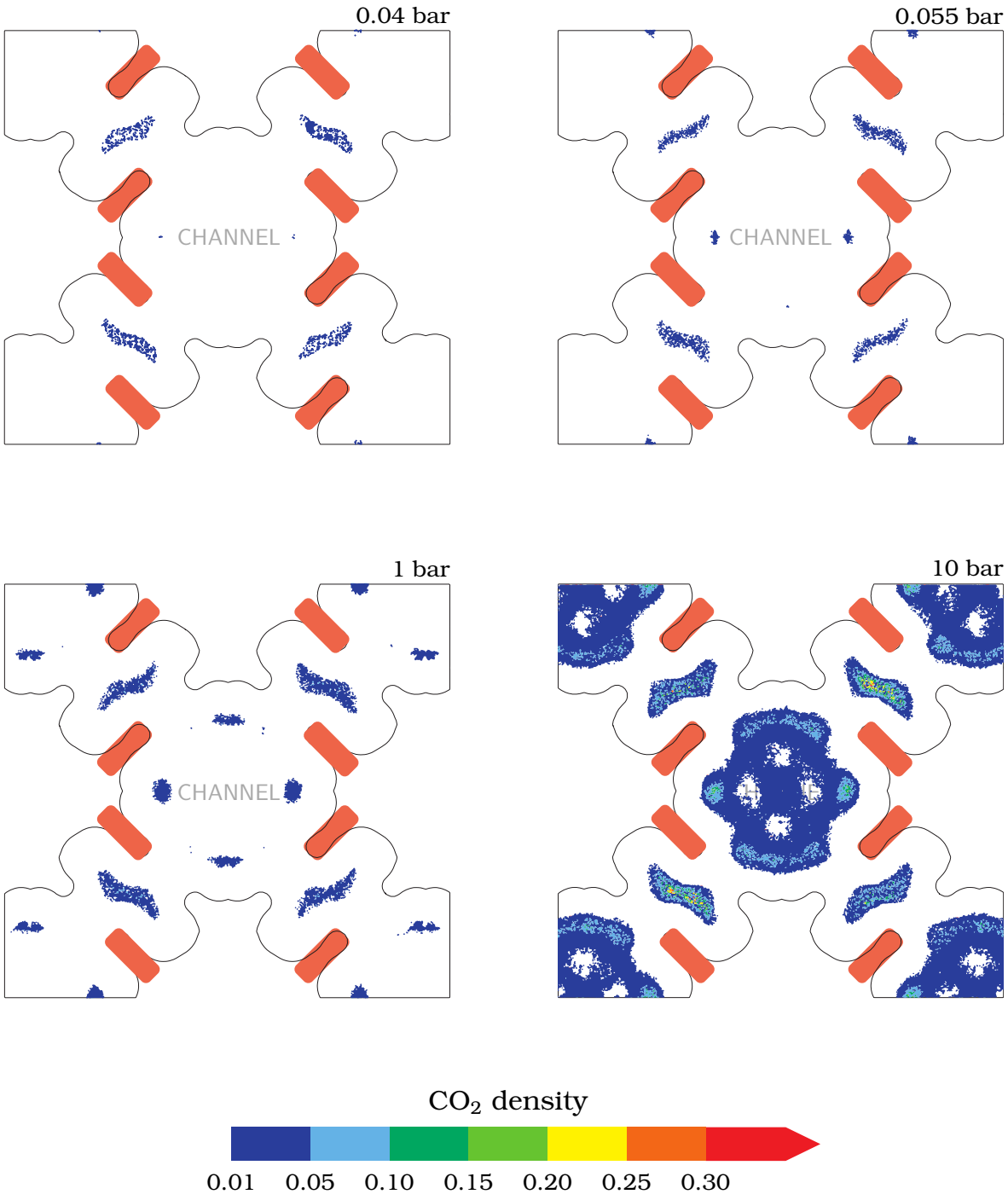

Figure 6.11: Distribution of centers of mass of the CO_2 molecules inside the framework of Zn-BPEB from the GCMC simulations of CO_2 adsorption at 298 K, as viewed perpendicular to the c-axis. It is clearly visible how the gas molecule prefer to occupy small pores, in fact they are the first to be filled and at high pressure the density is higher with respect to that in the channel. The rotors are highlighted in **orange**.

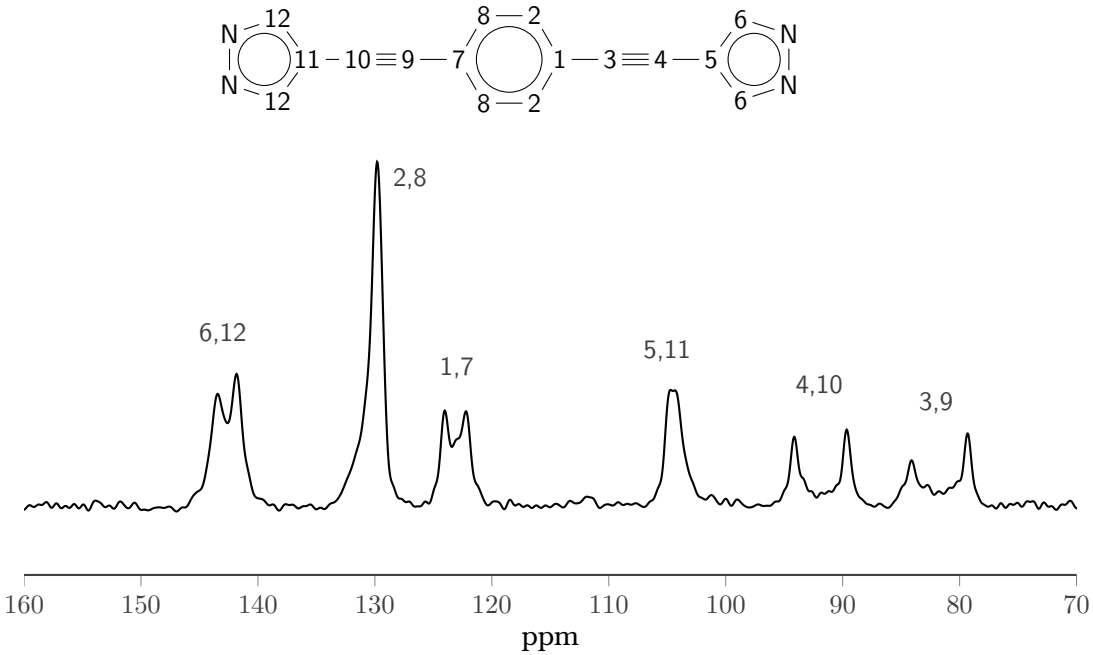

Figure 6.12: ^{13}C MAS NMR spectra of d_4-Zn-BPEB recorded with a recycle delay of 20 s.

NMR Spectroscopy

The ^{13}C MAS NMR spectrum of the deuterated sample is similar to that of protonated MOF, with a small shift for carbon 2 and 8 due to isotopic effect of deuterium (Fig. 6.12).

The sample was loaded with ^{13}C enriched-CO_2 at ambient pressure. ^{13}C NMR spectra show two different peaks at 125.1 and 125.7 ppm for the adsorbed and free CO_2 respectively, allowing the quantification of the amount of adsorbed gas (Fig. 6.13). Lowering the temperature increases the total adsorbed fraction.

^{2}H spin-echo Spectra

We perform the ^{2}H NMR analysis to demonstrate the dynamics of the molecular rotor (Fig. 6.14). The sample was flame sealed in a glass vial under vacuum and in a vial with CO_2 at 9 bar (at room temperature). The study was performed between 150 K and 290 K.

The empty sample shows a line shape compatible with a two-site 180° flip reorientation around the main axis of *p*-phenylene moieties. The reorientation

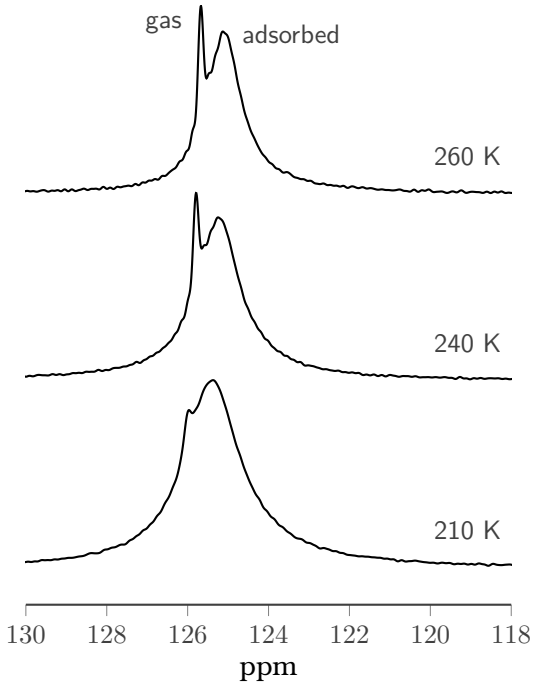

Figure 6.13: ^{13}C MAS collected on Zn-BPEB loaded with ^{13}C enriched-CO_2. It is possible to distinguish the signal of the gas phase (125.7 ppm) from the CO_2 in the pores (125.1 ppm). A recycle delay of 10 s was applied for collecting selectively CO_2 signals.

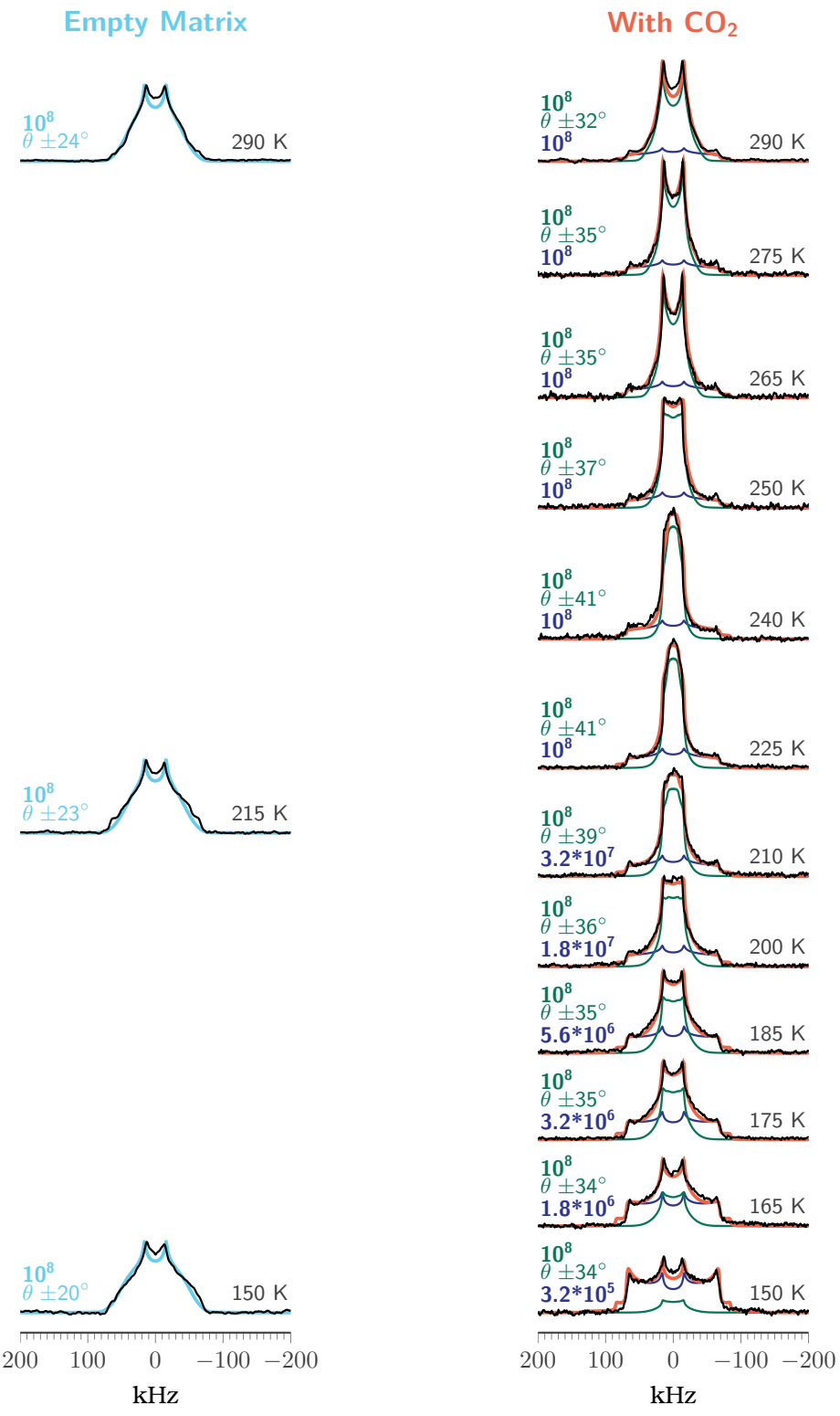

Figure 6.14: Experimental ^{2}H spin-echo NMR spectra of d_4-Zn-BPEB as function of temperature of the empty material and of the compound loaded with CO_2 at 9 bar. Profiles were simulated considering a two-site 180° flip mechanism (**light blue** and **orange**), distinguishing the fast (**green**) and slow (**blue**) components for the loaded series. θ corresponds to the libration semi-amplitude; the reorientation rates in hertz are also reported.

is extremely fast (> 10^8 Hz) with wide librations. Note that the spectra do not exhibit substantial changes in the entire temperature range.

CO_2 drastically changes the line shape but the motion is not as different. The spectra were simulated considering two distinct components: a fast rotation with strong librations and a slower rotation. Both are interpreted by a two-site 180° flip reorientation mechanism. The slow component is predominant at low temperature while the fast is at 290 K.

The total simulation can be explained with two possible loading configurations, which generate different rotor-gas interactions. The amount of adsorbed CO_2 increases at low temperature so the slow component (predominant at 150 K) must be due to the high number of gas molecules around the rotor.

As already stated, CO_2 preferentially fills the small pores with respect to the main channel. It is possible to define two configurations of the system (Fig. 6.15) one at low CO_2 loading (2 gas molecules around each rotor) and one at high loading (3 gas molecules per rotor). In the former, the two CO_2 molecules are not able to considerably increase the activation energy of the motion, but they increase the librations. In the latter, CO_2 molecules wrap the rotor and slow down its motion. Arrhenius plot of this configuration gives an activation energy of 4.5 kcal/mol, 4.0 kcal/mol more than the empty matrix, demonstrating how CO_2 can manipulate rotor dynamics.

^{1}H T_1 Relaxation

Deuterim NMR specra do not show any variation with temperature because the motion is always above the limit of ^{2}H NMR (10^8 Hz); we decided to perform a measurement of the activation energy of the empty non deuterated matrix using the ^{1}H NMR relaxation times (Fig. 6.16). The resulting activation energy is 0.5 kcal/mol.

When it was published, this was the lowest activation energy achieved for a molecular rotor.

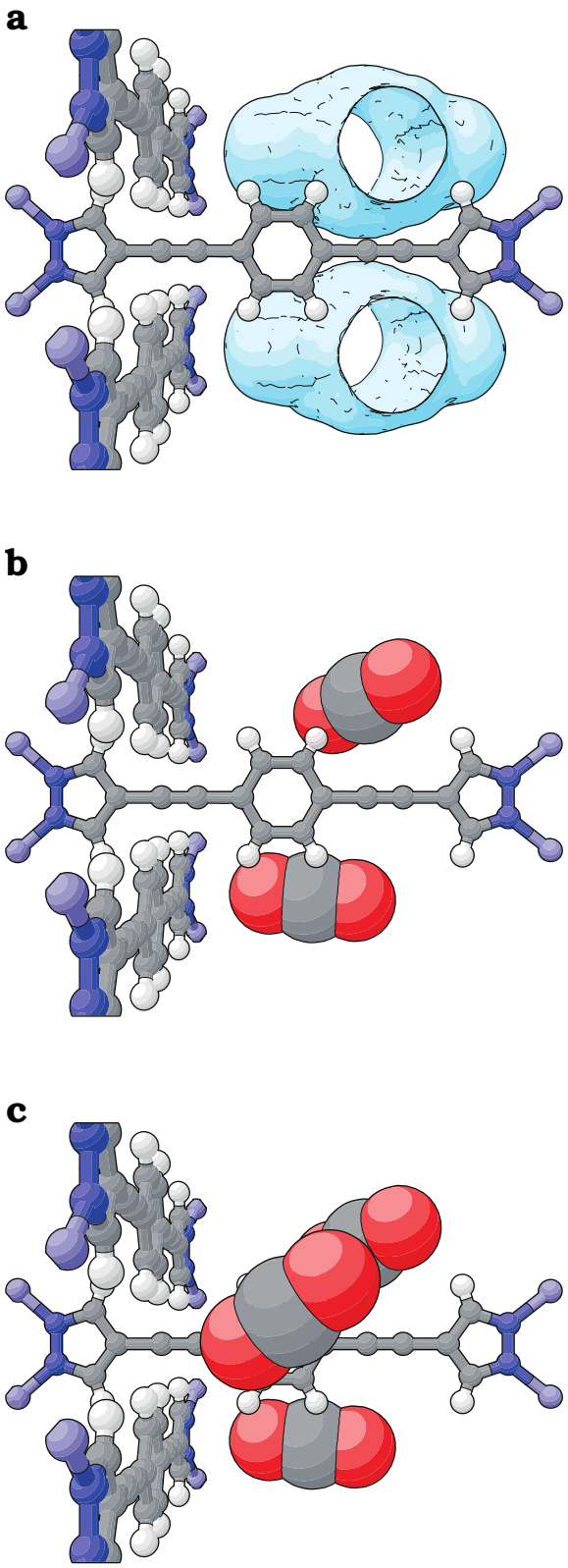

Figure 6.15: Front view of a rotor from the channel. **a** The empty system with the small pores position. **b** Exploration of the cavities by CO_2 at low loading. **c** Exploration of the cavities by CO_2 at high loading.

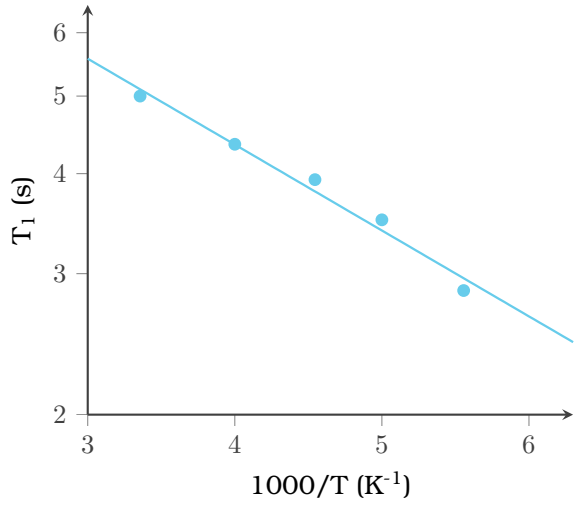

Figure 6.16: ^{1}H T_1 relaxation times for the empty Zn-BPEB.

This challenging project of having realized dynamics in crystals as fast as in liquids opens new perspectives such as the control of molecular dynamics by the influence of mild chemical stimuli, that is, gas loading. The rapid reorientation of mobile elements in crystals enables the activation of switchable ferroelectric properties that can be used in opto-electronic devices. This unique response of the materials to CO_2 is of great importance for the environment, enlarging perspectives in the field of sensors and gas detection.

Bibliography

[1] Comotti, A.; Bracco, S.; Valsesia, P.; Beretta, M.; Sozzani, P. Fast molecular rotor dynamics modulated by guest inclusion in a highly organized nanoporous organosilica. *Angewandte Chemie International Edition* **2010**, *49*, 1760–1764.

[2] Comotti, A.; Bracco, S.; Ben, T.; Qiu, S.; Sozzani, P. Molecular rotors in porous organic frameworks. *Angewandte Chemie International Edition* **2014**, *53*, 1043–1047.

[3] Comotti, A.; Bracco, S.; Yamamoto, A.; Beretta, M.; Hirukawa, T.; Tohnai, N.; Miyata, M.; Sozzani, P. Engineering switchable rotors in molecular crystals with open porosity. *Journal of the American Chemical Society* **2014**, *136*, 618–621.

[4] Comotti, A.; Bracco, S.; Sozzani, P. Molecular rotors built in porous materials. *Accounts of Chemical Research* **2016**, *49*, 1701–1710.

[5] Chen, L.; Cao, F.; Sun, H. Ab initiostudy of the Π-Π interactions between CO_2 and benzene, pyridine, and pyrrole. *International Journal of Quantum Chemistry* **2013**, *113*, 2261–2266.

[6] Bracco, S.; Miyano, T.; Negroni, M.; Bassanetti, I.; Marchio', L.; Sozzani, P.; Tohnai, N.; Comotti, A. CO_2 regulates molecular rotor dynamics in porous materials. *Chemical Communications* **2017**, *53*, 7776–7779.

[7] Breck, D. *Zeolite Molecular Sieves: structure, chemistry, and use*; Wiley-Interscience Publication; Wiley, 1973.

[8] Choudhary, V. R.; Mayadevi, S. Adsorption of methane, ethane, ethylene, and carbon dioxide on silicalite-I. *Zeolites* **1996**, *17*, 501–507.

[9] Comotti, A.; Bracco, S.; Distefano, G.; Sozzani, P. Methane, carbon dioxide and hydrogen storage in nanoporous dipeptide-based materials. *Chem. Commun.* **2009**, 284–286.

[10] Comotti, A.; Fraccarollo, A.; Bracco, S.; Beretta, M.; Distefano, G.; Cossi, M.; Marchese, L.; Riccardi, C.; Sozzani, P. Porous dipeptide crystals as selective CO_2 adsorbents: experimental isotherms vs. grand canonical Monte Carlo simulations and MAS NMR spectroscopy. *CrystEngComm* **2013**, *15*, 1503–1507.

[11] Sumida, K.; Rogow, D. L.; Mason, J. A.; McDonald, T. M.; Bloch, E. D.; Herm, Z. R.; Bae, T.-H.; Long, J. R. Carbon dioxide capture in metal-organic frameworks. *Chemical Reviews* **2011**, *112*, 724–781.

[12] Vega, A. J. Heteronuclear chemical-shift correlations of silanol groups studied by two-dimensional cross-polarization magic angle spinning NMR. *Journal of the American Chemical Society* **1988**, *110*, 1049–1054.

[13] Kitao, T.; Bracco, S.; Comotti, A.; Sozzani, P.; Naito, M.; Seki, S.; Uemura, T.; Kitagawa, S. Confinement of single polysilane chains in coordination nanospaces. *Journal of the American Chemical Society* **2015**, *137*, 5231–5238.

[14] Sozzani, P.; Bracco, S.; Comotti, A.; Simonutti, R.; Camurati, I. Stoichiometric compounds of magnesium dichloride with ethanol for the supported Ziegler-Natta catalysis: first recognition and multidimensional MAS NMR Study. *Journal of the American Chemical Society* **2003**, *125*, 12881–12893.

[15] Ladizhansky, V.; Vega, S. A method for measuring heteronuclear (^1H-^{13}C) distances in high speed MAS NMR. *Journal of the American Chemical Society* **2000**, *122*, 3465–3472.

[16] Bracco, S.; Comotti, A.; Ferretti, L.; Sozzani, P. Supramolecular aggregation of block copolymers in the solid state as assisted by the selective formation of inclusion crystals. *Journal of the American Chemical Society* **2011**, *133*, 8982–8994.

[17] Sozzani, P.; Comotti, A.; Bracco, S.; Simonutti, R. A family of supramolecular frameworks of polyconjugated molecules hosted in aromatic nanochannels. *Angewandte Chemie International Edition* **2004**, *43*, 2792–2797.

[18] Comotti, A.; Bracco, S.; Sozzani, P.; Hawxwell, S. M.; Hu, C.; Ward, M. D. Guest molecules confined in amphipathic crystals as revealed by X-ray diffraction and MAS NMR. *Crystal Growth & Design* **2009**, *9*, 2999–3002.

[19] Bassanetti, I.; Comotti, A.; Sozzani, P.; Bracco, S.; Calestani, G.; Mezzadri, F.; Marchiò, L. Porous molecular crystals by macrocyclic coordination supramolecules. *Journal of the American Chemical Society* **2014**, *136*, 14883–14895.

[20] Winston, E. B.; Lowell, P. J.; Vacek, J.; Chocholoušová, J.; Michl, J.; Price, J. C. Dipolar molecular rotors in the metal-organic framework crystal IRMOF-2. *Physical Chemistry Chemical Physics* **2008**, *10*, 5188.

[21] Galli, S.; Maspero, A.; Giacobbe, C.; Palmisano, G.; Nardo, L.; Comotti, A.; Bassanetti, I.; Sozzani, P.; Masciocchi, N. When long bis(pyrazolates) meet late transition metals: structure, stability and adsorption of metal–organic frameworks featuring large parallel channels. *Journal of Materials Chemistry A* **2014**, *2*, 12208.

[22] Bracco, S.; Castiglioni, F.; Comotti, A.; Galli, S.; Negroni, M.; Maspero, A.; Sozzani, P. Ultrafast molecular rotors and their CO_2 tuning in MOFs with rod-like ligands. *Chemistry - A European Journal* **2017**, *23*, 11210–11215.

7. Gas Dynamic in the Solid State by NMR

Summary

Understanding the motion of guest molecules in a porous material is mandatory for complete comprehension of the interactions between rotor and gases.

In porous materials, gases are in a more confined environment reducing their degrees of freedom.[1] Usually the diffusion occurs in a quasi random manner,[2] but the regularity of size and shape of pores in crystalline porous materials can induce a peculiar pathway and mechanism of diffusion. We will show the role played by the size and shape of pores and the specific interactions between the host and diffusing-in gases. Due to its incredible sensitivity, NMR has the potential to reveal the gas dynamics in a solid and its diffusion mechanism. The experimental results were compared to computational study.

7.1 Xe Diffusion

The limited free volume available provided by a porous material to diffusing-in gases generates peculiar diffusional mechanisms, from three dimensional to mono-dimensional diffusion (or single file diffusion) in 1D channels and modulates the gas dynamics. Xe gas shows a wide electron density and is sensitive to the explored environment[3,4] and its NMR chemical shift is extremely sensitive to the size and shape of explored cavity.

Regarding the pores, a new material was synthesized from methanetetrabenzoic acid (MTB, Fig. 7.1). Its crystalline structure (TCF-1) shows a series of parallel channels large enough to accommodate Xe atoms and well-defined adsorption sites.

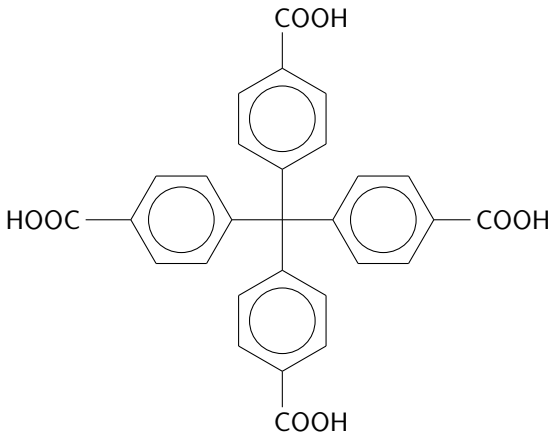

Figure 7.1: Methanetetrabenzoic acid.

Crystal Structure

The self-assembly of MTB molecules leads to a tetracarboxylic framework TCF-1, held together by hydrogen bonds between carboxyl groups. In particular, hydrogen bond dimers between carboxylic groups sustain the robust material that is endowed with high flexibility. Due to the peculiar tetrahedral shape of the molecules a 6-fold interpenetrating diamond array occurs. Despite the tendency of diamond arrays towards interpenetrating networks, there is only one other case of a system presenting six of them.[5] Each network is associated with the next by close contact interactions between the positively-charged carboxylic carbon and the *p*-phenyl groups (distance of 3.6 Å), further stabilizing the structure. The crystal structure exhibits a series of parallel channel (Fig. 7.2) with well-defined adsorption sites and an elliptical cross-section of 5.5 x 2.9 $Å^2$; interestingly it can expand to 6.4 x 4.2 $Å^2$ in the presence of xenon.

The crystal structure of empty sample and sample loaded with Xe were solved from single crystal X-ray diffraction. An important feature is the rotation by 90° of

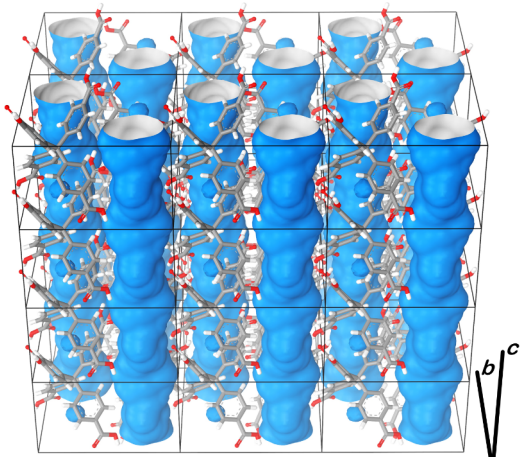

Figure 7.2: Crystal structure of the porous TCF-1 highlighting the empty channels as viewed perpendicular to the *c*-axis.

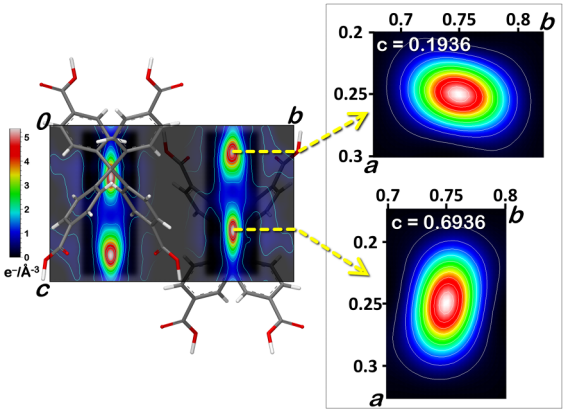

Figure 7.4: Electron density difference map (F_0-F_C) for Xe loaded TCF-1 as viewed perpendicular to and along the *c*-axis.

the ellipse main axis between adjacent sites along the *c*-axis (Fig. 7.3). The electron density maps clearly show the localization of xenon in the adsorption sites (Fig. 7.4).

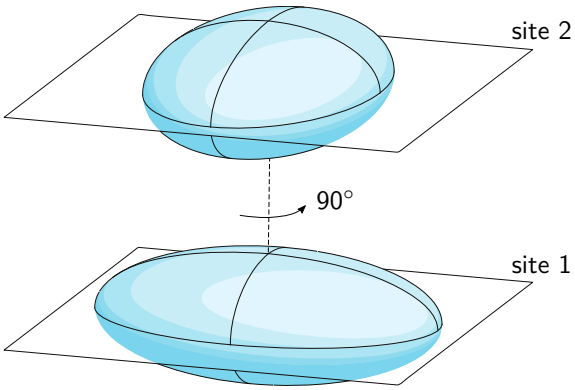

Figure 7.3: Schematic representation of Xe jumps between two sites and the orientation of the elliptical cross-section in two adjacent cavities.

Gas Adsorption

The permanent porosity of the TCF-1 was demonstrated by the CO_2 isotherm at 195 K (Fig. 7.5), which shows a Langmuir type profile typical of a microporous structure. The porous TCF-1 can adsorb 96.8 cm^3/g (4.3 mmol/g, i.e. 19.0 wt%), exceeding a number of materials based on stronger bonds, such as SNU-15: a Co^{2+} MOF,[6] which is constructed with the same tetrahedral building block (MTB^{4-})through coordination bonds. CO_2 adsorption isotherms collected up to 10 bar at 298 K and 273 K reach 72.3 and 76.6 cm^3/g (STP), respectively.

It is worth noticing that under the mild conditions of 1 bar and 273 K, TCF-1 adsorbs 40 cm^3/g of CO_2 (1.76 mmol/g and 7.7 wt%), overcoming a few prominent porous molecular and metal-organic frameworks[7,8] and many covalent based materials, in particular, COF-102[9] and PAF-1,[10–12] although their surface areas are markedly higher, giving credit to the fact that crystals with narrow channels are performant absorbers at low pressures.

The isosteric heat of adsorption calculated from CO_2 adsorption isotherms at distinct temperatures is 33 kJ/mol. This comparatively high value suggests multiple interactions installed simultaneously by the CO_2 molecule in the narrow channel.[13–16] In contrast, N_2 adsorption is negligible, this is probably because the pores in the empty structure are too narrow and the low affinity does not allow the opening up of the channels, therefore the CO_2/N_2 selectivity is not higher than a few hundred at 273 K.

A particular feature of the porous TCF-1 is its ability to adsorb methane and hexane. The isosteric heat of CH_4 adsorption, as calculated from the adsorption isotherms at distinct temperatures, is 21 kJ/mol, this

value is higher than most MOFs[17] thanks to the narrow cross section of the channel that enables multiple interactions with walls.

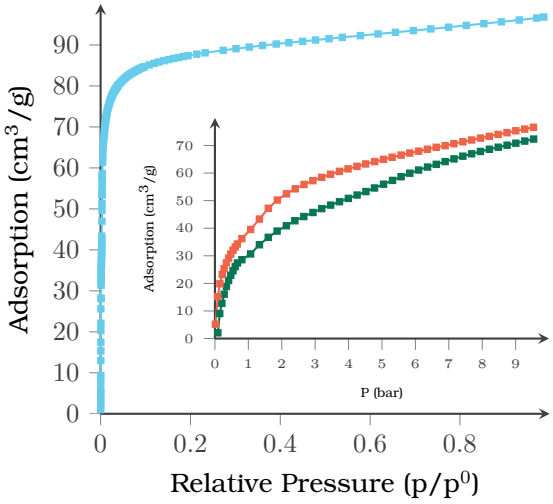

Figure 7.5: CO_2 isotherms of TCF-1 at 195 K (light blue), 273 K (orange) and 298 K (green).

NMR Spectroscopy

The flexibility of the crystal structure is shown by high temperature thermal treatment (>100 °C) that initiates the phase transformation to a close-packed structure, with longer and weaker hydrogen bonds. It is possible to restore the porous architecture with THF/hexane adsorption at room temperature.

It is possible to distinguish the porous structure from the close-packed with NMR, both from ^{1}H and ^{13}C spectra (Fig. 7.6 and 7.7). It is possible to distinguish the porous structure from the close-packed with NMR, both from ^{1}H and ^{13}C spectra (Fig. 7.6 and 7.7). Both spectra presents a downfield for the porous TCF-1, compatble with a shorter distance between carboxylic units. The universal calibration of ^{1}H chemical shift vs oxygen distances of carboxylic acid dimers yields a distance of 2.7 Å for the porous structure and 3.2 Å for the close-packed.

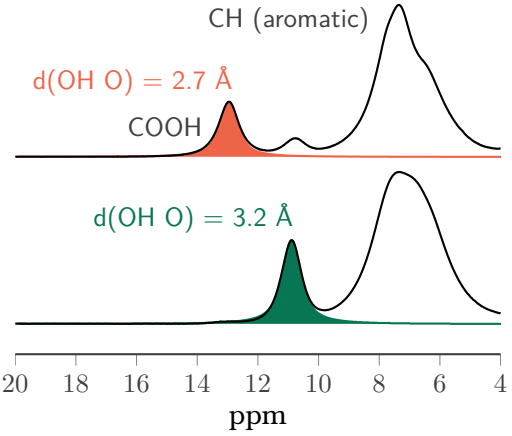

Figure 7.6: ^{1}H MAS (30 kHz) NMR spectra of porous (up) and close-packed (down) structures of TCF-1, the shift correspond to 2.2 ppm. The simulated profiles correspond to the carboxylic hydrogen resonances.

^{129}Xe NMR

The porous material was inserted in a glass vial and flame sealed with xenon gas at 9 bar at room temperature. ^{129}Xe NMR spectra acquired at variable temperatures show, in addition to the gas phase at 0 ppm, anisotropic signals in the 190-310 ppm range generated by Xe atoms confined to the accessible pores (Fig. 7.8). Such remarkable downfield of chemical shift values and the anisotropic pattern, achieved here under high Xe loading (>85%), indicate a tight fit in the host sites, as well as confining interactions with other Xe atoms that explore the channel.

The lineshape has remarkably changes with temperature. Although each adsorption site is equivalent (therefore they present the same tensors), adjacent sites are tilted by 90° along the channel. Xe atoms, undergoing their diffusion motion, feel this different orientation and the two tensor components get mixed. At low jump rate, xenon explores the cavity for more time giving the complete anisotropy while at high jump rate the gas perceived the channel as a cylinder.

Such model allows the complete simulation of the spectra, associating at

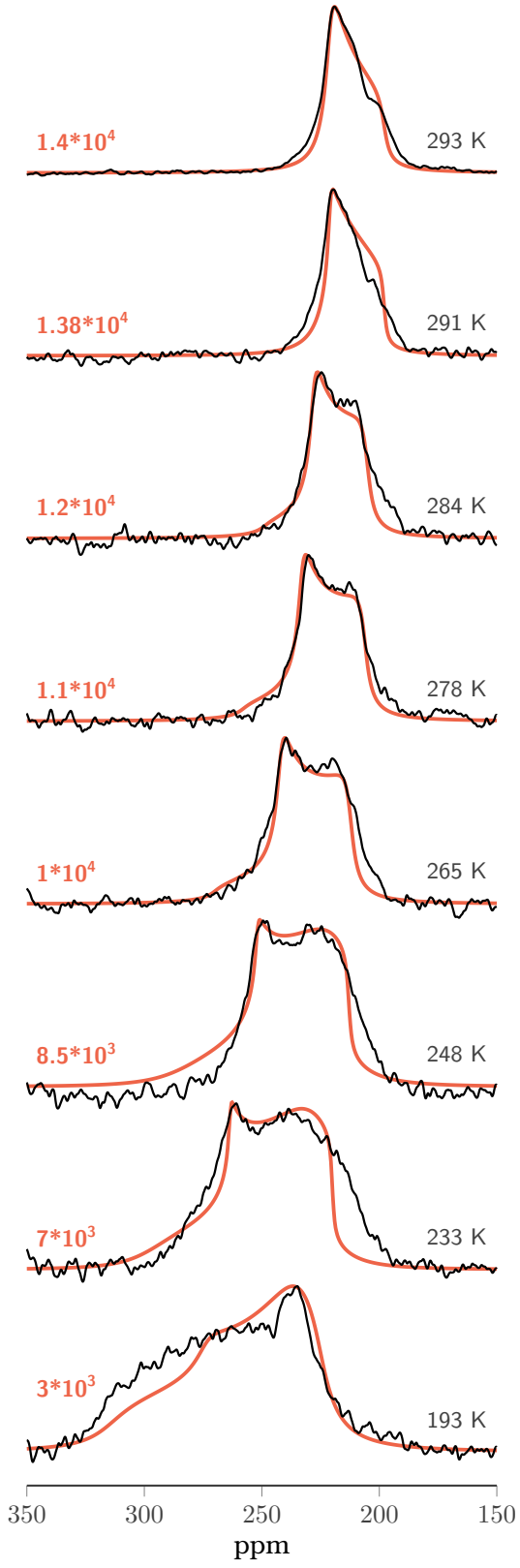

Figure 7.8: ^{129}Xe NMR spectra acquired at various temperatures, with simulations (orange). The reorientational rates in hertz are reported.

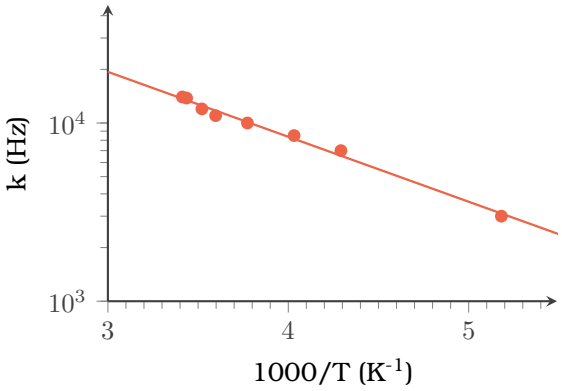

Figure 7.9: Arrhenius plots of the simulated ^{129}Xe spectra of TCF-1.

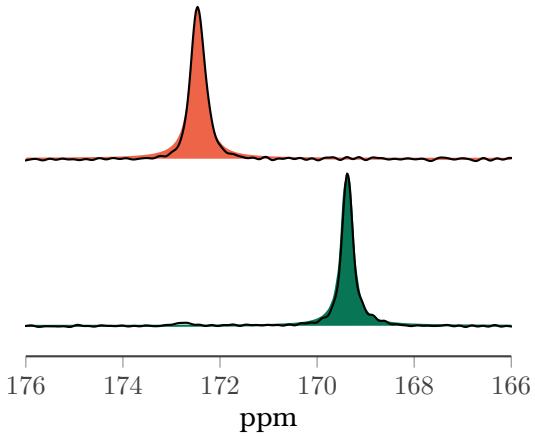

Figure 7.7: ^{13}C MAS NMR spectra of porous (up) and close-packed (down) TCF-1, the shift correspond to 3.0 ppm. The simulated profiles correspond to the carboxylic carbons.

each temperature a precise jump rate. The Arrhenius plot (Fig. 7.9) reveal an activation energy of 1.7 kcal/mol.

Simulations

To validate our model, we performed some *ab initio* calculations of the gas inside the pores. Xenon atoms have strong interactions between them and have the tendency to form long chains inside porous materials (clustering) even at low loading.[18] In this situation, the probability that a xenon atom has at least one free

space next to it seems quite low.

Considering the experimental occupation factor of 0.6 form XRD, ten adjacent sites were considered and filled with six xenon atoms. Of the 16 possible configurations, the chain one presents the lowest energy, while the arrangements in shorter Xe sequences are characterized by higher energies.

Applying the Boltzmann distribution at 220 K to the calculated energies, also taking into account their multiplicity, it is possible to notice that short Xe chains prevail over longer sequences. Focusing more on the single atom than on the chains, the probability that a single xenon has at least one free space next to it is above 50% (Fig. 7.10). The percentage increases with temperature.

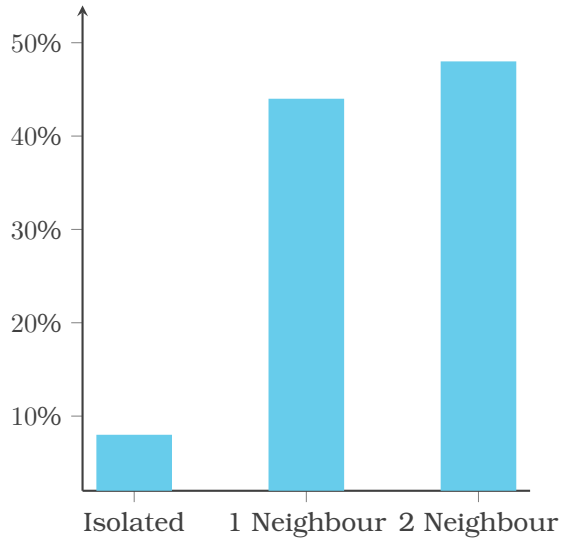

Figure 7.10: Representation of the probabilities calculated from the Boltzmann distribution at 220 K using the *ab initio* derived energies.

Another important simulation performed is the energy profile trajectory (Fig. 7.11). In this way it was possible to calculate the theoretical energy barrier for the jump between sites. The value obtained is 2.5 kcal/mol, that is close to the experimental result. Perhaps the resulting value is a bit higher because the simulation keeps rigid the host structure while the flexibility of the system is well documented. This more rigid system can be account for the slightly higher energy barrier.

This two combined analyses validate the experimental model we propose and give a more punctual perspective to xenon jumps. This fast motion is very interesting and underlines the sensitivity of Xe even to the smallest variation in the shape of the channel. It also necessary to emphasize how this porous structure comes from the crystallization of a relatively simple molecule such as MTB.

The simulations also highlight a big limit of NMR: the ability to see only the average situation of the system, but is completely blind to the behaviour of the single atom or molecule. Molecular simulations are able to overcame this limit and the experimental-theoretical joint characterization will become fundamental for the dynamic analysis in this thesis.

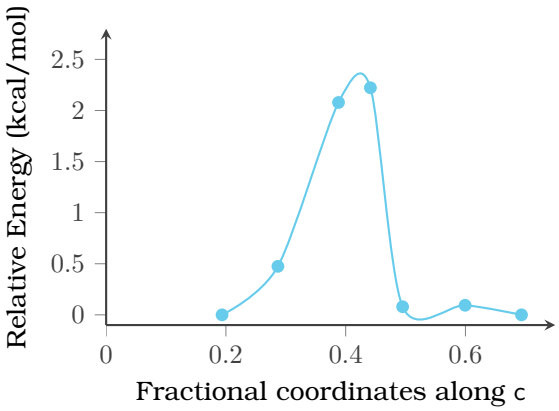

Figure 7.11: Energy profile for the trajectory of Xe from one cavity to the next by *ab initio* calculation applying the CASTEP transition state code.

7.2 CO_2 Diffusion

We have explored the role played by the intermolecular interactions for the capture and dynamics of CO_2 confined in porous architectures.

A novel material obtained from the crystallization of 4,4',4",4"'-methane tetrabenzenesulfonate (TBS) with 1,4-diamidiniumbenzene (DAB) (Fig. 7.13) offers an interesting environment to study the CO_2 behaviour in the presence of electrostatic interactions with the host walls. [19]

Crystal Structure

The material belongs to the family of organosulfonateamidinium salt (CPOS-5). The crystal is formed by tetrafunctional TBS and bifunctional DAB with a ratio of 1:2, held together by hydrogen bonds. The final structure has a series of parallel channels along *c*-axis with a cross-section of 6.8 x 5.3 Å^2.

Interestingly, the entire channel walls are made of the charges of TBS and DAB. To make the system even more intriguing, they form a double helix with two intertwined and alternatively charged ribbons (Fig. 7.14). This not only defines the adsorption sites, but also a path between them.

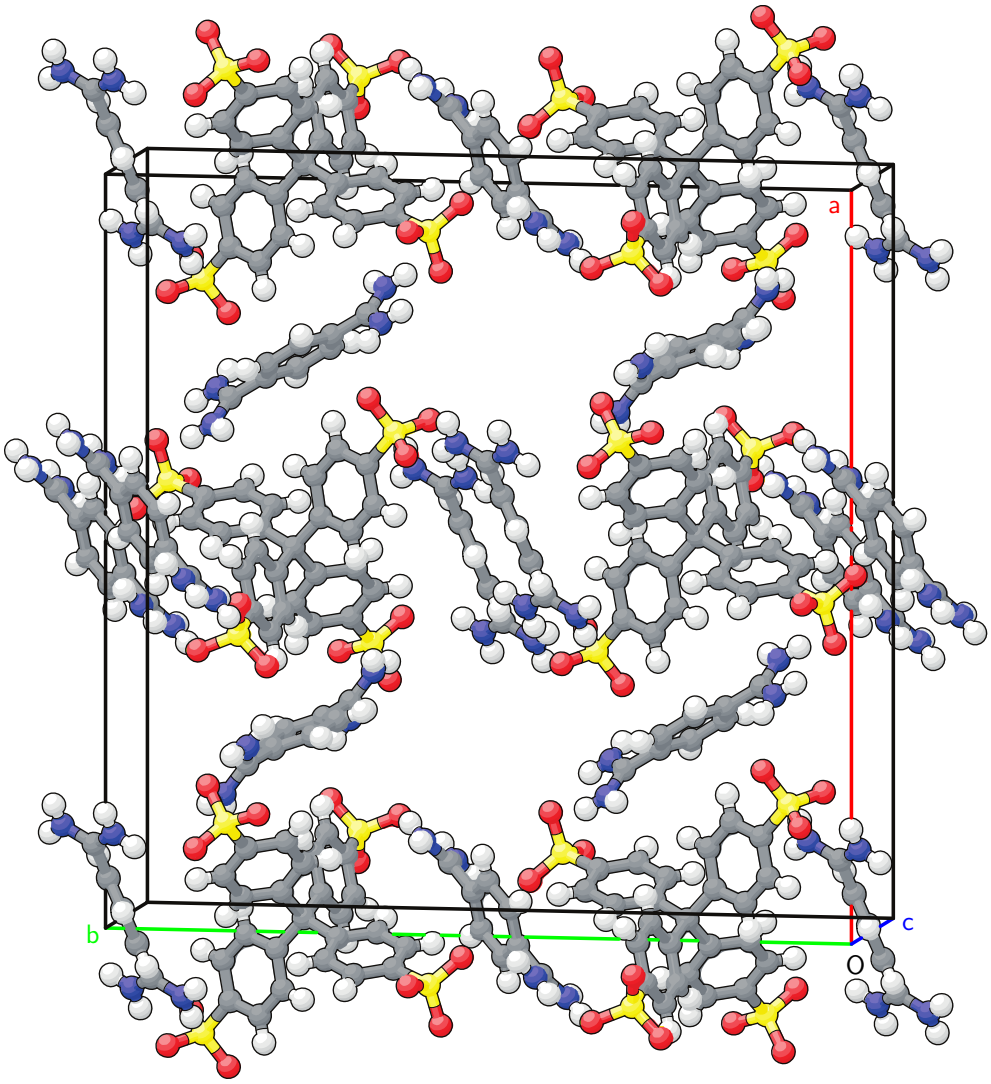

Figure 7.12: CPOS-5 crystal structure.

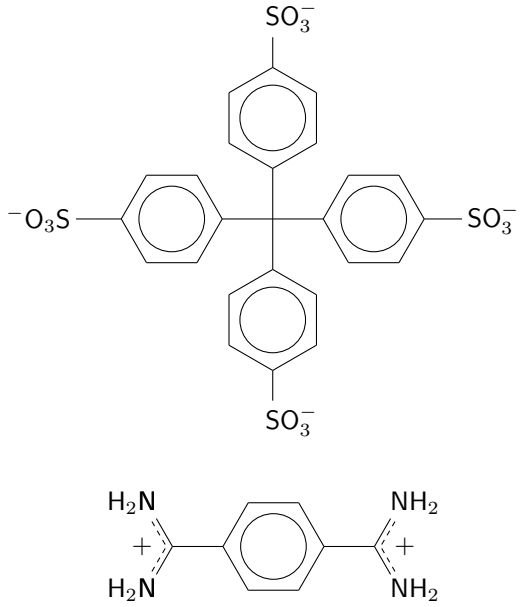

Figure 7.13: Schematic representation of anionic TBS and cationic DAB.

Gas Adsorption

The CO_2 adsorption isotherm shows an incredible uptake even at very low pressure (Fig. 7.15), suggesting an excellent affinity between the quadrupolar gas molecules with charge-decorated pore surfaces. 0.1 bar at room temperature are typical conditions of CO_2 in power plants. CPOS-5 is able to outperform many well well-known MOFs with greater surface areas such as HKUST-1, UMCM-150, MIL-47, IRMOF-3 and ZIF-8,[20] porous hydrogen-bonds and supramolecular organic frameworks such as SOF-1,[7] SOF-7,[21] HOF-3[22] and CB6[14] and its absorption value is comparable to that of the best performing HOF-5.[16]

The isosteric heat of adsorption calculated using van't Hoff is 34.5 kJ/mol, this value is in good agreement with the binding energy determined by DFT calculations (33.8 kJ/mol). This is considerably high and comparable to the other high-performance materials.

The tight fitting and the complementary electrostatic pattern of sub-nm channels is accounted for the exceptional CO_2/N_2 selectivity of 690.

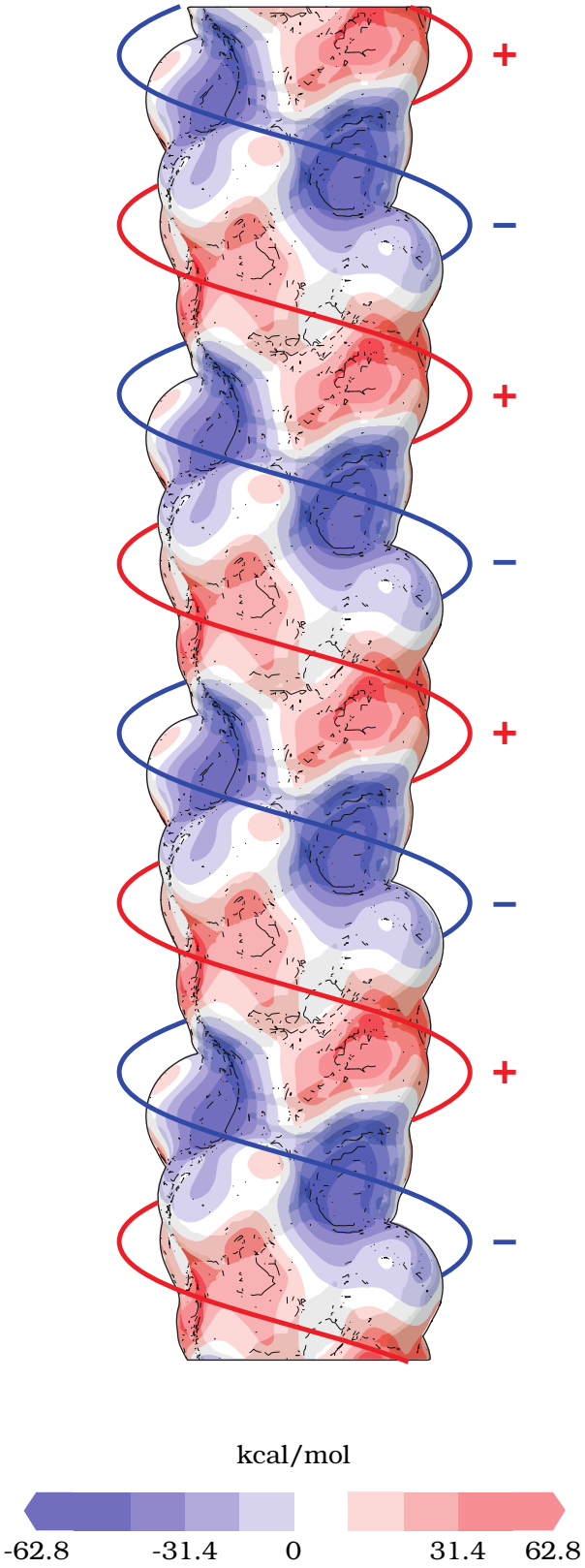

Figure 7.14: Electrostatic map showing the positively and negatively charged helical ribbons.

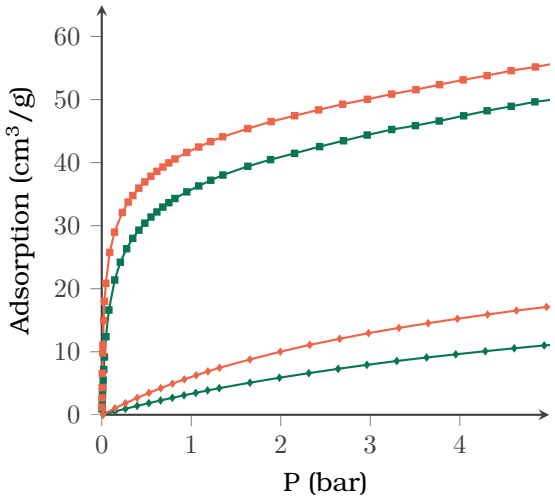

Figure 7.15: CO_2 (squares) and N_2 (diamonds) adsorption isotherms of CPOS-5 collected at 273 K (orange) and 298 K (green).

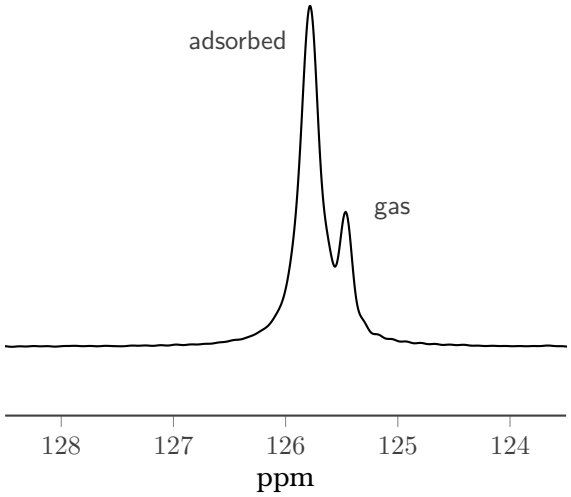

Figure 7.16: ^{13}C MAS collected on CPOS-5 loaded with ^{13}C enriched-CO_2. It is possible to distinguish the signal of the gas phase (125.5 ppm) from the CO_2 in the pores (125.8 ppm).

CO_2 Study

The porous material was loaded with ^{13}C enriched-CO_2, ^{13}C MAS NMR spectrum shows two signals of enriched-CO_2; at 125.5 ppm for the free gas and at 125.8 ppm for CO_2 adsorbed in the pores (Fig. 7.16). The downfield is generated by the magnetic susceptibility effect experienced by molecules embedded in the polar environment of the crystal.

Notably, the adsorbed CO_2 signal dominates in the CP spectra due to the fast magnetization transfer even at room temperature. This implies a very short distance between CO_2 and the hydrogens of the matrix (<1 nm)[23] demonstrating that the gas is exceptionally well retained. This phenomenon is incredibly difficult to achieve because, due to the short gas residence time, the transfer of nuclear polarization from a solid to a gas is inefficient. The fact that happens so easily even at room temperature is even more unique.

In order to identify the hydrogens that interact best with the gas, we performed a series of 2D ^{1}H-^{13}C HETCOR MAS NMR experiments (Fig. 7.17). Even with a contact time of 0.5 ms at room temperature, CO_2 is able to receive magnetization from amidinium hydrogens. DFT calculations reveal the adsorption site is right next to these groups, where one of the CO_2 oxygens can favourably interact with the amidinium. The carbon-hydrogen distance is 3.24 Å.

The second closest hydrogen belongs to the aromatic group of DAB, with a C-H distance of 4.18 Å. The HETCOR experiment with longer contact time reveals also this correlation. TBS hydrogens are not expose to the channel and are too far from the gas molecule for magnetization transfer.

From the combined NMR and modelling approach, we can conclude that the charge distribution of the host complements the charges on the CO_2 molecule and determines the stabilization of the gas in the channels. This also explains the high isosteric heat of adsorption and the good adsorption performance.

The dynamics of CO_2 inside CPOS-5 can be studied by performing ^{13}C static NMR experiments at variable temperature (Fig. 7.18). Anisotropies are incredibly narrow compared to the solid sample (dry ice).[24,25] The simulations assume a 4-fold flip mechanism with jumps of 90°, compatible with the symmetry of the channel, at different frequencies in function

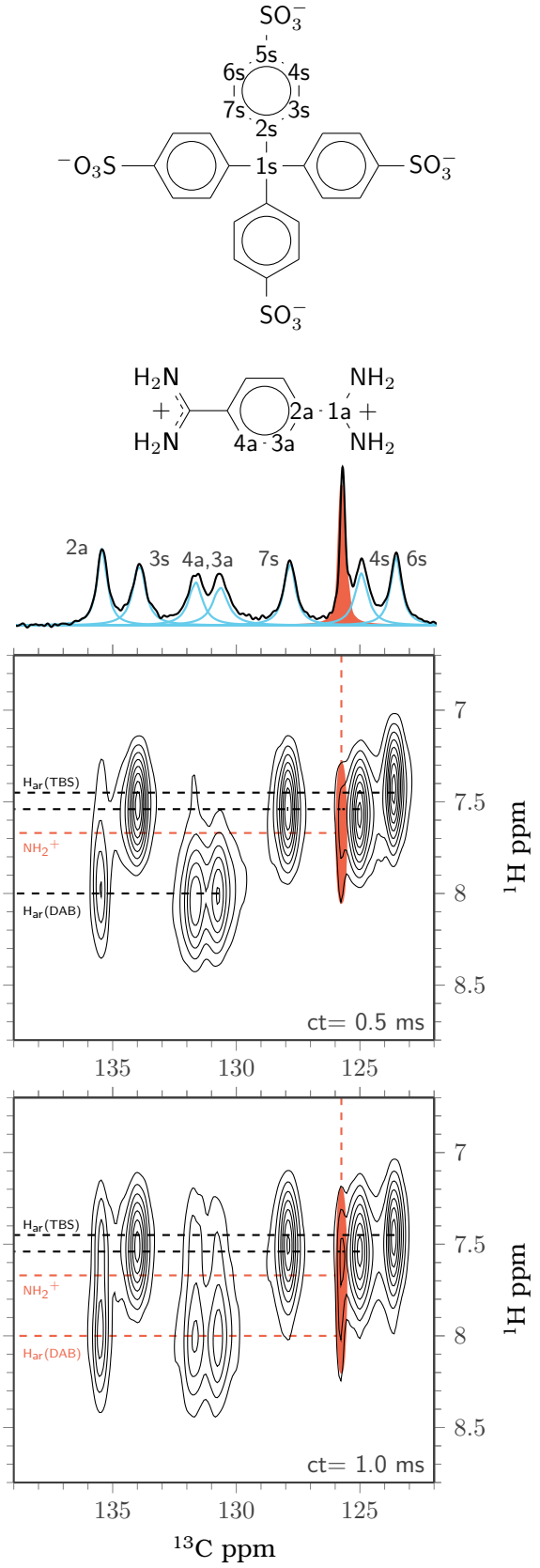

Figure 7.17: 2D ^{1}H-^{13}C hetero correlated MAS NMR spectra of CO_2 loaded CPOS-5 at room temperature and at two distinct contact times (ct). The host-CO_2 cross peaks are highlighted.

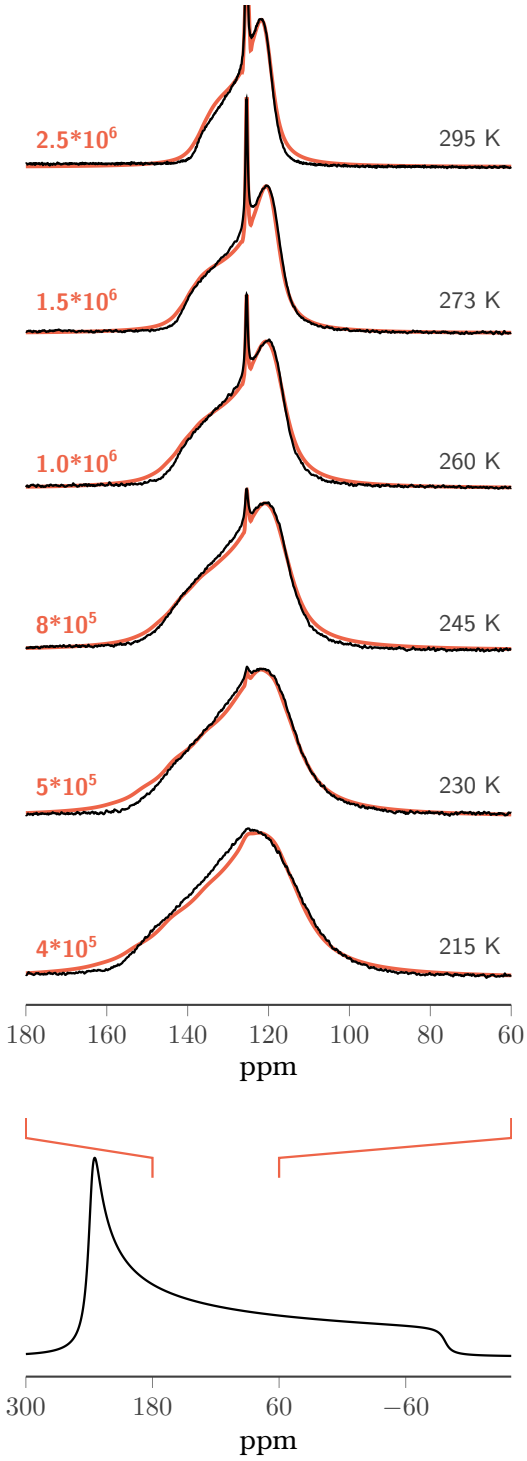

Figure 7.18: Variable temperature ^{13}C NMR spectra of the CPOS-5/$^{13}CO_2$ sample under static conditions. The chemical shift anisotropic lineshape of solid CO_2, simulated starting from the main tensor components, is reported below for comparison.

of the temperature. This analysis also emphasizes a very specific inclination of the molecule axis respect to the channel. The angle is 56.7° at 295 K and increases to 58.1° by lowering the temperature to 215 K. This is probably due to an increase loading that forces the CO_2 to a flatter conformation. The frequency is incredibly high (> 10^5 Hz) even at low temperature. Arrhenius plot indicates an activation energy of 2.9 kcal/mol (Fig. 7.19).

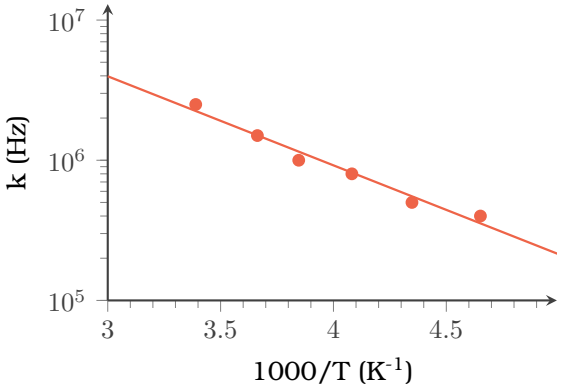

Figure 7.19: Arrhenius plots of the simulated $^{13}CO_2$ spectra of CPOS-5.

Although the NMR analysis provides a considerable amount of information on the dynamics of the gas, deeper insights are needed for a complete picture. In this regard, molecular dynamics and *ab initio* calculations were valuable sources of details. In particular, the location of the adsorption site was important to define the electrostatic distribution that shows a helical distrbution of positive and negative charges that influence the motion. CO_2 diffusion is based on a rototranslational mechanism (i.e. simultaneous rotation and translation along the *c*-axis) dictated by the electrostatic distribution, this implies a helical trajectory by a screwing path along a single file. The estimated energy required for a jump is 2.1 kcal/mol (Fig. 7.20), very similar to the result obtained with the Arrhenius plot.

Calculations also confirm the angle between CO_2 axis and the *c*-axis measured by NMR. At low loading the angle is

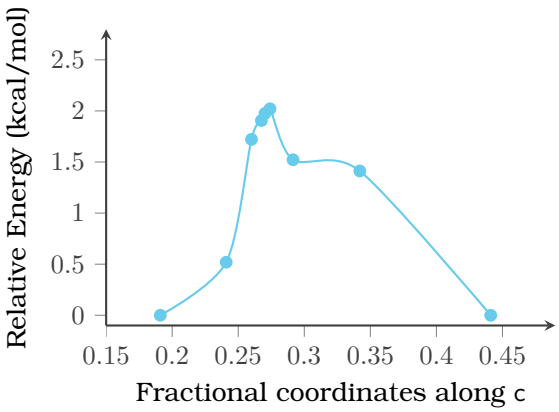

Figure 7.20: Energy profile for the rototranslation of CO_2 by *ab initio* calculation.

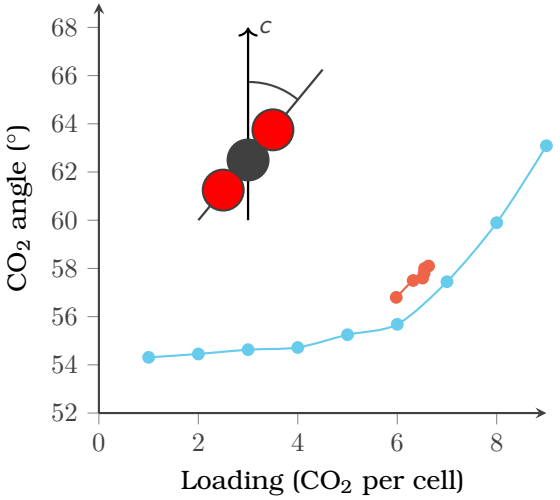

Figure 7.21: Variation of the angle between the CO_2 axis and the channel *c*-axis from NMR (orange) and *ab initio* calculations (azure).

constant, instead it increases when 4 molecules per cell increases rapidly (Fig. 7.21). This is due to the ideal CO_2 loading which consists in only half of the adsorption sites occupied, above this level (that is exactly 4 molecules per cell), the CO_2-CO_2 interactions became stronger, increasing the inclination. The values are also in good agreement with the NMR data.

It is interesting to notice how the electrostatic charge distribution in the channel strongly influences the behaviour of CO_2. This generates very strong adsorption sites but, due to the electrostatic path between them, a very

low barrier jump (Fig. 7.22). So while adsorption is surprisingly high, diffusion inside the channels is incredibly fast. This two elements generate an unique material for CO_2 adsorption.

The imprint of the double ribbon potential into the motion is just the so-called "cherry on the cake". These unique results generate a relatively simple environment for understanding the contribution of electrostatic interactions on motion. Such knowledge can be useful for the study of more complex biological systems. In fact, the diffusion of CO_2 in narrow helical channels, such as in aquaporins, plays a strategic role in the selection and concentration of gases in plant cells.[26,27] Our newly fabricated crystalline channels share the helical and sub-nanometric structural features, and transport properties in a single file through the polar environment, thus achieving high selectivity.

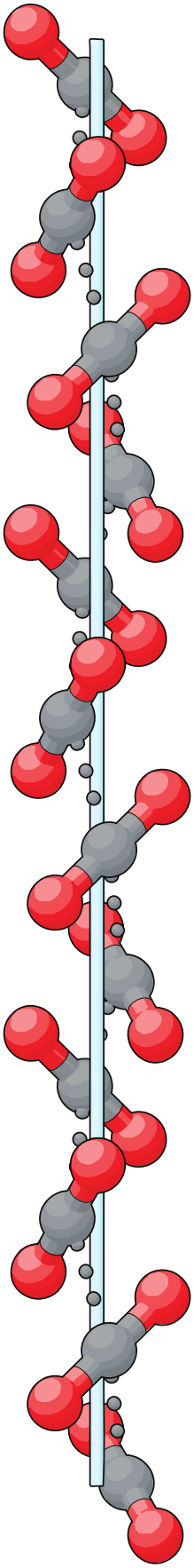

Figure 7.22: Helical trajectory of CO_2.

Bibliography

[1] Thomas, S.; Runcy, W.; S, A.; George, S. *Transport Properties of Polymeric Membranes*; Elsevier Science, 2017.

[2] Nichols, F. Kinetics of diffusional motion of pores in solids. *Journal of Nuclear Materials* **1969**, *30*, 143–165.

[3] Barrie, P. J.; McCann, G. F.; Gameson, I.; Rayment, T.; Klinowski, J. Variable-temperature xenon-129 NMR studies of a pillared montmorillonite. *The Journal of Physical Chemistry* **1991**, *95*, 9416–9419.

[4] Cheung, T. T. P. Temperature dependence of ^{129}Xe NMR of xenon in microporous solids. *The Journal of Physical Chemistry* **1995**, *99*, 7089–7095.

[5] Yang, J.; Ma, J.-F.; Liu, Y.-Y.; Batten, S. R. Four-, and six-connected entangled frameworks based on flexible bis(imidazole) ligands and long dicarboxylate anions. *CrystEngComm* **2009**, *11*, 151–159.

[6] Cheon, Y. E.; Suh, M. P. Selective gas adsorption in a microporous metalorganic framework constructed of Co^{II}_2 clusters. *Chemical Communications* **2009**, 2296–2298.

[7] Yang, W.; Greenaway, A.; Lin, X.; Matsuda, R.; Blake, A. J.; Wilson, C.; Lewis, W.; Hubberstey, P.; Kitagawa, S.; Champness, N. R.; Schroder, M. Exceptional thermal stability in a supramolecular organic framework: porosity and gas storage. *Journal of the American Chemical Society* **2010**, *132*, 14457–14469.

[8] Sumida, K.; Rogow, D. L.; Mason, J. A.; McDonald, T. M.; Bloch, E. D.; Herm, Z. R.; Bae, T.-H.; Long, J. R. Carbon dioxide capture in metalorganic frameworks. *Chemical Reviews* **2012**, *112*, 724–781.

[9] Han, S. S.; Furukawa, H.; Yaghi, O. M.; Goddard, W. A. Covalent organic frameworks as exceptional hydrogen storage materials. *Journal of the American Chemical Society* **2008**, *130*, 11580–11581.

[10] Lu, W.; Yuan, D.; Sculley, J.; Zhao, D.; Krishna, R.; Zhou, H.-C. Sulfonate-grafted porous polymer networks for preferential CO_2 adsorption at low pressure. *Journal of the American Chemical Society* **2011**, *133*, 18126–18129.

[11] Zeng, Y.; Zou, R.; Zhao, Y. Covalent organic frameworks for CO_2 capture. *Advanced Materials* **2016**, *28*, 2855–2873.

[12] Bracco, S.; Piga, D.; Bassanetti, I.; Perego, J.; Comotti, A.; Sozzani, P. Porous 3D polymers for high pressure methane storage and carbon dioxide capture. *Journal of Materials Chemistry A* **2017**, *5*, 10328–10337.

[13] Sozzani, P.; Bracco, S.; Comotti, A.; Ferretti, L.; Simonutti, R. Methane and carbon dioxide storage in a porous van der waals crystal. *Angewandte Chemie International Edition* **2005**, *44*, 1816–1820.

[14] Kim, H.; Kim, Y.; Yoon, M.; Lim, S.; Park, S. M.; Seo, G.; Kim, K. Highly selective carbon dioxide sorption in an organic molecular porous material. *Journal of the American Chemical Society* **2010**, *132*, 12200–12202.

[15] Galli, S.; Maspero, A.; Giacobbe, C.; Palmisano, G.; Nardo, L.; Comotti, A.; Bassanetti, I.; Sozzani, P.; Masciocchi, N. When long bis(pyrazolates) meet late transition metals: structure, stability and adsorption of metalorganic frameworks featuring large parallel channels. *Journal of Materials Chemistry A* **2014**, *2*, 12208.

[16] Wang, H.; Li, B.; Wu, H.; Hu, T.-L.; Yao, Z.; Zhou, W.; Xiang, S.; Chen, B. A flexible microporous hydrogen-bonded organic framework for gas sorption and separation. *Journal of the American Chemical Society* **2015**, *137*, 9963–9970.

[17] He, Y.; Zhou, W.; Qian, G.; Chen, B. Methane storage in metalorganic frameworks. *Chem. Soc. Rev.* **2014**, *43*, 5657–5678.

[18] Jameson, C. J.; Jameson, A. K.; Gerald, R.; de Dios, A. C. ^{129}Xe nuclear magnetic resonance studies of xenon in zeolite CaA. *The Journal of Chemical Physics* **1992**, *96*, 1690–1697.

[19] Xing, G.; Bassanetti, I.; Bracco, S.; Negroni, M.; Bezuidenhout, C.; Ben, T.; Sozzani, P.; Comotti, A. A double helix of opposite charges to form channels with unique CO_2 selectivity and dynamics. *Chemical Science* **2019**, *10*, 730–736.

[20] Yazaydın, A. O.; Snurr, R. Q.; Park, T.-H.; Koh, K.; Liu, J.; LeVan, M. D.; Benin, A. I.; Jakubczak, P.; Lanuza, M.; Galloway, D. B.; Low, J. J.; Willis, R. R. Screening of metal-organic frameworks for carbon dioxide capture from flue gas using a combined experimental and modeling approach. *Journal of the American Chemical Society* **2009**, *131*, 18198–18199.

[21] Lü, J.; Perez-Krap, C.; Suyetin, M.; Alsmail, N. H.; Yan, Y.; Yang, S.; Lewis, W.; Bichoutskaia, E.; Tang, C. C.; Blake, A. J.; Cao, R.; Schröder, M. A robust binary supramolecular organic framework (SOF) with high CO_2 adsorption and selectivity. *Journal of the American Chemical Society* **2014**, *136*, 12828–12831.

[22] Li, P.; He, Y.; Zhao, Y.; Weng, L.; Wang, H.; Krishna, R.; Wu, H.; Zhou, W.; O'Keeffe, M.; Han, Y.; Chen, B. A rod-packing microporous hydrogen-bonded organic framework for highly selective separation of C_2H_2/CO_2 at room temperature. *Angewandte Chemie International Edition* **2014**, n/a–n/a.

[23] Pines, A.; Gibby, M. G.; Waugh, J. S. Proton-enhanced NMR of dilute spins in solids. *The Journal of Chemical Physics* **1973**, *59*, 569–590.

[24] Bowers, C.; Long, H.; Pietrass, T.; Gaede, H.; Pines, A. Cross polarization from laser-polarized solid xenon to $^{13}CO_2$ by low-field thermal mixing. *Chemical Physics Letters* **1993**, *205*, 168–170.

[25] Kong, X.; Scott, E.; Ding, W.; Mason, J. A.; Long, J. R.; Reimer, J. A. CO_2 dynamics in a metal-organic framework with open metal sites. *Journal of the American Chemical Society* **2012**, *134*, 14341–14344.

[26] Uehlein, N.; Lovisolo, C.; Siefritz, F.; Kaldenhoff, R. The tobacco aquaporin NtAQP1 is a membrane CO_2 pore with physiological functions. *Nature* **2003**, *425*, 734–737.

[27] Hibbs, R. E.; Gouaux, E. Principles of activation and permeation in an anion-selective Cys-loop receptor. *Nature* **2011**, *474*, 54–60.

8. Fluorinated Porous Aromatic Frameworks

Summary

A series of new flourinated porous aromatic frameworks has been studied in order to recognize the role played by fluorine atoms on the gas adsorption proprieties especially for CO_2.

The porous 3D selectively fluorinated framework (F-PAF1), robust yet flexible and with a surface area of 2050 m^2/g, was synthesised by condensation of an *ad hoc* prepared fluorinated tetraphenylmethane (TPM) monomer to ensure homogenously distributed C-F dipoles in the swellable architecture. Tetradentate TPM was also used as comonomer for the reaction with fluorinated difunctional monomers to obtain frameworks (FMFs) with a controlled amount of regularly spaced reorientable C-F dipoles. The isosteric heat of adsorption of CO_2 was increased by 53% after C-F dipole insertion, with respect to the non-fluorinated frameworks. CO_2/N_2 selectivity was also increased up to a value of 50 for the difluoro-containing comonomer. Moreover, methane shows optimal interaction energies of 24 kJ/mol.[1]

8.1 Functionalization of PAFs

The interest in PAFs is growing thanks to their remarkable surface area adsorption capabilities combined with thermal and chemical robustness[2,3]. Despite their impressive loading capacity, they have a very low CO_2/N_2 selectivity.[4–6] This detail greatly reduces their possible use as molecular filters.

A strategy to improve selectivity involves the insertion of electron-rich functional groups, by pre- and post-synthetic approaches, which are expected to increase the material affinity towards CO_2.[7–11]the functionalization has the advantage of adding a species with good interaction with the desired gas at the expense of the total pore volume. Fluorine is a promising agent to increasing CO_2 adsorption due to its high electronegativity but small enough to not significantly affect the pore volume. This strategy has already been used in several porous organic materials with good results, in particular by improving the material adsorption capability.[12,13]

Usually, the pore size distribution is obtained from adsorption isotherms, but in the PhD thesis work I decided to evaluate the possibility of using hyperpolarized xenon to get more detailed information. The technique is fast and takes only few minutes to collect a spectrum. Probably due to the novelty of these materials (PAF1,2009),[4] there are no previous examples of the use of such technique on these porous systems. The only other examples of xenon in PAFs are two studies about adsorption isotherms and selectivity but no NMR spectra were acquired.[14,15] This is the first reported example of NMR study of xenon diffused in PAFs.

Synthesis

We extended the library of existing fluorinated materials reporting the synthesis of new fluorinated organic porous materials by adopting two distinct strategies: direct condensation of an *ad hoc* fluorinated tetrahedral monomer, specifically designed for this sake, and copolymerization between two complementary functionalities of tetrahedral (A_4) and fluorine-containing linear (B_2) struts such as monofluoro and difluoro-*p*-phenylene units. By this synthetic strategy the fluorine atoms are regularly bound onto

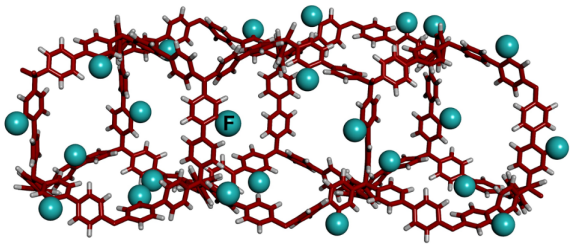

Figure 8.1: Schematic representation of fluoro porous aromatic framework F-PAF1. Blue spheres represent fluorine atoms.

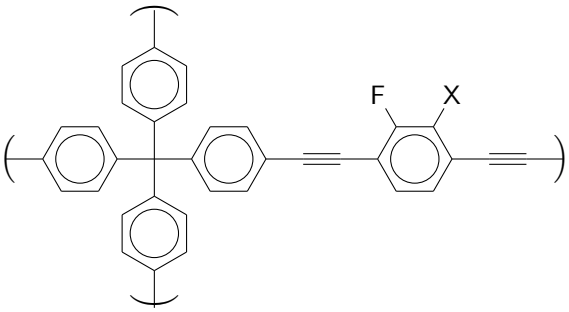

Figure 8.2: 1-FMF (X=H) and 2-FMF (X=F).

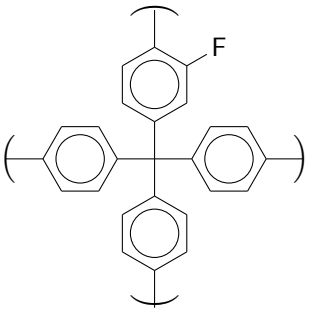

Figure 8.3: F-PAF1.

each monomeric unit and are exposed to the pore volume (Fig. 8.1).

Our design was to build local C-F dipoles that imparted a dipole moment to the whole *p*-phenylene moiety, wherein C-F groups are inserted. This was made possible by arranging the dipolar substituents in a non-centrosymmetric manner. The frameworks were designed to bear a limited number of fluorine atoms in order to keep the skeleton as light as possible and at the same time a regularly spaced fluorine substitution. Such homogeneous distribution ensures that the carbon-fluorine dipoles are exposed to the diffusing-in gases, resulting in a well-distinct behaviour as compared to the unfluorinated skeleton.

The condensation of fluorinated microporous frameworks (FMFs) employs a Sonogashira coupling protocol to create an extended copolymer framework between tetrakis(4-bromophenylmethane) and a difunctional 1,4- diethynyl-2-fluorobenzene or 1,4-diethynyl-2,3-difluorobenzene in a 1 : 2 ratio, leading to the formation of 1-FMF and 2-FMF (Fig. 8.2), respectively. The fluorinated porous aromatic framework F-PAF1 (Fig. 8.3) was prepared by the Yamamoto-type homopolymerization reaction of 4,4',4"-((4-bromo-3-fluorophenyl)methantryl)tris(bromobenzene).

TGA curves of the fluoro-containing frameworks show their extremely high stability, up to 450-500 °C, as a consequence of the fully covalent bond network.

^{13}C MAS NMR

^{13}C CP MAS NMR spectra show the chemical structure of the frameworks (Fig. 8.4). Signal assignments were established by comparison to solution ^{13}C-NMR spectra of the monomers. Besides the signals of non-fluorinated moieties, characteristic signals of the presence of fluorine atoms on *p*-phenylene rings appear in the aromatic region (highlighted in orange). The peak at 65 ppm belongs to the central quaternary carbon atom of the tetraphenylmethane units, while the resonances in the 80-100 ppm region of 1-FMF and 2-FMF correspond to the *sp* carbon atoms. Notably, in F-PAF1 the doublet due to the 250 Hz $J(^{13}C\text{-}^{19}F)$ coupling of the carbon nucleus directly bonded to the fluorine atom is apparent at 160 ppm.

Carbon relaxation times indicate a fast 10^8 Hz reorientation rate for the non-fluorinated para-phenylenes (T_1=1.5 s for C_3), as occurring in prototypal PAF-1 rotors.[16,17] Despite a comparable torsional flexibility of fluorinated rings about the pivotal sp_2-sp_2 carbon-carbon bonds,

orientational dynamics of fluorinated rings was slower, as proved by longer spin-lattice relaxation times (T_1>10 s) owing to the increased inertial mass of the rotor and long-range electrostatic interactions among C-F dipoles. Overall, dynamical results depict a skeleton bearing reorientable aromatic moieties, potentially adaptable after guest diffusion.

Porosity Evaluation

The porosity of the materials was evaluated by N_2 adsorption/desorption isotherms at 77 K (Fig. 8.5). The Langmuir and BET surface areas of F-PAF1 are 2338 and 2054 m^2/g, respectively: these values are among the highest reported for fluorinated organic porous materials.[7,12,13] The shape shows a contribution by the mesoporosity resulting in a total pore volume of 1.96 cm^3/g that is outstanding for a fluorinated organic porous material. Pore size distribution (PSD) analysis, carried out by non-local density functional theory (NLDFT) and the carbon slit pore model, shows a peak centered at 11.9 Å.

1-FMF and 2-FMF show Langmuir isotherms characteristic of microporous solids with Langmuir and BET surface areas of 1285 and 1132 m^2/g for 1-FMF and 970 and 853 m^2/g for 2-FMF, respectively. PSD analysis reveals two peaks at ca. 5.9-11.9 Å for 1-FMF and 2-FMF. An increase in the 5.9 Å peak height is observed for the difluoro substituted material, indicating that the increase of fluorine substitution selects an ultramicroporosity range, which offers neat advantages for the adsorption of small gas molecules.

We used ^{129}Xe SEOP NMR to provide more information about the pore size. The exploration of the restricted environment by Xe atoms is manifested by high chemical shift values (104-127 ppm) with respect to the gas phase (Fig. 8.6). The chemical shift increase from F-PAF1 to copolymers reveals the more effective Xe confinement in the smaller pores of the copolymers (from 11 to

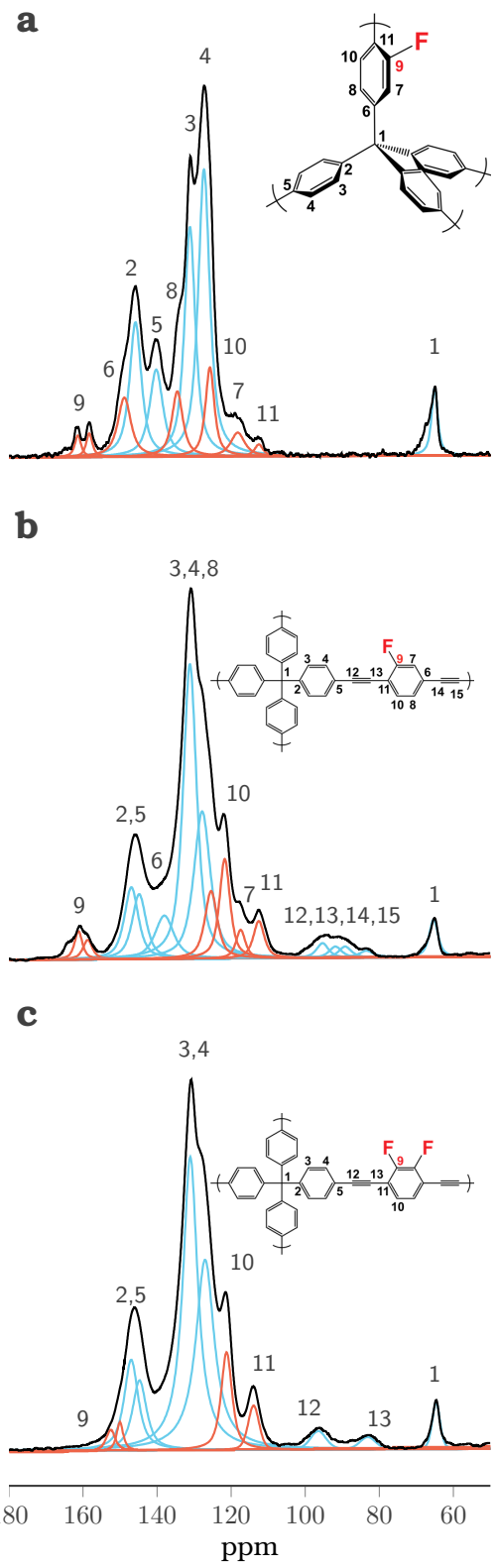

Figure 8.4: ^{13}C CP MAS NMR spectra of (**a**) F-PAF1, (**b**) 1-FMF and (**c**) 2-FMF (contact time = 2 ms). The signals of the fluorinated *p*-phenylene units are highlighted in orange.

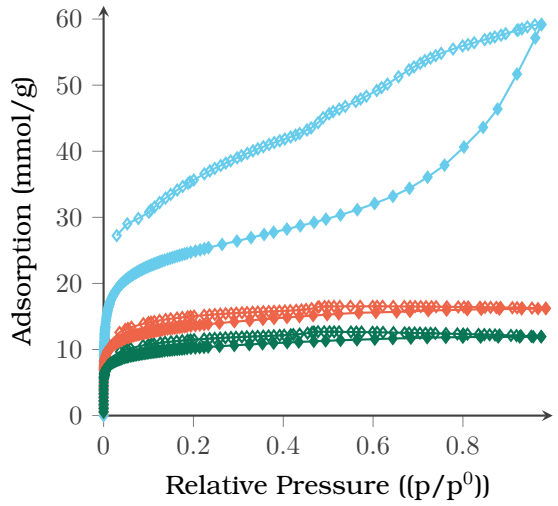

Figure 8.5: N_2 adsorption isotherms collected at 77 K of F-PAF1 (light blue), 1-FMF (orange) and 2-FMF (green).

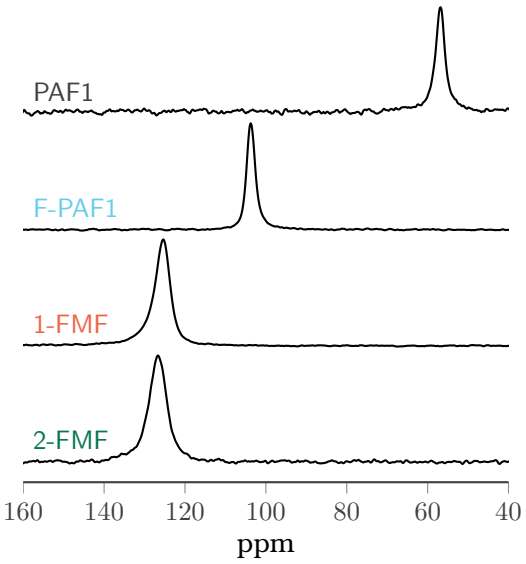

Figure 8.6: Hyperpolarized HP ^{129}Xe NMR spectra collected at room temperature.

6 Å).

Gas Adsorption and Selectivity

The new fluorinated matrices were tested for carbon dioxide and methane capture. CO_2 sorption isotherms were collected at 195 K up to 1 bar and at three other distinct temperatures (273, 283, and 298 K) up to 10 bar (Fig. 8.7). Owing to its higher surface area, F-PAF1 shows a remarkable CO_2 uptake at 195 K and 1 bar, reaching the value of 26.3 mmol/g, which corresponds to 115% of its weight. Interestingly, in F-PAF1, the CO_2 adsorption value at 273 K and 1 bar is superior to that reported for the unfunctionalized PAF1 (2.7 vs. 2.0 mmol/g, respectively),[18] despite the lower BET surface area (2054 vs. 5300 m^2/g, respectively). The presence of fluorine atoms enhances low-pressure CO_2 capture through favorable electrostatic interactions. Similarly, the CO_2 uptake for 1-FMF at 273 K and 1 bar is superior to that for its non-fluorinated analogue MOP1 (2.4 vs. 2.1 mmol /g, respectively).[8]

Furthermore, the CO_2 isosteric heat of adsorption, calculated using the van't Hoff equation at low coverage for F-PAF1 is 25 kJ/mol (Fig. 8.8), which is significantly higher than 15.6 kJ/mol determined for PAF1.[19] Notably, the CO_2 isotherm changes from a sigmoidal shape for PAF1 to a Langmuir profile for F-PAF1, owing to a higher CO_2 affinity towards the fluorinated surface. Thus, the use of a fluorinated building block leads to a 53% increase of the heat of adsorption with respect to the non-fluorinated analogue. For 1-FMF, the heat calculated at low coverage is 30 kJ/mol, indicating favorable interactions with CO_2. These values are higher than that of the parent non-fluorinated framework (26 kJ/mol), demonstrating the effectiveness of the C-F dipole insertion to enhance the CO_2 capture. It is expected that two vicinal fluorine atoms further increase the binding energy because of the cooperative interactions with the positively charged carbon of CO_2, as previously proved by theoretical calculations.[20] Indeed, for 2-FMF the heat of adsorption reached 32 kJ/mol. Furthermore, the torsional flexibility of the Csp_2-Csp bond about the monofluoro and difluoro-*p*-phenylene moieities[21] may allow adjustment of the conformation in order to maximize the dipole-CO_2 interaction.

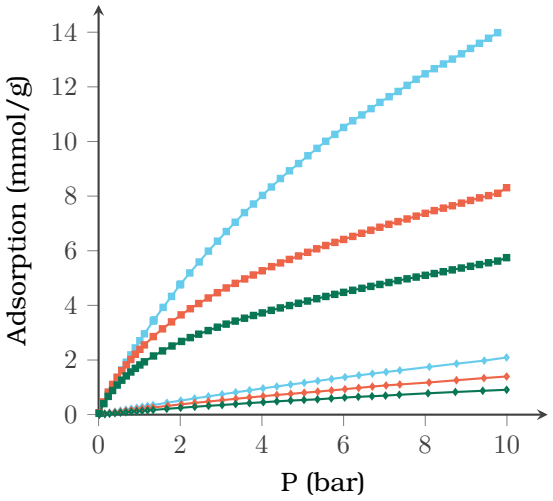

Figure 8.7: CO_2 (squares) and N_2 (diamonds) adsorption isotherms collected at 273 K and up to 10 bar of F-PAF1 (**light blue**), 1-FMF (**orange**) and 2-FMF (**green**).

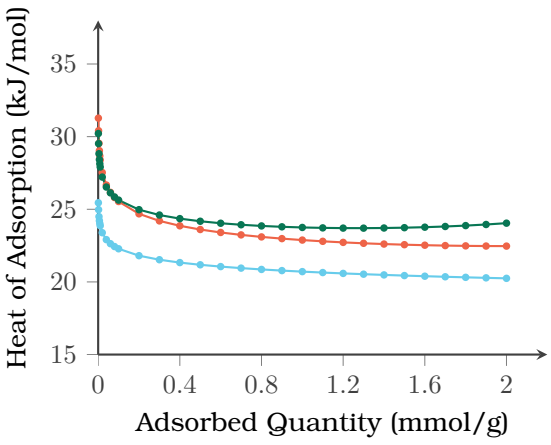

Figure 8.8: CO_2 heat of adsorption calculated with van't Hoff equation for F-PAF1 (**light blue**), 1-FMF (**orange**) and 2-FMF (**green**).

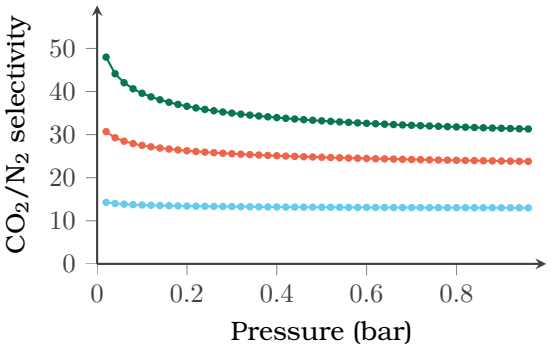

Figure 8.9: IAST selectivity for the adsorption of CO_2 over N_2 from 15:85 mixture calculated at 273 K for F-PAF1 (**light blue**), 1-FMF (**orange**) and 2-FMF (**green**).

The higher CO_2 heat of adsorption for the fluorinated matrices was reflected in the higher CO_2/N_2 selectivity values derived using the Ideal Adsorbed Solution Theory (IAST) in the case of the 15/85 CO_2/N_2 mixture, typical of industrial fume emissions (Fig. 8.9). At 273 K, the covalent frameworks exhibited a CO_2/N_2 selectivity as high as 31 and 48 for 1-FMF and 2-FMF, respectively. The selectivity of 1-FMF and 2-FMF is superior to that of the porous materials obtained by post-synthetic fluorination methods recently reported.[13]

Since enhanced interactions can be expected towards CH_4 owing to the polarity of the C-F bond, CH_4 adsorption measurements were performed at various temperatures to characterize the process (Fig. 8.10 and 8.11). The heat of adsorption for F-PAF1 (17 kJ/mol) is higher than that of the non-fluorinated analogue (14 kJ/mol),[22] which confirms the increased CH_4 affinity owing to the presence of fluorine in the porous matrix. 1-FMF and 2-FMF show a remarkably higher adsorption heat of up to 20 and 24 kJ/mol, respectively. The presence of two adjacent fluorine atoms on the *p*-phenylene moiety increases the dipole moment and plays a key role in enhancing the interactions of the framework with CH_4. Additionally, the sub-nanometer pore size increases van der Waals stabilisation which significantly contributes to the remarkably favorable CH_4 binding energy. The heat of adsorption values are competitive with the values reported for the best performing MOFs and COFs. In particular, they exceed the reported value for H-KUST-1 (18.2 kcal/mol), a Cu(II)-based MOF whose methane adsorption properties are considered the benchmark in the field of porous materials and suitable for practical uses.[23]

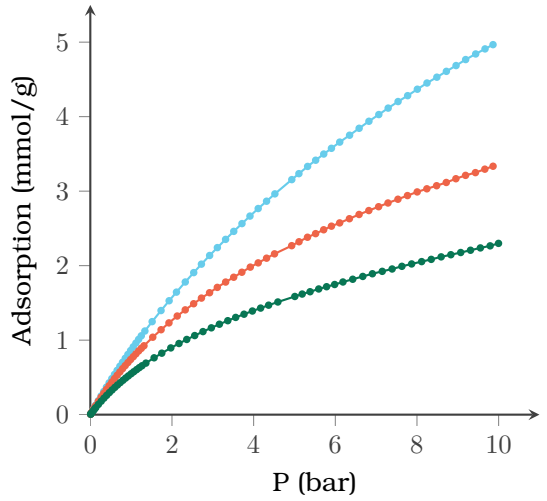

Figure 8.10: CH_4 adsorption isotherms collected at 273 K and up to 10 bar of F-PAF1 (light blue), 1-FMF (orange) and 2-FMF (green).

Furthermore, the CH_4/N_2 (50:50 mixture) and CO_2/CH_4 (50:50 mixture) selectivities were studied, using IAST theory, to evaluate the performance of materials towards gas purification (Fig. 8.12 and 8.13). 1-FMF and 2-FMF show good selectivity for both CO_2/CH_4 and CH_4/N_2 binary mixtures. In particular, the CO_2/CH_4 selectivity of 1-FMF at 273 K and 298 K of 5.4 is close to that of HKUST-1 (estimated as 4.8).[24]

The results presented demonstrate the active role played by fluorine-containing moieties in improving CO_2 and CH_4 capture. In particular, the calibrated introduction of fluorine groups in F-PAF1 increased the heat of adsorption for CO_2 by 53% compared to its non-fluorinated analogue.

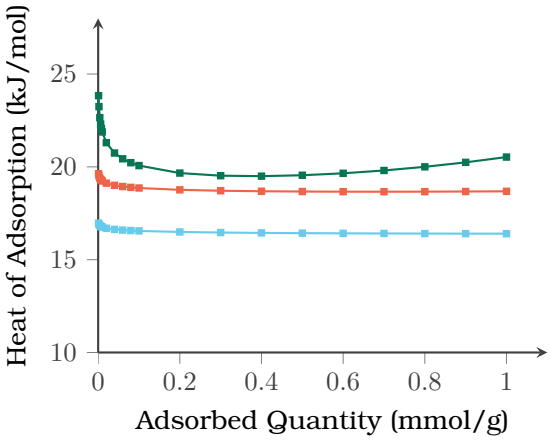

Figure 8.11: CH_4 heat of adsorption calculated with van't Hoff equation for F-PAF1 (light blue), 1-FMF (orange) and 2-FMF (green).

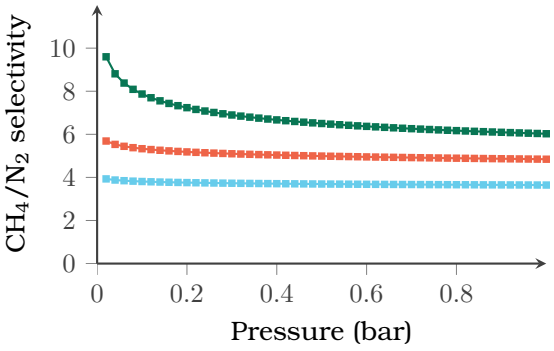

Figure 8.12: IAST selectivity for the adsorption of CH_4 over N_2 from 50:50 mixture calculated at 273 K for F-PAF1 (light blue), 1-FMF (orange) and 2-FMF (green).

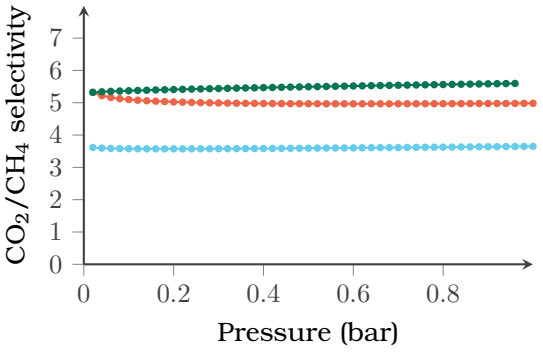

Figure 8.13: IAST selectivity for the adsorption of CO_2 over CH_4 from 50:50 mixture calculated at 273 K for F-PAF1 (light blue), 1-FMF (orange) and 2-FMF (green).

Bibliography

[1] Comotti, A.; Castiglioni, F.; Bracco, S.; Perego, J.; Pedrini, A.; Negroni, M.; Sozzani, P. Fluorinated porous organic frameworks for improved CO_2 and CH_4 capture. *Chemical Communications* **2019**, *55*, 8999–9002.

[2] Zou, X.; Ren, H.; Zhu, G. Topology-directed design of porous organic frameworks and their advanced applications. *Chemical Communications* **2013**, *49*, 3925–3936.

[3] Zhang, H.; Li, G.; Liao, C.; Cai, Y.; Jiang, G. Bio-related applications of porous organic frameworks (POFs). *Journal of Materials Chemistry B* **2019**, *7*, 2398–2420.

[4] Ben, T.; Ren, H.; Ma, S.; Cao, D.; Lan, J.; Jing, X.; Wang, W.; Xu, J.; Deng, F.; Simmons, J.; Qiu, S.; Zhu, G. Targeted synthesis of a porous aromatic framework with high stability and exceptionally high surface area. *Angewandte Chemie International Edition* **2009**, *48*, 9457–9460.

[5] Zhao, Y.-C.; Zhou, D.; Chen, Q.; Zhang, X.-J.; Bian, N.; Qi, A.-D.; Han, B.-H. Thionyl chloride-catalyzed preparation of microporous organic polymers through aldol condensation. *Macromolecules* **2011**, *44*, 6382–6388.

[6] Bracco, S.; Piga, D.; Bassanetti, I.; Perego, J.; Comotti, A.; Sozzani, P. Porous 3D polymers for high pressure methane storage and carbon dioxide capture. *Journal of Materials Chemistry A* **2017**, *5*, 10328–10337.

[7] Yang, Z.-Z.; Zhao, Y.; Zhang, H.; Yu, B.; Ma, Z.; Ji, G.; Liu, Z. Fluorinated microporous organic polymers: design and applications in CO_2 adsorption and conversion. *Chemical Communications* **2014**, *50*, 13910–13913.

[8] Yang, Z.-Z.; Zhao, Y.; Ji, G.; Zhang, H.; Yu, B.; Gao, X.; Liu, Z. Fluoro-functionalized polymeric ionic liquids: highly efficient catalysts for CO_2 cycloaddition to cyclic carbonates under mild conditions. *Green Chemistry* **2014**, *16*, 3724–3728.

[9] Zou, L.; Sun, Y.; Che, S.; Yang, X.; Wang, X.; Bosch, M.; Wang, Q.; Li, H.; Smith, M.; Yuan, S.; Perry, Z.; Zhou, H.-C. Porous organic polymers for post-combustion carbon capture. *Advanced Materials* **2017**, *29*, 1700229.

[10] Yang, X.; Zou, L.; Zhou, H.-C. Anchor installation on porous polymer networks (PPNs) for high CO_2 uptake. *Polymer* **2017**, *126*, 303–307.

[11] Perego, J.; Piga, D.; Bracco, S.; Sozzani, P.; Comotti, A. Expandable porous organic frameworks with built-in amino and hydroxyl functions for CO_2 and CH_4 capture. *Chemical Communications* **2018**, *54*, 9321–9324.

[12] Zhao, Y.; Yao, K. X.; Teng, B.; Zhang, T.; Han, Y. A perfluorinated covalent triazine-based framework for highly selective and water-tolerant CO_2 capture. *Energy & Environmental Science* **2013**, *6*, 3684–3692.

[13] Alahmed, A. H.; Briggs, M. E.; Cooper, A. I.; Adams, D. J. Post-synthetic fluorination of Scholl-coupled microporous polymers for increased CO_2 uptake and selectivity. *Journal of Materials Chemistry A* **2019**, *7*, 549–557.

[14] Wang, Q.; Wang, H.; Peng, S.; Peng, X.; Cao, D. Adsorption and separation of Xe in metal-organic frameworks and covalentorganic materials. *The Journal of Physical Chemistry C* **2014**, *118*, 10221–10229.

[15] Li, J.; Huang, L.; Zou, X.; Zheng, A.; Li, H.; Rong, H.; Zhu, G. Porous organic materials with ultra-small pores and sulfonic functionality

for xenon capture with exceptional selectivity. *Journal of Materials Chemistry A* **2018**, *6*, 11163–11168.

[16] Comotti, A.; Bracco, S.; Ben, T.; Qiu, S.; Sozzani, P. Molecular rotors in porous organic frameworks. *Angewandte Chemie International Edition* **2014**, *53*, 1043–1047.

[17] Comotti, A.; Bracco, S.; Sozzani, P. Molecular rotors built in porous materials. *Accounts of Chemical Research* **2016**, *49*, 1701–1710.

[18] Li, Y.; Ben, T.; Zhang, B.; Fu, Y.; Qiu, S. Ultrahigh gas storage both at low and high pressures in KOH-activated carbonized porous aromatic frameworks. *Scientific Reports* **2013**, *3*.

[19] Garibay, S. J.; Weston, M. H.; Mondloch, J. E.; Colón, Y. J.; Farha, O. K.; Hupp, J. T.; Nguyen, S. T. Accessing functionalized porous aromatic frameworks (PAFs) through a de novo approach. *CrystEngComm* **2013**, *15*, 1515–1519.

[20] Dorris, R. E.; Trendell, W. C.; Peebles, R. A.; Peebles, S. A. Rotational spectrum, structure, and interaction energy of the trifluoroethylene-carbon dioxide complex. *The Journal of Physical Chemistry A* **2016**, *120*, 7865–7872.

[21] Comotti, A.; Bracco, S.; Yamamoto, A.; Beretta, M.; Hirukawa, T.; Tohnai, N.; Miyata, M.; Sozzani, P. Engineering switchable rotors in molecular crystals with open porosity. *Journal of the American Chemical Society* **2014**, *136*, 618–621.

[22] Ben, T.; Pei, C.; Zhang, D.; Xu, J.; Deng, F.; Jing, X.; Qiu, S. Gas storage in porous aromatic frameworks (PAFs). *Energy & Environmental Science* **2011**, *4*, 3991–3999.

[23] Konstas, K.; Osl, T.; Yang, Y.; Batten, M.; Burke, N.; Hill, A. J.; Hill, M. R. Methane storage in metal organic frameworks. *Journal of Materials Chemistry* **2012**, *22*, 16698–16708.

[24] Hamon, L.; Jolimaître, E.; Pirngruber, G. D. CO_2 and CH_4 separation by adsorption using Cu-BTC metalorganic framework. *Industrial & Engineering Chemistry Research* **2010**, *49*, 7497–7503.

9. Porous Dipeptides as Volatile Drug Vessels

Summary

Porous crystalline dipeptides absorb, reversibly from the gas phase, a series of volatile fluorinated ethers in use as anesthetics. Their vapor pressure was considerably reduced, with favorable guest capture and release. Variable channel sizes were customized for selective sorption and pressure thresholds were observed in the narrowest pores. ^{1}H, ^{13}C and ^{19}F MAS NMR coupled with *ab initio* conformational analysis and grand canonical Monte Carlo simulations highlight the arrangement of the guest molecules in the cavities and the amount of loaded anesthetics, in agreement with the adsorption isotherms.

This investigation may shed light on the way volatile anesthetics adapt to variable-size subnanometric channels, mimicking biological receptors. Moreover, the biodegradability and biocompatibility of nanoporous dipeptide materials encourages their use in biomedical applications.

9.1 Porous Dipeptides

Biological molecules, especially dipeptides composed by proteinogenic amino-acids, are able to self-assemble into porous architectures and have been proposed as absorptive materials.[1–8] Such dipeptides are outstanding for their large variety of available channels. Supramolecular interactions as stable as charge assisted hydrogen bonding between ammonium and carboxylate end-groups support the porous structure. They are biodegradable and thus environmentally friendly, as opposed to the majority of porous materials.

The biocompatibility of peptides make them suitable as drug delivery systems for hydrophobic drugs. Moreover, the use of nanocrystals as hydrophobic-drug carriers may be attractive for parenteral or oral administration, thanks to the increased solubility and, thus, bioavailability.[9]

However, crystalline porous dipeptides have not yet been exploited for hosting/releasing volatile drugs like anesthetics, although they are particularly intriguing for the subnanometric size of the available spaces. The reduction of the vapour pressure of volatile drugs upon nanoconfinement may give rise to practical advantages in handling and storage.[10,11]

Anesthetics

Halogenated ethers and alkanes have extensive applications in general anesthesia, although there are still difficulties in their storage and delivery without dispersion into the environment.[12] Halothane, enflurane, desflurane and isoflurane (Fig. 9.1), and the non-halogenated diethyl ether, are among the most commonly used substances as anesthetics. These compounds, administered by inhalation, interact with $GABA_A$ receptors in synaptic membranes and cause a reversible loss of consciousness.[13,14] Moreover, most of them belong to the category of chlorofluorocarbon ethers (CFCs) and thus represent a constant danger for the environment.[15–17] The family of volatile halogenated ethers and alkanes was chosen as probing guests, given the high vapour pressure already at 273 K.

Crystal Structures

We investigated porous dipeptides L-valyl-L-alanine (VA), L-alanyl-L-isoleucine (AI), L-valyl-L-valine (VV), L-isoleucyl-L-valine (IV) and L-isoleucyl-L-alanine (IA) (Fig. 9.2), whose hexagonal crystal structures exhibit one-dimensional channels.[3–6,18]

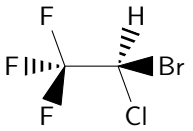

Halothane

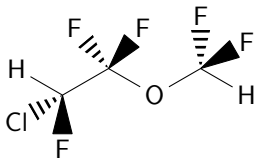

Enflurane

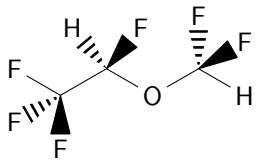

Desflurane

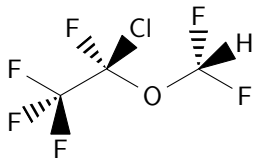

Isoflurane

Figure 9.1: Chemical structures of the halogenated ethers used as guests.

Pores with tailored cross-sections from 5.3 Å to 3.5 Å, as modulated by aliphatic groups lining the inner surface of the walls, offer a great versatility for studying vapour absorptive properties, especially, selectivity and capacity towards the ethers. Indeed, pore size plays a key role in the selective recognition of the anesthetics: dipeptide crystals with channels larger than 4 Å such as VA (Fig. 9.3), AI and VV efficiently absorb the guests whilst IA and IV with pore sizes of about 3.5 Å exclude the anesthetics.

Dynamic light scattering analysis of a suspension of crystals proved that their particle size falls in the nanometric range with a distribution centered at 30 nm. This evidence enforces the perspectives for the use of dipeptides in nanomedicine, because this particle size is suitable for blood stream transport and cell internalization.

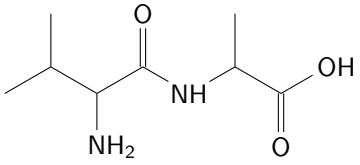

L-valyl-L-alanine

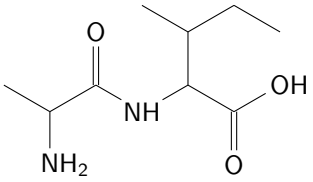

L-alanyl-L-isoleucine

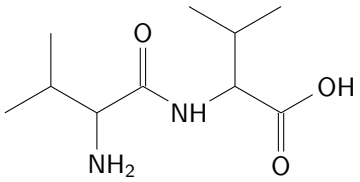

L-valyl-L-valine

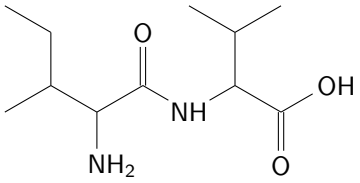

L-isoleucyl-L-valine

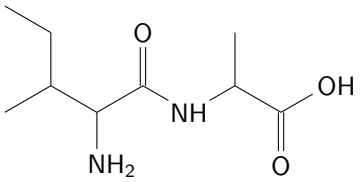

L-isoleucyl-L-alanine

Figure 9.2: Chemical structures of the dipeptides.

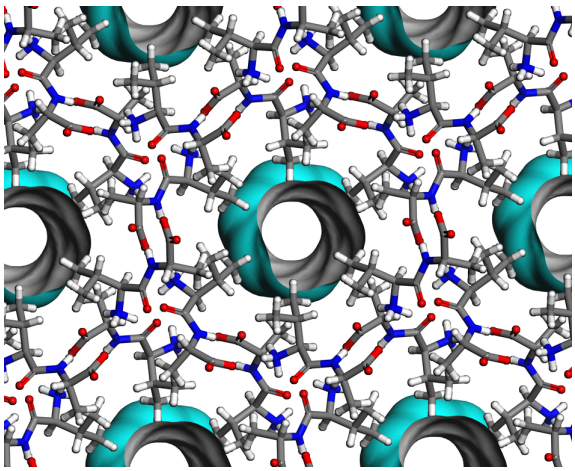

Figure 9.3: Portion of the crystal structure of L-valyl-L-alanine (VA) along the channels axis.

ADSORPTION

The vapour isotherms in VA channels (d = 5.1-5.3 Å, 9.4) exhibited Langmuir-type profiles for all the halogenated guests showing maximum absorption values of 170-200 mmol/mol at 273 K and 80-100 Torr, which correspond to a virtually complete loading of available volume and more than 20% by weight. The unit cell parameters of the samples upon loading remain substantially unaltered, indicating the zeolitic behavior of the molecular crystalline material. Langmuir-type isotherms for enflurane are also shown in the smaller channels of AI (4.7-5.0 Å) and VV (4.0-4.2 Å) owing to the limited steric requirements of the chlorine on the terminal methyl group, which allows easy adjustment in the channels. On the contrary, the isotherms of the isoflurane isomer bearing the chlorine substituent on the methylene group and halothane (containing F, Cl and Br halogens) in VV do not follow a Langmuir profile, this different behavior is particularly accentuated in the case of halothane. In fact, in the channels of VV, halothane isotherms exhibited a minimal adsorption at low pressures followed by an increased uptake above 10 Torr. Thus, at low pressures a selective absorption of enflurane with respect to halothane is exhibited. This behavior is fully reproducible over a few cycles and can be attributed to the flexibility of the structure that expanded upon crossing a pressure threshold. On the contrary, in IA and IV nanochannels with cross-sections of about 3.5 Å the halogenated molecules are excluded for their exceeding steric encumbrance. Interestingly, dipeptides containing the same aminoacids, alanine and isoleucine, in opposite sequences, AI and IA, generate different cross-sections (from 4.7-5.0 Å to 3.5 Å, respectively), that can differentiate the adsorption properties of the same guest. Desflurane, bearing exclusively fluorine atoms as halogens and exhibiting the highest volatility, shows in all dipeptides modest absorption values.

From adsorption isotherms at various temperature, we evaluated the isosteric heats of adsorption by applying the van't Hoff equation. We found out values in the range of 35-50 kJ/mol, which demonstrate the strong affinity between the dipeptide hosts and the guests owing to multiple interactions installed within the narrow channels. These adsorption energies are comparable to the highest values reported for adsorbed anesthetics in porous materials.[19]

^{1}H FAST-MAS NRM

Fast magic angle spinning ^{1}H NMR spectra provided direct evidence of the inclusion of the anesthetics in the crystalline channels of VA, AI and VV upon sorption from the gas phase (Fig. 9.5). An interesting feature is the upfield shift (d = 0.2 ppm) of included halogenated ethers with respect to the pure compounds, owing to the magnetic susceptibility generated by the dipeptide environment.[20–23] Specifically, a sample with an excess of enflurane in VA allowed us to distinguish the signals of free and included enflurane. The signals of the included halogenated molecules have a linewidth wider than that of free molecules owing to stronger ^{1}H homonuclear coupling, indicating that guest molecules undergo restricted motion. Quantitative analysis

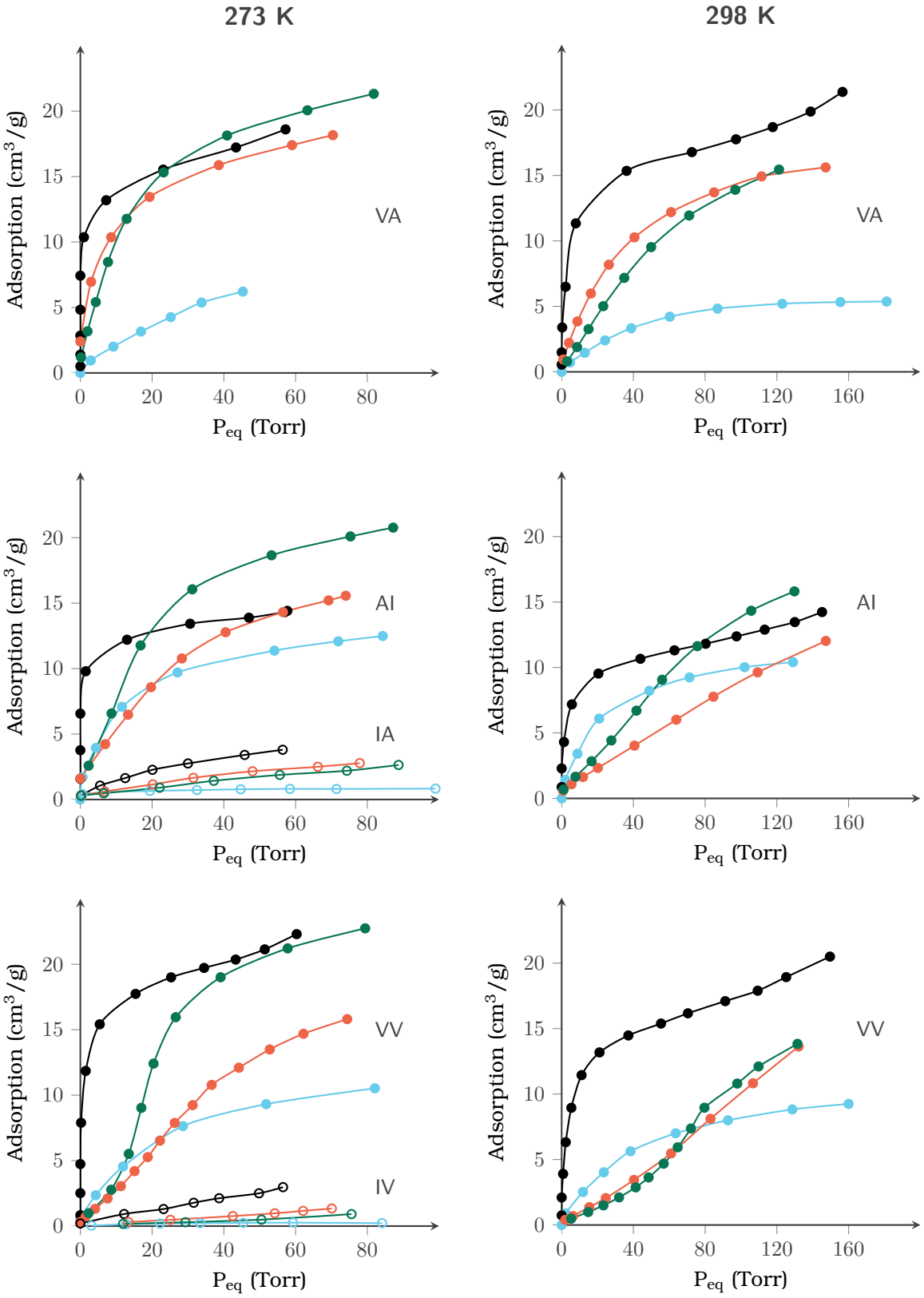

Figure 9.4: Anesthetics adsorption isotherms at 273 K (left) and at 298 K (right). Enflurane (**black**), isoflurane (**orange**), halothane (**green**) and desflurane (**azure**). In IA and IV the labels are empty.

of the amount of included anesthetics with respect to the dipeptide hosts allowed us to measure the maximum loading of the channels. Enflurane, isoflurane and halothane in VA were found to be 0.19, 0.16 and 0.19 mol/mol, respectively, in agreement with the amount measured from adsorption isotherms at 273 K (0.18, 0.16 and 0.19 mol/mol, respectively).

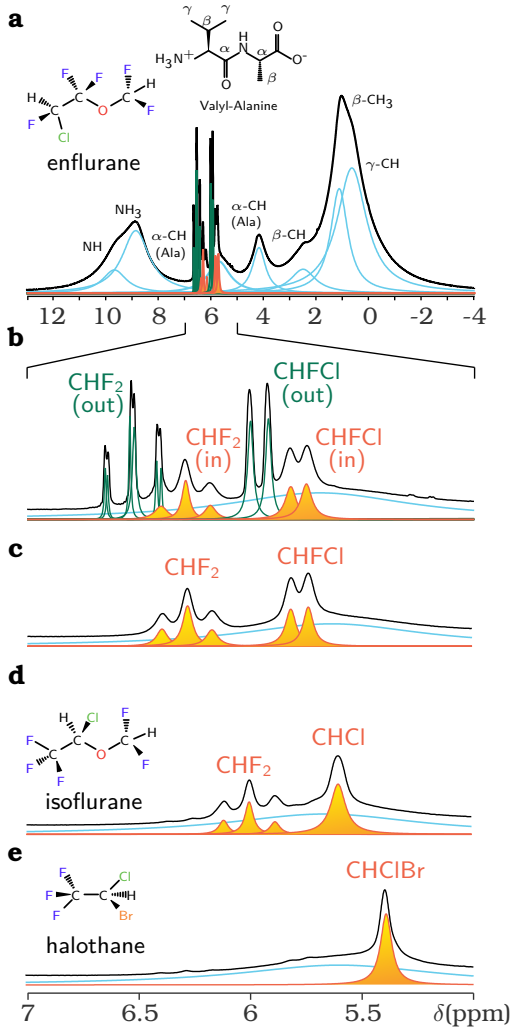

Figure 9.5: 600 ^{1}H fast-MAS NMR (35 kHz spinning speed): **a** VA with enflurane both inside and outside the nanochannels; **b** enlargement of the above spectrum in the 57 ppm range. 1H spectra (57 ppm range) of VA fully loaded with **c** enflurane, **d** isoflurane and **e** halothane. The signals of halogenated ethers confined in the nanochannels and in the bulk are highlighted in orange and green, respectively.

Adsorbate Conformation

However, the conformational arrangement of anesthetics in confined spaces has never been investigated. ^{19}F MAS NMR spectra of isoflurane in the all the dipeptides show a dramatic change with respect to the spectra in the liquid state (Fig. 9.6). Indeed, the ^{19}F NMR spectra of isoflurane confined in VA showed two distinct triplets separated by about 5.3 ppm for the two fluorine nuclei of the CHF_2 group, in contrast to a single multiplet recorded for pure isoflurane in the bulk wherein fast exchange among conformers occurs. Such large separation must be ascribed to the conformational arrangement of the two fluorine atoms and the γ-*gauche* effect that produces an upfield shift of 5 ppm when the observed nucleus changes from a *trans* to a *gauche* conformation.[24]

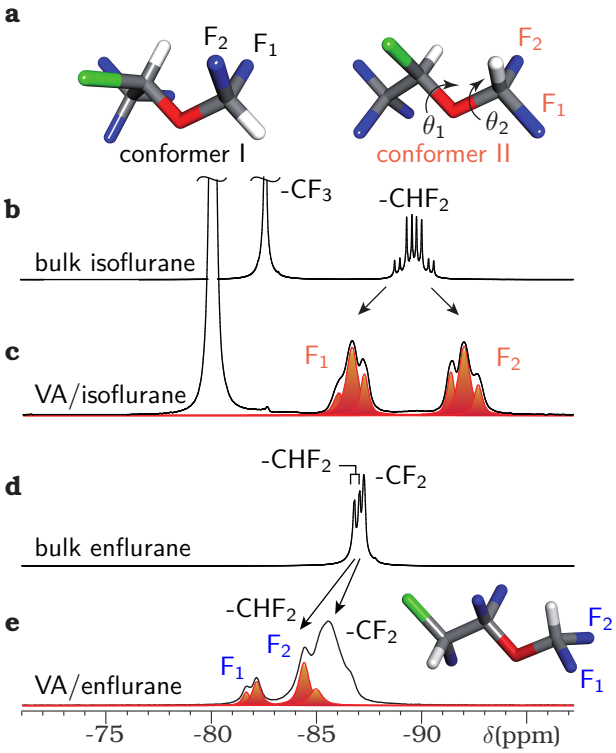

Figure 9.6: **a** The two conformational minima of isoflurane: conformer I and II with C-C-O-C of 139° and of 166°, respectively. ^{19}F MAS NMR spectra of **b** isoflurane on celite, **c** isoflurane in VA, **d** enflurane on celite, **e** enflurane in VA.

A theoretical study allowed us to establish the most stable conformers of isoflurane. We explored the dihedral angles θ_1 and θ_2 (C-C-O-C and F_1-C-O-C, respectively) and observed the stability of two conformational minima in the energy map with values as close as Δ = 0.5 kcal/mol. In conformer I, the F-C-O-C dihedral angles for F_1 and F_2 are 63° and 58° (i.e. both in *gauche* conformation); on the contrary in conformer II the F_1-C-O-C and F_2-C-O-C dihedral angles are 177° and 62°, respectively (i.e. F_1 in *trans* and F_2 in *gauche* conformations).[25,26] The experimental spectrum clearly indicates that the conformer II (with the torsional angle θ_2 setting F_1 in *trans* and F_2 in *gauche* conformation) provides the only feasible arrangement of isoflurane confined in the narrow dipeptide channels: in fact, the behavior of included isoflurane is common to all the observed dipeptide crystals, such as AI and VV. Indeed, the lateral steric encumbrance is reduced in conformer II because at least one of the two fluorine atoms is set in the more elongated *trans* arrangement, whereas in conformer I both fluorines protrude laterally in gauche arrangement. Conformer II also displayed a θ_1 torsional angle close to a *trans* arrangement, setting the main chain in the most elongated conformation. In the case of enflurane, a different behavior is observed for the CHF_2 group. Actually, the two fluorine nuclei resonate downfield with respect to those of the structural isomer isoflurane. This is due to the conformation of the two fluorine atoms, which are set at F-C-O-C dihedral angles of 105° and 135° and thus do not undergo γ-*gauche* effect when enflurane is included in the VA channels. The GCMC simulations of enflurane and isoflurane isotherms in VA show that the energetically stable conformers occupy the channels with a maximum loading corresponding to that of the experimental isotherms and the guests are not periodically distributed along the channels.

Bibliography

[1] Görbitz, C. H.; Gundersen, E. L-Valyl-L-alanine. *Acta Crystallographica Section C Crystal Structure Communications* **1996**, *52*, 1764–1767.

[2] Görbitz, C. Microporous organic materials from hydrophobic dipeptides. *Chemistry - A European Journal* **2007**, *13*, 1022–1031.

[3] Comotti, A.; Bracco, S.; Distefano, G.; Sozzani, P. Methane, carbon dioxide and hydrogen storage in nanoporous dipeptide-based materials. *Chemical Communications* **2009**, 284–286.

[4] Comotti, A.; Fraccarollo, A.; Bracco, S.; Beretta, M.; Distefano, G.; Cossi, M.; Marchese, L.; Riccardi, C.; Sozzani, P. Porous dipeptide crystals as selective CO_2 adsorbents: experimental isotherms *vs.* grand canonical Monte Carlo simulations and MAS NMR spectroscopy. *CrystEngComm* **2013**, *1*, 1503–1507.

[5] Soldatov, D. V.; Moudrakovski, I. L.; Grachev, E. V.; Ripmeester, J. A. Micropores in crystalline dipeptides as seen from the crystal structure, He pycnometry, and ^{129}Xe NMR spectroscopy. *Journal of the American Chemical Society* **2006**, *128*, 6737–6744.

[6] Afonso, R. V.; Durão, J.; Mendes, A.; Damas, A. M.; Gales, L. Dipeptide crystals as excellent permselective materials: sequential exclusion of argon, nitrogen, and oxygen. *Angewandte Chemie International Edition* **2010**, *49*, 3034–3036.

[7] Distefano, G.; Comotti, A.; Bracco, S.; Beretta, M.; Sozzani, P. Porous dipeptide crystals as polymerization nanoreactors. *Angewandte Chemie International Edition* **2012**, *51*, 9258–9262.

[8] Lim, S.; Kim, H.; Selvapalam, N.; Kim, K.-J.; Cho, S.; Seo, G.; Kim, K. Cucurbit[6]uril: organic molecular porous material with permanent porosity, exceptional stability, and acetylene sorption properties. *Angewandte Chemie International Edition* **2008**, *47*, 3352–3355.

[9] Qiu, F.; Chen, Y.; Tang, C.; Zhang, J.; Gong, M.; Su, B. Self-assembling surfactant-like peptide A_6K as potential delivery system for hydrophobic drugs. *International Journal of Nanomedicine* **2015**, 847.

[10] Chen, T.-H.; Kaveevivitchai, W.; Jacobson, A. J.; Miljanić, O. Š. Adsorption of fluorinated anesthetics within the pores of a molecular crystal. *Chemical Communications* **2015**, *51*, 14096–14098.

[11] Abrahams, B. F.; Dharma, A. D.; Donnelly, P. S.; Hudson, T. A.; Kepert, C. J.; Robson, R.; Southon, P. D.; White, K. F. Tunable porous coordination polymers for the capture, recovery and storage of inhalation anesthetics. *Chemistry A European Journal* **2017**, *23*, 7871–7875.

[12] Hendrickx, J. F. A.; Eger, E. I.; Sonner, J. M.; Shafer, S. L. Is synergy the rule? A review of anesthetic interactions producing hypnosis and immobility. *Anesthesia & Analgesia* **2008**, *107*, 494–506.

[13] Garcia, P.; Kolesky, S.; Jenkins, A. General anesthetic actions on $GABA_A$ receptors. *Current Neuropharmacology* **2010**, *8*, 2–9.

[14] Miller, P. S.; Aricescu, A. R. Crystal structure of a human $GABA_A$ receptor. *Nature* **2014**, *512*, 270–275.

[15] Ryan, S. M.; Nielsen, C. J. Global warming potential of inhaled anesthetics. *Anesthesia & Analgesia* **2010**, *111*, 92–98.

[16] Andersen, M. S.; Sander, S.; Nielsen, O.; Wagner, D.; Sanford, T.; Wallington, T. Inhalation anaesthetics and climate change. *British Journal of Anaesthesia* **2010**, *105*, 760–766.

[17] Yasny, J. S.; White, J. Environmental implications of anesthetic gases. *Anesthesia Progress* **2012**, *59*, 154–158.

[18] Görbitz, C. Microporous organic materials from hydrophobic dipeptides. *Chemistry – A European Journal* **2007**, *13*, 1022–1031.

[19] Gargiulo, N.; Peluso, A.; Aprea, P.; Hua, Y.; Filipović, D.; Caputo, D.; Eić, M. A chromium-based metal organic framework as a potential high performance adsorbent for anaesthetic vapours. *RSC Adv.* **2014**, *4*, 49478–49484.

[20] Brown, S. P. Probing proton-proton proximities in the solid state. *Progress in Nuclear Magnetic Resonance Spectroscopy* **2007**, *50*, 199–251.

[21] Bracco, S.; Comotti, A.; Valsesia, P.; Beretta, M.; Sozzani, P. Self-assembly of 1,4-cis-polybutadiene and an aromatic host to fabricate nanostructured crystals by CH$\cdots\pi$ interactions. *CrystEngComm* **2010**, *12*, 2318.

[22] Bracco, S.; Comotti, A.; Ferretti, L.; Sozzani, P. Supramolecular aggregation of block copolymers in the solid state as assisted by the selective formation of inclusion crystals. *Journal of the American Chemical Society* **2011**, *133*, 8982–8994.

[23] Williams, P. A.; Hughes, C. E.; Martin, J.; Courvoisier, E.; Buanz, A. B. M.; Gaisford, S.; Harris, K. D. M. Understanding the solid-state hydration behavior of a common amino acid: identification, structural characterization, and hydration/dehydration processes of new hydrate phases of L-lysine. *The Journal of Physical Chemistry C* **2016**, *120*, 9385–9392.

[24] Gorenstein, D. G. A generalized gauche NMR effect in carbon-13, fluorine-19, and phosphorus-31 chemical shifts and directly bonded coupling constants. Torsional angle and bond angle effects. *Journal of the American Chemical Society* **1977**, *99*, 2254–2258.

[25] Pfeiffer, A.; Mack, H.-G.; Oberhammer, H. Enflurane: structure and conformational properties. *Journal of the American Chemical Society* **1998**, *120*, 6384–6388.

[26] Lesarri, A.; Vega-Toribio, A.; Suenram, R. D.; Brugh, D. J.; Nori-Shargh, D.; Boggs, J. E.; Grabow, J.-U. Structural evidence of anomeric effects in the anesthetic isoflurane. *Physical Chemistry Chemical Physics* **2011**, *13*, 6610.

10. Conclusions

Dynamics in porous materials is an incredibly complex topic, full of challenges and promising effects. During my thesis I was able to unveil some details of this world, understanding the feature regulating this motion.

The results are not only related to dynamics but to the study of novel porous materials and their properties, such as gas adsorption, gas-host energy interaction and pore shape.

10.1 Interaction

I have shown how a gas can influence the molecular rotor. Interaction between CO_2 and *p*-phenyl rotor increases the activation energy of the motion without altering the others parameters (rotation mechanism and frequency at infinite temperature). The most important result is that the modulation of rotor dynamics is function of loading, a feature that is rarely observed. The statement remains true even in a complex porous system with no uniform loading.

10.2 Gas Dynamics

A new method was developed to study diffusion of gases inside porous crystals, combining NMR and *ab initio* calculations. This method allows to obtain a complete picture of the motion, especially in the complex single file diffusion regime. Xenon is confirmed to be a very sensitive probe for channel size even if it has been used in an unconventional way. CO_2 reveals how strongly it can be affected by electrostatic interactions, which are even able to imprint a screw diffusion mechanism to the gas molecules.

10.3 Drug Vessels

We demonstrated that dipeptide crystals offer a suitable room for hosting anesthetic molecules and tuning their volatility. The diversity in pore size and shape allows the selection of the most appropriated crystal for specific guests. The biodegradability and biocompatibility of these materials could encourage their use in biomedical applications.

10.4 Fluorine PAFs

The functionalization, even if it involves the addition of a small fluorine atom, changes the material properties. This not only increases the interaction with CO_2 but the pores become significantly narrower.

10.5 Future

The results individually may seems disconnected but they are all fundamental for the next phase. We want to synthesize a crystalline porous material with partially fluorinated rotors and very low activation energy. The dipole generated by fluorination can theoretically be influenced by an external electric field. If loading affects rotor speed, why should the rotor speed not affect the loading? The basic idea is to generate a rotor that responds to external stimuli and therefore to the amount of adsorbed gas. This material should store and release gas on command. Since this would happen without a structural transition a considerable amount of cycles is expected.

10.6 Scientific Impact of Mattia Negroni

Articles

1. Comotti, A.; Castiglioni, F.; Bracco, S.; Perego, J.; Pedrini, A.; Negroni, M.; Sozzani, P. Fluorinated porous organic frameworks for improved CO_2 and CH_4 capture. *Chemical Communication* **2019**, *55*, 8999-9002.

2. Xing, G.; Bassanetti, I.; Bracco, S.; Negroni, M.; Bezuidenhout, C.; Ben, T.; Sozzani, P.; Comotti, A. A double helix of opposite charges to form channels with unique CO_2 selectivity and dynamics. *Chemical Science* **2019**, *10*, 730-736.

3. Bassanetti, I.; Bracco, S.; Comotti, A.; Negroni, M.; Bezuidenhout, C.; Canossa, S.; Mazzeo, P. P.; Marchió, L.; Sozzani, P. Flexible porous molecular materials responsive to CO_2, CH_4 and Xe stimuli. *Journal of Materials Chemistry A* **2018**, *6*, 14231-14239.

4. Bracco, S.; Asnaghi, D.; Negroni, M.; Sozzani, P.; Comotti, A. Porous dipeptide crystals as volatile-drug vessels. *Chemical Communication* **2017**, *54*, 148-151.

5. Bracco, S.; Miyano, T.; Negroni, M.; Bassanetti, I.; Marchio', L.; Sozzani, P.; Tohnai, N.; Comotti, A. CO_2 regulates molecular rotor dynamics in porous materials. *Chemical Communications* **2017**, *53*, 7776-7779.

6. Bracco, S.; Castiglioni, F.; Comotti, A.; Galli, S.; Negroni, M.; Maspero, A.; Sozzani, P. Ultrafast molecular rotors and their CO_2 tuning in MOFs with rod-like ligands. *Chemistry - A European Journal* **2017**, *23*, 11210-11215.

Conferences

1. A. Comotti, S. Bracco, J. Perego, M. Negroni, C. Bezuidenhout, I. Supino, A. Pedrini, P. Sozzani; *Imprinting the pore symmetry to CO_2 and Xe, gas dynamics and ultra-fast molecular rotors in molecular porous materials with tetrahedral building blocks*; POPs 2019, 2nd international symposium on porous organic polymers (Heidelberg, Germany, 8-12 September 2019).

2. A. Comotti, S. Bracco, J. Perego, M. Negroni, C. Bezuidenhout, P. Sozzani; *Dynamics of CO_2 and Xe and Ultra-fast Molecular Rotors in Porous Crystals*; ISMSC 2019, 14th International Symposium on Macrocyclic and Supramolecular Chemistry, (Lecce, Italy, 2-6 June 2019).

3. A. Pedrini, S. Bracco, F. Castiglioni, A. Comotti, S. Galli, A. Maspero, M. Negroni, P. Sozzani; *Fluorinated bis(pyrazole)-based MOFs for gas adsorption and separation*; ICS 2019, Innovative Catalysis and Sustainability, International Winter School (Bardonecchia, Italy, 7-11 January 2019).

4. Sozzani, P., Bracco, S., Comotti, A., Bassanetti, I., Castiglioni, F., Negroni, M., A. Pedrini, J. Perego; *Switchable Dynamics and Flexibility in Gas-absorptive Porous Materials*; Materials.it 2018 - Italian National Conference on Materials Science and Technology (Bologna, Italy, 22-26 October, 2018).

5. A. Comotti, S. Bracco, F. Castiglioni, M. Negroni, F. Alite, P. Sozzani; *Ultra-fast Molecular Rotors in Porous Supramolecular Architectures and Dynamics Control by Chemical Stimuli*; 7th EuCheMS Chemistry Congress (Liverpool, UK, 26-30 August 2018).

6. S. Bracco, A. Comotti, M. Negroni, F. Castiglioni, A. Pedrini, P. Sozzani; *Ultra-fast Molecular Rotor Dynamics and their Regulation in Nanoporous Architectures*; Euromar 2018, (Nantes, France 1-5 July 2018).

7. M. Negroni, S. Bracco, A. Comotti, C. Bezuidenhout, I. Bassanetti, L. Marchio and P. Sozzani; *Reorientation*

jumps and energy profile for Xe diffusing from site to site along the channels of porous molecular crystals; Xemat 2018 - International Xenon Symposium (Philadelphia, USA, 5-8 May 2018).

8. S. Bracco, A. Comotti, F. Castiglioni, M. Negroni, P. Sozzani; *Molecular Rotor Dynamics in Nanoporous Architectures*; ISNSC-9, 9th International Symposium on Nano & Supramolecular Chemistry, (Naples, Italy, 4-7 September 2017).

9. S. Bracco, M. Negroni, F. Castiglioni, J. Perego, D. Piga, A. Comotti, P. Sozzani; *Metal-organic and organic frameworks: porosity, gas adsorption and fast dynamics*; Italian Crystal Growth 2017 - Materials and Methods in Crystal growth Conference (Milan, Italy, 20-21 November 2017).

10. A. Comotti, S. Bracco, F. Castiglioni, M. Negroni, P. Sozzani; *Molecular Rotors in Porous Supramolecular Architectures*; ICCOSS XXIII, 23rd International Conference on the Chemistry of the Organic Solid State (Stellenbosch, South Africa, 2-7 April 2017).

A. Materials Details

BSPEB and *n*-benzylamine

Molecular Ionic Crystal

Cell: Monoclinic
Group: $P2_1/c$
Formula: $C_{20}H_{20}NO_4S$
Z: 4

a: 5.51851 Å
b: 40.4605 Å
c: 8.28955 Å
α: 90°
β: 96°
γ: 90°

Volume: 1840.9 Å^3
Void: 15.2 %
Density (bulk): 1.18 g/cm^3
Density (true): 1.39 g/cm^3
Surface (Langmuir): 332 m^2/g
Surface (BET): 291 m^2/g

Activation

The material usually present the inclusion of 1,4-dioxane. The activation is performed at 80° C in vacuum overnight.

Zn-BPEB

Metal-Organic Framework

Cell: Orthorhombic
Group: Cccm
Formula: $C_{16}H_8N_4Zn$
Z: 8

a: 25.3033 Å
b: 26.4643 Å
c: 7.30733 Å
α: 90°
β: 90°
γ: 90°

Volume: 4893.2 Å^3
Void: 48.2 %
Density (bulk): 0.88 g/cm^3
Density (true): 1.54 g/cm^3
Surface (Langmuir): 1366 m^2/g
Surface (BET): 1214 m^2/g

Activation

The material presents traces of MeOH. The activation is performed at 120° C in vacuum overnight.

TCF-1

Molecular Crystal

Cell: Tetragonal
Group: $P4_2/n$
Formula: $C_{29}H_{20}O_8$
Z: 2

a: 12.76 Å
b: 12.76 Å
c: 8.173 Å
α: 90°
β: 90°
γ: 90°

Volume: 1330.7 Å^3
Void: 18.5 %
Density (bulk): 1.23 g/cm^3
Density (true): 1.51 g/cm^3
Stability: 700 K (340 K closed-packed transition)

Activation

The material presents traces of THF. The activation is performed at 60° C (or room temperature) in vacuum overnight.

CPOS-5

Molecular Ionic Crystal

Cell: Tetragonal
Group: $I41/A$
Formula: $C_{41}H_{40}N_8O_{12}S_4$
Z: 4

a: 25.7276 Å
b: 25.7276 Å
c: 7.7202 Å
α: 90°
β: 90°
γ: 90°

Volume: 5110.1 Å^3
Void: 17.4 %
Density (bulk): 1.25 g/cm^3
Density (true): 1.51 g/cm^3
Stability: 723 K

Activation

The material has water as inclusion compound. The activation is performed at 150° C in vacuum overnight.

L-VALYL-L-ALANINE

Dipeptide Crystal

Cell: Hexagonal
Group: P 6_1
Formula: $C_8H_{16}N_2O_3$
Z: 6

a: 14.4240 Å
b: 14.4240 Å
c: 9.9960 Å
α: 90°
β: 90°
γ: 180°

Volume: 1801.1 Å^3
Void: 17.1 %
Density (bulk): 1.04 g/cm^3
Density (true): 1.25 g/cm^3

L-VALYL-L-VALINE

Dipeptide Crystal

Cell: Hexagonal
Group: P 6_1
Formula: $C_{10}H_{20}N_2O_3$
Z: 6

a: 14.5730 Å
b: 14.5730 Å
c: 10.3540 Å
α: 90°
β: 90°
γ: 180°

Volume: 1904.3 Å^3
Void: 12.5 %
Density (bulk): 1.13 g/cm^3
Density (true): 1.29 g/cm^3

L-ALANYL-L-ISOLEUCINE

Dipeptide Crystal

Cell: Hexagonal
Group: P 6_1
Formula: $C_9H_{18}N_2O_3$
Z: 6

a: 14.2610 Å
b: 14.2610 Å
c: 10.2210 Å
α: 90°
β: 90°
γ: 180°

Volume: 1800.2 Å^3
Void: 13.3 %
Density (bulk): 1.12 g/cm^3
Density (true): 1.29 g/cm^3

L-ISOLEUCYL-L-ALANINE

Dipeptide Crystal

Cell: Hexagonal
Group: P 6_1
Formula: $C_9H_{18}N_2O_3$
Z: 6

a: 14.3720 Å
b: 14.3720 Å
c: 9.8282 Å
α: 90°
β: 90°
γ: 180°

Volume: 1758.1 Å^3
Void: 11.1 %
Density (bulk): 1.15 g/cm^3
Density (true): 1.29 g/cm^3

L-ISOLEUCYL-L-VALINE

Dipeptide Crystal

Cell: Hexagonal
Group: P 6_1
Formula: $C_{11}H_{22}N_2O_3$
Z: 6

a: 14.8710 Å
b: 14.8710 Å
c: 10.3050 Å
α**:** 90°
β**:** 90°
γ**:** 180°

Volume: 1973.6 $Å^3$
Void: 10.0 %
Density (bulk): 1.16 g/cm^3
Density (true): 1.29 g/cm^3